Lucas F. M. da Silva
Robert D. Adams   *Editors*

7th International Conference on Structural Adhesive Bonding 2023

Selected Contributions of AB 2023

Springer

Proceedings in Engineering Mechanics

Research, Technology and Education

Series Editors

Lucas F. M. da Silva, Faculty of Engineering, University of Porto, Porto, Portugal

António J. M. Ferreira ⓘ, Faculty of Engineering, University of Porto, Porto, Portugal

This book series publishes the results of meetings dealing with material properties in engineering and science. It covers a wide range of topics, from the fundamentals of materials mechanics and applications for various industries to aspects of scientific training and career development. The volumes in the series are based typically on primary research materials presented at conferences, workshops, and similar scientific meetings, and represent comprehensive scientific and technical studies.

Lucas F. M. da Silva · Robert D. Adams
Editors

7th International Conference on Structural Adhesive Bonding 2023

Selected Contributions of AB 2023

Springer

Editors
Lucas F. M. da Silva
Department of Mechanical Engineering
Faculty of Engineering
University of Porto
Porto, Portugal

Robert D. Adams
Department of Mechanical Engineering
University of Bristol
Bristol, UK

Preface

This volume of the series *Proceedings in Engineering Mechanics—Research, Technology and Education* contains selected papers presented at the 7th International Conference on Structural Adhesive Bonding (AB 2023), held in Porto (Portugal) during 13–14 July 2023 (www.fe.up.pt/ab2023). The goal of the conference was to provide a unique opportunity to exchange information, present the latest results as well as to discuss issues relevant to structural adhesive bonding research today. Approximately 200 papers were presented by researchers from more than 27 countries.

In order to disseminate the work presented in AB 2023, selected papers were prepared which resulted in the present volume dedicated to adhesive bonding. A wide range of topics are covered resulting in nine papers dealing with the most recent research topics concerning adhesive bonding: *Adhesive Formulation and Properties* (first two chapters), *Adhesion and Surface Treatments* (three chapters), *Joint Design* (two chapters) and *Durability of Structural Adhesive Joints* (last two chapters). The book represents the latest trends in adhesive joining and serves as a reference volume for researchers and graduate students working with adhesive bonding.

The organizer and editor wish to thank all the authors for their participation and cooperation, which made this volume possible. Finally, I would like to thank the team of Springer-Verlag, especially Dr. Christoph Baumann and Ute Heuser, for the excellent cooperation during the preparation of this volume.

Porto, Portugal   Prof. Lucas F. M. da Silva
                                                                              lucas@fe.up.pt

Bristol, UK   Prof. Robert D. Adams
September 2023

Contents

Durability of Structural Adhesive Joints

Adhesive Formulation and Properties

Analysis of the Influence of Basalt Powders on the Mechanical Properties of Epoxy Coatings

Agnieszka Chowaniec-Michalak

Abstract Epoxy resins are a popular material for floor coatings, especially industrial floors. Due to the harmfulness of epoxy resin, efforts are made to reduce the amount of epoxy resin needed to make the coating. Fillers and additives, especially mineral ones, are used for this purpose. The paper investigated the possibility of using three basalt powders as an additive to epoxy coatings. The weight content of basalt powders in the coating ranged from 0 to 29%. Two tests of the mechanical properties of the epoxy coating were performed. The hardness was tested with a Shore D durometer, and the pull-off strength was tested by the method of pull-off using an automatic device. It has been shown that basalt powders improve the hardness of the epoxy coating (by 8%) and do not deteriorate the pull-ff strength of the epoxy coating.

Keywords Industrial floors · Epoxy resin · Hardness · Pull-off strength

1 Introduction

Among the materials with a wide industrial application, epoxy resins can be distinguished. Thanks to their very good adhesion, strength parameters, chemical resistance and corrosion resistance, they have found a wide range of applications, e.g. in civil engineering, aerospace industry, electrical systems and electronics, composite materials, as adhesives, paints, coatings and reinforcing materials (Waseem et al. 2021). Considering the natural environment, one cannot ignore the fact that the chemical composition of epoxy resin contains many very harmful substances that are toxic to organisms. Working with epoxy resins can lead to breathing difficulties and allergies. Another problem is the management of epoxy resin waste. Attempts are being made to recycle resin materials (Thamizh Selvan et al. 2021), but this is problematic, because cured epoxy resins can only be removed mechanically.

A. Chowaniec-Michalak (✉)

Department of Materials Engineering and Construction Processes, Wroclaw University of Science and Technology, Wroclaw, Poland

e-mail: agnieszka.chowaniec@pwr.edu.pl

Therefore, many attempts to modify and fill epoxy resin with various materials can be found in the literature. Often, these additives to epoxy resins not only perform the function of a filler, but also improve its some properties. In Burda et al. (2021), calcium carbonate and nanosilica were used as an additive to the epoxy resin, which improved the compressive strength by 20%. In turn, in Naghizadeh et al. (2018), the addition of nanosilica and multi-walled carbon nanotubes improved impact resistance. In Ojha et al. (2022), silica and carbon had a positive effect on tensile, flexural, compression and erosion wear. Krzywiński et al. (2023) showed that the addition of waste quartz-feldspar powder improves the adhesion of the epoxy coating to the substrate and its thermal properties. Multi-walled carbon nanotubes can also improve adhesive fracture resistance of the epoxy coating (Khoramishad and Khakzad, 2018). Epoxy resins with the addition of granite powder work very well as floor repair systems, in which, thanks to the addition of granite powder, better pull-ff strength and resistance to thermal shock were obtained (Kampa et al. 2023). Kırbaş (2023) showed that the addition of pumice in an amount of up to 10% reduces the thermal conductivity coefficient, increases the hardness and improves the mechanical properties of the epoxy resin. Other additives to epoxy resins that improved some of their properties include graphite (Rzeczkowski et al. 2020), aluminum oxide (Kumar et al. 2021), lignin (Fernando et al. 2023), flax (Hadj-Djilani et al. 2023).

Among the additives for epoxy coatings that can be successfully used in epoxy floor coatings and have been previously studied by the authors, there are mineral powders, especially such as: quartz (Chowaniec et al. 2022), granite (Chowaniec 2021) and limestone powders (Chowaniec-Michalak et al. 2022). The next mineral powders, the usefulness of which for epoxy coatings would be worth investigating, are basalt powders. Basalt is successfully used in other materials in civil engineering, such as concrete (Karasin et al. 2022).

In conclusion, the aim of the research is to test the suitability of basalt powders as an additive to the epoxy coating used in floors.

The specific objectives of the research are to determine the effect of basalt powders on such mechanical properties of the epoxy coating that are important for floor coatings. For the durability of the coating, the pull-off strength and hardness of the epoxy coating are of particular importance.

2 Materials and Methods

2.1 Materials for Tests

Epoxy resin intended for coatings of industrial floors was used in the tests. The selected epoxy resin was a two-component product, where the first component contained a mixture of epoxy resins based on bisphenol A and F, and the second component was a phenalkamine curing agent, which should be mixed together in the appropriate weight proportions (component 1: component 2 = 100: 50).

Table 1 The weight ratio of the mixture of epoxy resin with basalt powder

Series	A weight ratio of 1:2:B			Percentage of basalt powder %
	Component 1	Component 2	Basalt powder (B)	
R (reference)	100	50	0	0
B1-I, B2-I, B3-I	100	50	12	7
B1-II, B2-II, B3-II	100	50	24	14
B1-III, B2-III, B3-III	100	50	36	19
B1-IV, B2-IV, B3-IV	100	50	48	24
B1-V, B2-V, B3-V	100	50	60	29

Basalt powder was chosen as the filler. In order to determine what particle size of the basalt powder is optimal as a filler for the epoxy coating, the basalt powder was sieved through a set of 3 sieves. As a result, three types of basalt powders with the following particle sizes were obtained:

- basalt powder B1 with a particle size of up to 0.100 mm,
- basalt powder B2 with a particle size of 0.100–0.125 mm,
- basalt powder B3 with a particle size of 0.125–0.250 mm.

The basalt powders were mixed with the epoxy resin according to the weight ratio given in Table 1, with the weight ratio between components 1 and 2 of the epoxy resin not changed (always 100:50).

2.2 Samples Preparation

The epoxy coating was made on a concrete substrate made of concrete class C30/37 and 15 cm thick. The surface of the substrate was mechanically grinded, vacuumed and then impregnated with an epoxy bonding agent. The bonding agent was applied with a sponge roller. After 24 h, an epoxy coating with basalt powders was applied to the separated areas (Fig. 1) with a notched trowel. Figure 2 shows the view of the concrete substrate after vacuuming, applying the bonding agent and applying the epoxy coating. The thickness of the bonding agent layer was about 0.1–0.2 mm, and the thickness of the epoxy coating was 1.4 mm. The entire procedure was performed as for a typical epoxy floor.

2.3 Shore D Hardness Tests

Hardness tests were performed with a Shore D durometer in accordance with the ISO 868:2003 standard. The test consisted in pressing an indenter into the epoxy
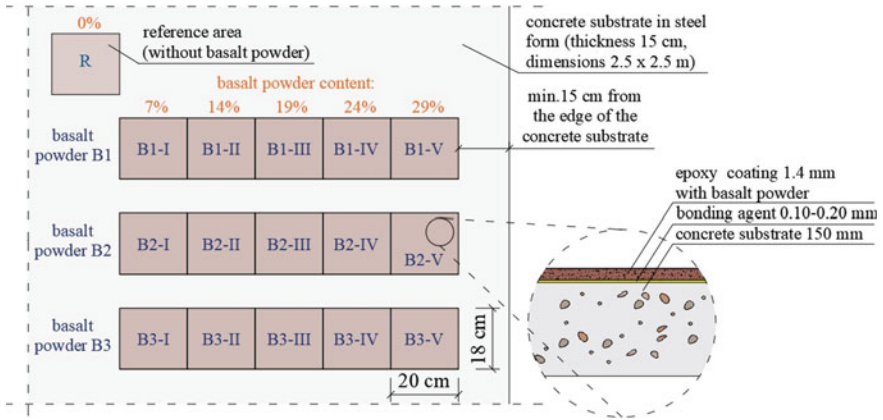
Fig. 1 Division of the concrete substrate into areas where a multi-variant epoxy coating with basalt powders was applied
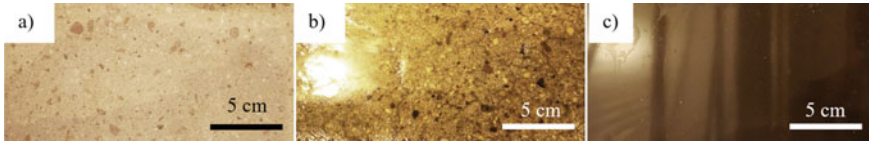
Fig. 2 The view of the concrete substrate after: **a** vacuuming, **b** applying the bonding agent, **c** applying the epoxy coating

coating and reading the indications of the device (Fig. 3). Measurements were taken at 5 points for each coating.

2.4 Pull-Off Strength Tests

Pull-off strength tests of the epoxy coating were performed in accordance with the procedure described in ASTM D4541. In each rectangular area (see Fig. 1) three test points were designated. Circles with a diameter of 50 mm and a depth of approximately 4 mm were cut around the points to cut through the entire epoxy coating down to the concrete substrate. Then, the surfaces of the epoxy coating were cleaned, degreased with acetone and steel discs with a diameter of 50 mm were glued with epoxy glue. After 7 days, the discs were peeled off using an automatic measuring machine Y-216 machine (Proceq, Switzerland). As shown in Fig. 4, a steel pin was first screwed into the disc and placed in the holder of the measuring machine. Then the machine pulled out the disk with a constant force increase rate of 0.050 MPa/s. The pull-off strength was calculated as the quotient of the maximum applied load (F) and the base area of the steel disc.
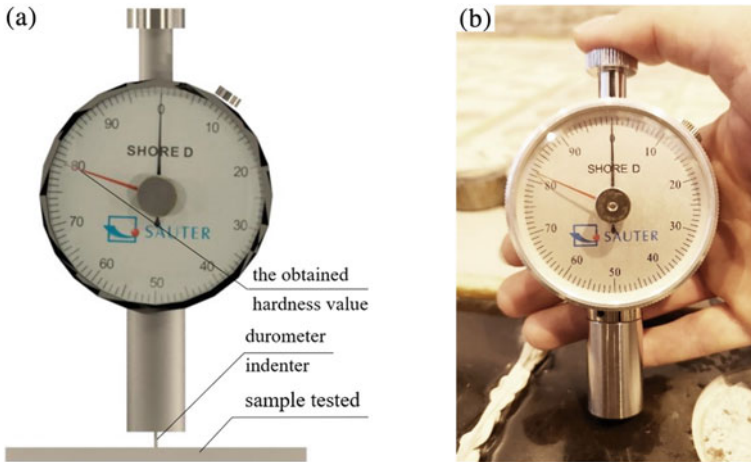
Fig. 3 **a** Scheme of the hardness test stand, **b** shore durometer during testing
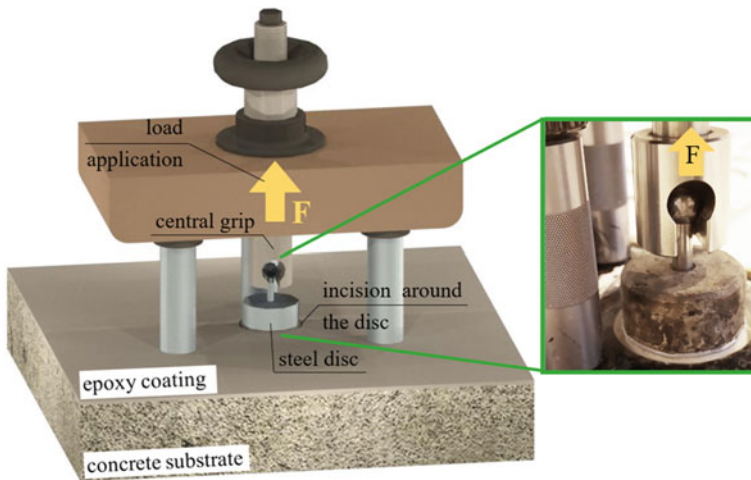
Fig. 4 View of the pull-off test stand

3 Results and Discussion

3.1 Shore D Hardness

Table 2 presents the results of hardness tests of the epoxy coating with three types of basalt powders. For the reference sample (R) without the addition of powders, an average hardness of 79 ± 0.8 was obtained. For the epoxy coating with basalt powders, in all cases, the hardness of the coating increased with the increase in the

powder content. For the epoxy coating with powder B1 (particle size <0.100 mm) the hardness increased from 81 to 83, for powder B2 (particle size from 0.100 to 0.125 mm) and B3 (particle size from 0.125 to 0.250 mm) the hardness increased from 80 to 82. The improvement in hardness caused by the addition of basalt powder is due to the very good hardness of the basalt stone (usually a minimum of 6 on the Mohs scale). The hardness improvement of the epoxy coating with basalt powders relative to the reference sample (last column in Table 2) ranges from 1.0 to 4.8%. The improvement is not much because the unmodified epoxy already has a very good hardness (79 out of 100 Shore D).

The average hardness values together with the standard deviation are presented in Fig. 5, where it can be seen that the best values were obtained for the B1 powder, i.e. for the powder with the smallest particles. The smallest values of standard deviations (SD) and coefficients of variation (CV) were also obtained for powder B1 (SD from 0.4 to 0.7, CV from 0.5 to 0.9). This may be due to the fact that the smaller particles of the basalt powder are sedimented less in the epoxy resin, and therefore there are more of them in the upper part of the coating. A similar relationship was noticed in previous studies of epoxy resin with lime powder (Chowaniec-Michalak et al. 2022), where

Table 2 Results of the hardness test for epoxy coating with basalt powders

Series	Single results, −					Average hardness, −	Standard deviation, −	Coefficient of variation, %	Change relative to sample R, %
Reference—no powder									
R	79	78	80	79	80	79	0.8	1.1	–
B1 basalt powder									
B1-I	81	81	81	80	81	81	0.4	0.6	2.0
B1-II	82	82	82	81	82	82	0.4	0.5	3.3
B1-III	82	82	83	82	82	82	0.4	0.5	3.8
B1-IV	83	82	83	83	83	83	0.4	0.5	4.5
B1-V	82	83	84	83	83	83	0.7	0.9	4.8
B2 basalt powder									
B2-I	80	80	80	81	81	80	0.5	0.7	1.5
B2-II	81	82	82	80	82	81	0.9	1.1	2.8
B2-III	81	81	82	82	82	82	0.5	0.7	3.0
B2-IV	83	82	82	82	80	82	1.1	1.3	3.3
B2-V	83	81	81	82	83	82	1.0	1.2	3.5
B3 basalt powder									
B3-I	79	80	80	81	80	80	0.7	0.9	1.0
B3-II	82	81	82	82	81	82	0.5	0.7	3.0
B3-III	81	82	81	80	82	81	0.8	1.0	2.5
B3-IV	81	83	81	82	81	82	0.9	1.1	3.0
B3-V	83	81	83	81	82	82	1.0	1.2	3.5
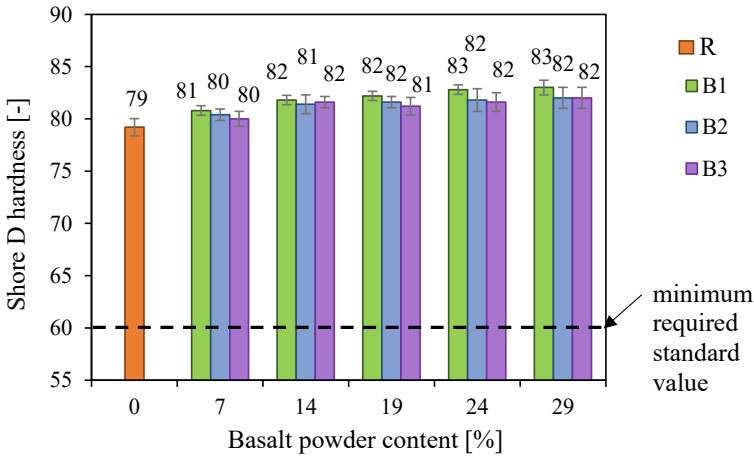
Fig. 5 Graph of the relationship between the hardness of the epoxy coating and the percentage of basalt powder in the epoxy coating

scanning electron microscope images showed that the larger the powder particles, the more they sedimented in the epoxy coating. These assumptions result from Stokes' law, from which, among others, it follows that larger particles sink faster in the liquid than smaller ones.

Figure 5 also shows the minimum hardness value required by the PN-EN 1504-2 standard. For floor coatings the minimum value is 60, so all the values obtained are well above. Epoxy coatings are usually used in industrial halls where they are exposed to intensive use and it is desirable that the coating has the highest possible hardness.

3.2 Pull-Off Strength

Figure 6 shows all places where pull-off strength tests and detached steel discs were performed. In almost all places, the epoxy coating peeled off along with a thick layer of the substrate with aggregate—cohesive failure occurred there. Only in one place (green arrow) the coating partially broke off without the concrete substrate. Partial adhesive failure occurred at this location.

Table 3 shows the average pull-off strength values of the epoxy coating with basalt powders. Neither an upward nor a downward trend was observed due to the increase in the content of basalt powders in the epoxy coating. For 7 samples, the average values were lower than for the reference sample, for 7 samples higher, and for one sample (B2-V) it was almost the same as for the reference coating. The change from sample R ranged from −20.3% to +7.9%.
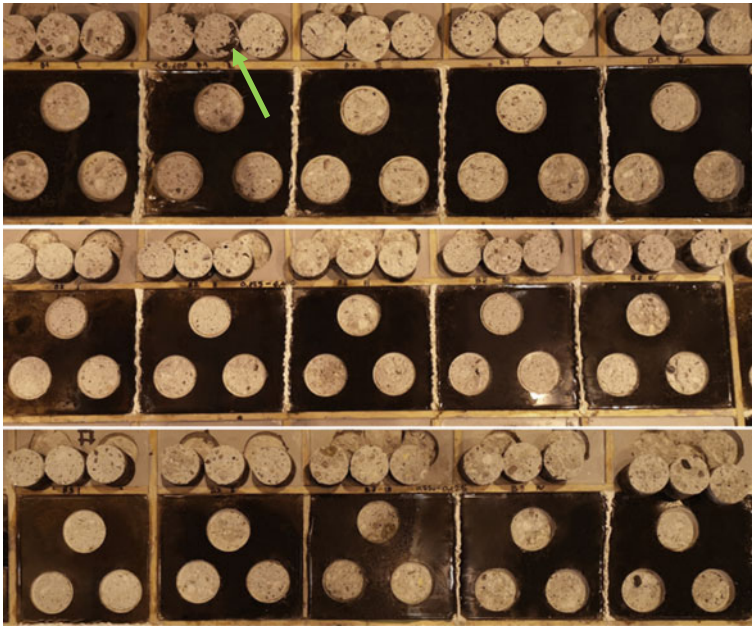
Fig. 6 View of all measurement points after the pull-off strength test

In Fig. 7, the results are presented in the form of a graph. Most of the results are within the standard deviation of sample R (orange horizontal band), except for 2 samples (one from B2 powder and one from B3) which are below the band.

It should be noted that since the failure occurred in the concrete substrate, the strength of the concrete substrate may have a greater impact on the results than the adhesion of the epoxy coating. In these tests, in almost all places (except one), the failure occurred at some depth in the concrete substrate. This means that the epoxy coating with basalt powder has very good adhesion to the concrete substrate (no complete adhesive failure) and that the adhesion between the epoxy coating and the concrete substrate is greater than the strength of the concrete. C30/37 class concrete was used to make the concrete substrate, i.e. higher-strength concrete usually used as industrial floors.

Figure 7 also shows the minimum value of pull-off strength required by the standard for the floor coating, which is 1.5 MPa. Thus, the resulting reduction in the pull-off strength value is not a barrier to the use of basalt powder as a filler for the epoxy coating. Therefore, from the point of view of pull-off strength, basalt powder can be successfully used as a filler for epoxy coating. All three types of basalt powders achieved satisfactory results (above the standard minimum value, failure occurred in concrete).

Table 3 Results of the pull-off strength test for epoxy coating with basalt powders

Series	Single results, MPa			Average pull-off strength, MPa	Standard deviation, MPa	Coefficient of variation, %	Change relative to sample R, %
Reference—no powder							
R	2.55	3.21	2.98	2.91	0.34	11.5	–
B1 basalt powder							
B1-I	3.60	2.29	2.63	2.84	0.68	23.9	−2.5
B1-II	3.21	2.34	2.49	2.68	0.47	17.4	−8.0
B1-III	2.88	2.97	2.70	2.85	0.14	4.8	−2.2
B1-IV	2.85	2.80	2.41	2.69	0.24	9.0	−7.8
B1-V	3.41	3.15	2.52	3.03	0.46	15.1	3.9
B2 basalt powder							
B2-I	2.16	2.51	2.91	2.53	0.38	15	−13.3
B2-II	3.61	2.37	3.45	3.14	0.67	21	7.9
B2-III	3.22	3.22	2.67	3.04	0.32	10	4.2
B2-IV	3.31	2.96	2.76	3.01	0.28	9	3.3
B2-V	2.97	2.56	3.23	2.92	0.34	12	0.2
B3 basalt powder							
B3-I	2.42	3.35	3.37	3.05	0.54	18	4.6
B3-II	3.53	2.29	3.15	2.99	0.64	21	2.6
B3-III	2.04	2.82	2.11	2.32	0.43	19	−20.3
B3-IV	3.05	3.09	2.02	2.72	0.61	22	−6.6
B3-V	3.05	3.28	2.83	3.05	0.23	7	4.8

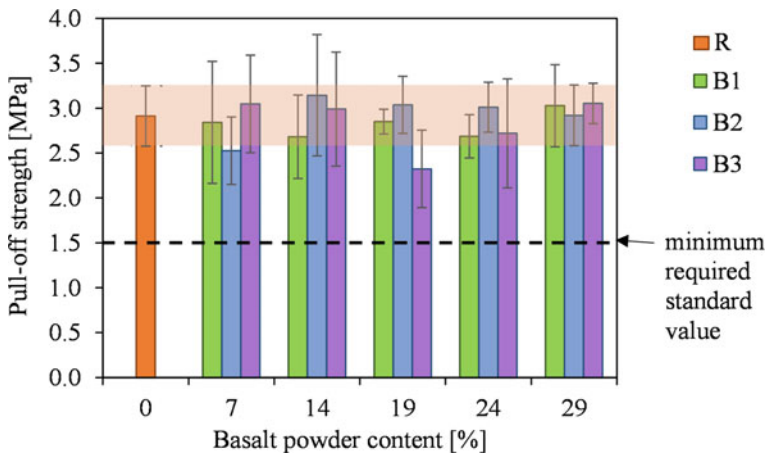**Fig. 7** Graph of the relationship between the pull-off strength of the epoxy coating and the percentage of basalt powder in the epoxy coating

4   Conclusions

The article presents the results of research into the influence of three types of basalt powders on selected mechanical properties of the epoxy floor coating, including hardness and pull-off strength. The basalt powders differed in particle size, and their mass percentage in the coating ranged from 7 to 29%. Based on the research, the following conclusions were drawn:

- The addition of basalt powders has a positive effect on the hardness of the epoxy coating. With the increase in the content of basalt powders, the hardness of the coating increases. The greatest improvement in hardness was 4.8% for 29% of the B1 powder content, i.e. the powder with the smallest particles.
- The basalt powder does not unequivocally worsen or improve the pull-off strength of the epoxy coating. Half of the samples had higher values and half of the samples had lower values than the reference coating. The smallest average value obtained (2.32 MPa) is still above the standard required value (1.50 MPa).
- Among the tested basalt powders, slightly better results were obtained for the B1 powder with particle sizes <0.100 mm.

Basalt powders can potentially be used as a filler for epoxy coatings. In future research, further properties relevant to epoxy floor coatings, such as compressive strength, flexural strength and abrasion resistance, should be analyzed.

References

ASTM D4541-17: Standard Test Method for Pull-Off Strength of Coatings Using Portable Adhesion Testers. ASTM International, West Conshohocken, PA (2017)

Burda, I., Barbezat, M., Brunner, A.J.: The effect of nano- and micron-scale filler modified epoxy matrix on glass-fiber reinforced polymer insulator component behavior. Proc. Inst. Mech. Eng. Part L: J. Mater. Design Appl. **235**(6), 1287–1301 (2021). https://doi.org/10.1177/146442072 11000775

Chowaniec, A.: The effect of the viscosity and the contact angle on the pull-off strength of epoxy resin modified with waste granite powders. In: da Silva, L.F.M., Adams, R.D. (eds.) 6th International Conference on Adhesive Bonding 2021. Proceedings in Engineering Mechanics. Springer, Cham (2021). https://doi.org/10.1007/978-3-030-87668-5_6

Chowaniec, A., Czarnecki, S., Sadowski, Ł.: The effect of the amount and particle size of the waste quartz powder on the adhesive properties of epoxy resin coatings. Int. J. Adhes. Adhes. **117** (2022). https://doi.org/10.1016/j.ijadhadh.2021.103009

Chowaniec-Michalak, A., Czarnecki, S., Sadowski, Ł., Królicka, A.: Recycling of waste limestone powders for the cleaner production of epoxy coatings: fundamental understanding of the mechanical and microstructural properties. J. Cleaner Prod. **372** (2022). https://doi.org/10.1016/j.jclepro.2022.133828

Fernando, P.H.L., Antonino, L.D., Garcia, G.E.S., de Sousa Júnior, R.R., Neto, A.V., Nakamoto, F.Y., dos Santos, D.J.: Effects of the incorporation of modified kraft lignin on the mechanical properties of epoxy adhesive: experimental and theoretical approaches. J. Adhes. (2023). https://doi.org/10.1080/00218464.2023.2194535

Hadj-Djilani, A., Kioua, A., Zitoune, R., Toubal, L., Bougherara, H.: Exploring the flexural and impact properties of pure flax/epoxy and Kevlar/flax/epoxy composites through experimental and numerical analysis. Proc. Inst. Mech. Eng. Part L: J. Mater. Des. Appl. (2023). https://doi.org/10.1177/14644207231178663

Kampa, Ł., Oluwasegun, E., Sadowski, Ł.: An innovative way to repair damaged concrete floors using epoxy adhesives: a case study of its technical assessment and renovation. Pract. Periodical Struct. Des. Constr. 28(2) (2023). https://doi.org/10.1061/PPSCFX.SCENG-1213

Karasin, A., Hadzima-Nyarko, M., Işık, E., Doğruyol, M., Karasin, I.B., Czarnecki, S.: The effect of basalt aggregates and mineral admixtures on the mechanical properties of concrete exposed to sulphate attacks. Materials 15, 1581 (2022). https://doi.org/10.3390/ma15041581

Khoramishad, H., Khakzad, M.: Toughening epoxy adhesives with multi-walled carbon nanotubes. J. Adhes. 94(1), 15–29 (2018). https://doi.org/10.1080/00218464.2016.1224184

Kırbaş, I.: Effects of pumice additions on thermal and mechanical behaviors of epoxy resin. Bull. Polish Acad. Sci. Tech. Sci. 71(4), e146286 (2023). https://doi.org/10.24425/bpasts.2023.146286

Krzywiński, K., Sadowski, Ł, Fedoruk, K., Sieradzki, A.: Fundamental understanding of the thermal properties of amorphous epoxy resin coatings filled with quartz-feldspar powder sourced from quarry waste. Appl. Surf. Sci. 614, 156133 (2023). https://doi.org/10.1016/j.apsusc.2022.156133

Kumar Gupta, S., Kumar Shukla, D., Kaustubh Ravindra, D.: Effect of nanoalumina in epoxy adhesive on lap shear strength and fracture toughness of aluminium joints. J. Adhes. 97(2), 117–139 (2021). https://doi.org/10.1080/00218464.2019.1641088

Naghizadeh, Z., Faezipour, M., Pol, M.H., Liaghat, G.H., Abdolkhani, A.: Improvement in impact resistance performance of glass/epoxy composite through carbon nanotubes and silica nanoparticles. Proc. Inst. Mech. Eng. Part L: J. Mater. Des. Appl. 232(9), 785–799 (2018). https://doi.org/10.1177/1464420716649403

Ojha, S., Pranay, V., Raghavendra, G., Gara, D.: Experimental evaluation and comparison of silica/biocarbon particulate-epoxy composites for high-strength applications. Proc. Inst. Mech. Eng. Part L: J. Mater. Des. Appl. 236(1), 190–199 (2022). https://doi.org/10.1177/14644207211043506

PKN: ISO 868: 2003, Plastics and ebonite—determination of indentation hardness by means of a durometer (shore hardness). Warsaw, Poland (2003)

PKN: PN-EN 1504-2:2006 Products and systems for the protection and repair of concrete structures—definitions, requirements, quality control and evaluation of conformity—part 2: surface protection systems for concrete. Warsaw, Poland (2006)

Rzeczkowski, P., Pötschke, P., Fischer, M., Kühnert, I., Krause, B.: Graphite modified epoxy-based adhesive for joining of aluminium and PP/graphite composites. J. Adhes. 96(1–4), 229–252 (2020). https://doi.org/10.1080/00218464.2019.1688152

Thamizh Selvan, R., Vishakh Raja, P., Mangal, P., Mohan, N., Bhowmik, S.: Recycling technology of epoxy glass fiber and epoxy carbon fiber composites used in aerospace vehicles. J. Compos. Mater. 55(23), 3281–3292 (2021). https://doi.org/10.1177/00219983211011532

Waseem, S.A., Manzoor, Z., Bhat, J.A.: An experimental investigation into the behavior of steel-timber composite beam. Pract. Periodical Struct. Des. Constr. 27 (2021). https://doi.org/10.1061/(ASCE)SC.1943-5576.0000636

Experimental Validation of the Characterisation of Highly Flexible Adhesives Using Multiple Specimen Configurations

F. J. Simón-Portillo, O. Cuadrado, E. A. S. Marques, M. Sánchez-Lozano, and Lucas F. M. da Silva

Abstract The mechanical characterisation of adhesives with hyperelastic behaviour is complex task and the accuracy of these material modes should be validated in joints subjected to different types of stress. In a previous work by the authors, the hyperelastic behaviour laws of the adhesive were determined and validated by means of the Single Lap Joint (SLJ) test. As a result, it was determined that the Mooney Rivlin model provides the best fit for the adhesive behaviour. The current work expands upon this by first carrying out an experimental analysis of the behaviour of the adhesive under cleavage loads, using the Double Cantilever Beam (DCB) specimen configuration and then assessing the behaviour of the adhesive under tension using a T specimen configuration. In both cases, the response of the adhesive two different adhesive thickness values are analysed. The second part focuses on the validation of the Mooney Rivling behavioural law that has been previously proposed, assessing its effectiveness under tensile and tearing stresses. Finite element models are then developed and compared with the experimental results obtained in the first part.

F. J. Simón-Portillo (✉) · O. Cuadrado · M. Sánchez-Lozano
Department of Mechanical and Energy Engineering, Miguel Hernandez University, 03202 Elche, Spain
e-mail: f.simon@umh.es

O. Cuadrado
e-mail: o.cuadrado@umh.es

M. Sánchez-Lozano
e-mail: msanchez@umh.es

E. A. S. Marques
Instituteof Science and Innovation in Mechanical and Industrial Engineering (INEGI), Rua Dr. Roberto Frias, 4200-465 Porto, Portugal
e-mail: emarques@inegi.up.pt

L. F. M. da Silva
Department of Mechanical Engineering, Faculty of Engineering, University of Porto, 4200-465 Porto, Portugal
e-mail: lucas@fe.up.pt

15

Keywords Finite Element · Hyperelastic Models · Traction · Peel · Polyurethane

1 Introduction

The use of adhesives has grown substantially in various industrial fields, especially in the marine, aerospace and automotive sectors (Cavezza et al. 2020; Amstutz et al. 2018; Lu et al. 2014). The increasing need for lightweight structures has led industries to adopt larger amounts of composite materials, seeking to develop more efficient products through the exploitation of their optimal specific mechanical properties of composites (Mazlan et al. 2022; Pathak and Dhakate 2022). Although composites have many important advantages, traditional joining techniques, such as bolted joints, often involve operations such as drilling that may cause damage to these materials. Thus, the use of adhesives is preferred for composite structures (da Silva and Campilho 2015). Adhesive bonding also allows for a more uniform stress distribution in the bondline and, may also prevent corrosion of substrates due to its inherent sealing properties. In recent years, highly flexible structural adhesives have reached the market and have also gained importance. These adhesives behave similarly to rubber and other elastomers and are able to undergo large changes in shape without any permanent deformation or damage, making them ideal for applications requiring flexibility and strength (Loureiro et al. 2010; Banea and Da Silva 2009; Lubowiecka et al. 2012). The characterization of the mechanical properties of highly flexible adhesives is still relatively unexplored, especially under different types of stresses (Domingues et al. 2015; Galvez et al. 2017).

Although adhesives are primarily designed to resist shear forces, mechanical components often face different conditions and loading modes during their lifetime. Therefore, it is essential to carry out studies of the performance of adhesive bonds under different conditions (Da Silva et al. 2012; Banea and Da Silva 2009). In this work, joints subjected to tearing and tensile stresses are analysed in order to understand their behaviour under these stresses.

In order to ensure that adhesive joints can perform satisfactorily in structural applications, it is essential to model and optimise the joint performance. The use of finite element modelling (FEM) is a powerful tool at the disposal of the bonded joint designer. However, even highly advanced models are unable to accurate and reliable results without precise material characterisation data (Narayana Naik 2019; Campilho 2013). This is especially true for highly flexible adhesives, with non-linear elastic behaviour in the large strain range that can only be successfully described through hyperelastic material constitutive models (Hesebeck and Wulf 2018; Holzapfel 2000; Kim et al. 2012; Chiminelli et al. 2019). Such models account for the large deformation levels reached by these adhesives before failure. The fitting of the hyperelastic model and the validation of the model using SLJ specimens of different adhesive thicknesses was carried out by the authors in a previous work, pending publication. In this work, the Mooney Rivlin model was found to be the best fit for determining the behavioural law of this type of adhesive, fitted only using

the results of two simple mechanical characterisation tests of the adhesive. With the adjusted constants, the simulation of the behaviour of the adhesive under different loading conditions should also be achieved, being this the main objective that drives this work.

The first part of this research consists of an experimental study on the mechanical behaviour of the adhesive, with an analysis of how the adhesive thickness influences the cleavage and tensile behaviour (Banea et al. 2014). Firstly, specimens with adhesive thicknesses of 2, 3, 4 and 6 mm were tested using the double cantilever beam (DCB) configuration, providing a cleavage type of loading. Subsequentially, tensile tests were carried out using T-shaped specimens with 4 and 6 mm thick adhesive layers.

Finally, in order to validate the material model under generic tensile and cleavage loads, finite element models of the joints were developed, using the behavioural law fitted in the aforementioned previous investigations and then validated against experimental data.

2   Materials and Methods

The adhesive considered for this research is a single-component polyurethane (PUR) adhesive, Sikaflex 252, designed for use in highly flexible joints. This type of adhesive cures by reacting with moisture, forming a high performance elastomer (Kordová et al. 2022).

As mentioned in the previous section, two types of specimens are used in this research. These are described in the following paragraphs.

- Traction

The joints were manufactured with an adhesive surface measuring 50×50 mm. To ensure a precise alignment between the two adhesives and to be able to properly control the thickness of the adhesive, a special 3D printed tooling has been designed, as shown in Fig. 1. Aluminium is used as an adherend, with a modulus of elasticity of 70 GPa.

- Cleavage

The specimen used for the cleavage test was manufactured using the DCB configuration, with a width of 25 mm and a length of 100 mm. The details of this configuration are shown in Fig. 2. These joints were manufactured following some of the guidelines set out in ASTM D3433. The adherends were made of steel, with a Young's modulus of 200 GPa.

In this study, the aim is to ensure that almost all of the deformation takes place within the adhesive layer. Therefore, adhesives that are sufficiently rigid to avoid their deformation have been designed in both configurations.
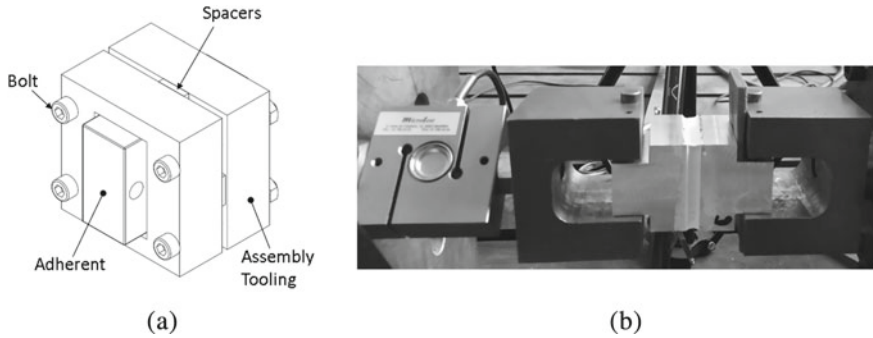
Fig. 1 Tensile joint fabrication tooling (**a**), test equipment (**b**)
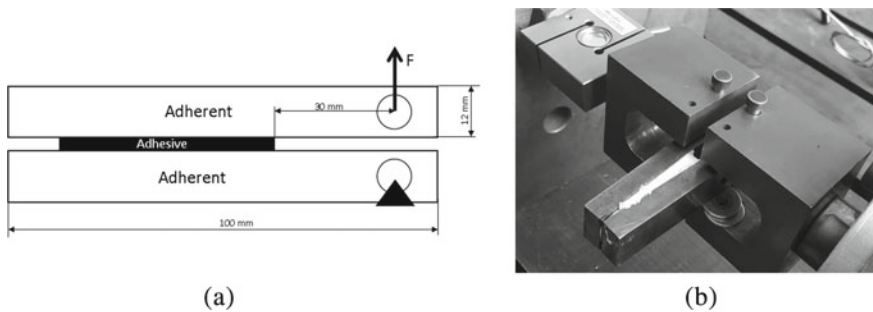
Fig. 2 Tear test tube (DCB) (**a**), test equipment (**b**)

To control the thickness of the adhesive, calibrated spacers coated with a release agent were used. To ensure a good level of adhesion and following the adhesive manufacturer's specifications, an adhesion promoter, in this case Sika Primer 206, was applied to both the steel and aluminium specimens. All tests were carried out under laboratory conditions (temperature of 23 °C and relative humidity 70%) using a testing machine equipped with a 20 kN load cell, with a controlled displacement rate of 10 mm/min.

3   Results and Experimental Discussion

In this section, the results of the quasi-static tests carried out are presented and analysed. Cleavage tests were carried out using double cantilever beam (DCB) specimens with adhesive layer thicknesses of 2, 3, 4 and 6 mm. Tensile tests were also carried out using the T-probe configuration, with adhesive thicknesses of 4 and 6 mm. Following the conclusion of the tests, cohesive failure was observed in all cases, indicating the successful selection of the surface treatment.
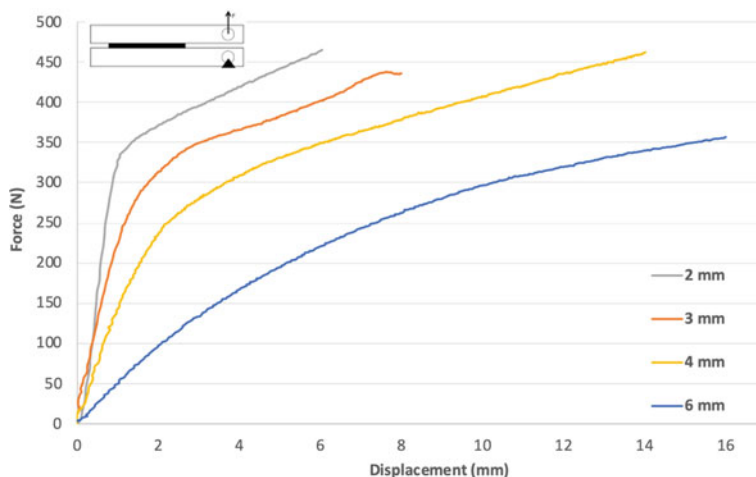
Fig. 3 Experimental results for DCB specimens with bondline thicknesses of 2, 3, 4 and 6 mm of SikaFlex 252

Figure 3 shows the force–displacement curves for the DCB tests, as function of the adhesive thickness. It can be seen that as the adhesive thickness decreases, the slope of the curves increases, indicating that the bond stiffness increases progressively. For the DCB specimen configuration and adhesive thicknesses of 2.3 and 4 mm, it can be seen that the load increased almost linearly with displacement in the initial phase, before reaching its strength limit and leading to failure of the adhesive layer.

Figure 4 shows the force–displacement curves corresponding to the tensile tests conducted with 4 and 6 mm adhesive thicknesses. In this case, it is also observed that as the adhesive thickness decreases, the slope of the curves slightly increases. In this type of joint, the level of stress required to initiate adhesive fracture is similar for both thicknesses. However, there is a difference since, for the 6 mm thick adhesive layer, fracture occurs with at a larger displacement, compared to the thinner adhesive.

In summary, the results obtained from the tear tests are shown in Table 1, and the results from the tensile tests in Table 2. This table gives the values of the maximum loads and displacements at the instants before fracture occurred in the adhesive, thus providing an overview of the experimental results obtained in the tests.

4 Comparison Between Experimental and Numerical Results

To obtain the constants of the hyperelastic models of order 1 and 2, stress–strain curves in two different loading configurations are first required (Crocker et al. 1999; Moreira and Nunes 2013). A uniaxial tensile test with halter specimens and a planar test, also known as "pure shear", have been chosen. It is highly recommended to
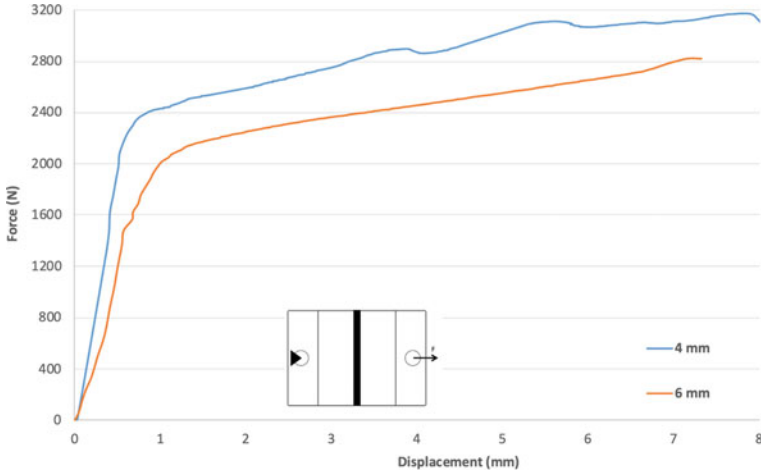
Fig. 4 Experimental results for tensile joints with thicknesses of 4 and 6 mm of SikaFlex 252

Table 1 Results for experimental DCB tests

DCB	Force max (N)	Displacement (mm)
2 mm	330	0.46
3 mm	275	1.8
4 mm	250	2.1
6 mm	150	3.5

Table 2 Results for experimental T-tensile tests

T	Force max (N)	Displacement (mm)
4 mm	2380	0.8
6 mm	2015	1

include the latter test in the characterisation of hyperelastic materials so that the shear behaviour of the material can be taken into account. The material models considered were: Neo-Hookean, Mooney-Rivlin (polynomial $N = 1$) and Ogden ($N = 1$ and $N = 2$) (Crocker et al. 1999; Duncan and Crocker 2001). It should be noted that, in this case, the compressibility constants are zero for any of the models, since it is assumed that this is an incompressible material. As mentioned above, the hyperelastic model has been adjusted and validated in previous investigations, pending publication.

As an example, Fig. 5 shows the validation results using the SLJ specimen with an adhesive thickness of 3 mm. This initial validation provides evidence of the model's ability to accurately represent adhesive behaviour in this bond configuration.

As part of the validation of the adhesive characterisation, modelling of DCB specimens with the geometries described in point 2 was carried out, using adhesive thicknesses of 4 and 6 mm. This modelling process aims to evaluate the accuracy
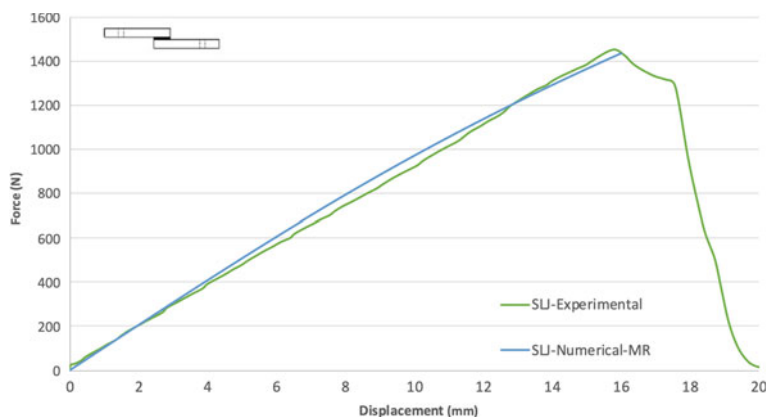
Fig. 5 Experimental results for SLJ-3 mm SikaFlex 252

and validity of the adhesive characterisation process, verifying whether the model is able to accurately predict the behaviour of the adhesive in the joints under different loads.

Following a similar methodology as that used to create a model of the SLJ specimen, a 3D finite element model was developed to validate both specimen configurations. Quasi-static analysis was carried out using Abaqus software. The steel for the DCB specimens is considered as a linear material. The mechanical properties of the adhesive are assumed according to the previously fitted hyperelastic model; using the Mooney-Rivlin model to define the constitutive law. Quadratic hexahedral elements with reduced integration were used in order to reduce the mesh density without affecting the accuracy of the solution. Additionally, a mesh convergence study was performed to determine the optimal element size in each case.

The boundary conditions were defined as shown in Fig. 6. One end is embedded, allowing rotation, while a displacement is applied at the other end, also allowing rotation. The force–displacement response was analysed up to a displacement range of 2 mm for the specimen with an adhesive thickness of 4 mm and 3 mm for the specimen with an adhesive thickness of 6 mm.

The results obtained from the simulation show an acceptable correlation with the experimental results for both specimen configurations, up to moments prior to adhesive failure. This indicates that the Mooney-Rivlin model used is adequate for defining the behaviour of the adhesive under tearing loads. Going into more detail in each of the configurations, as can be seen in Fig. 7, the slopes of the experimental and numerical curves are very similar in each of them.

In the simulations, the adhesive deformation (δ) in the direction of adhesive thickness was assessed (Fig. 6). In the case of the specimen with an adhesive thickness of 4 mm, an adhesive deformation of 1.2 mm was observed with no evidence of damage. For the 6 mm specimen, a deformation of 3 mm was achieved. These results indicate
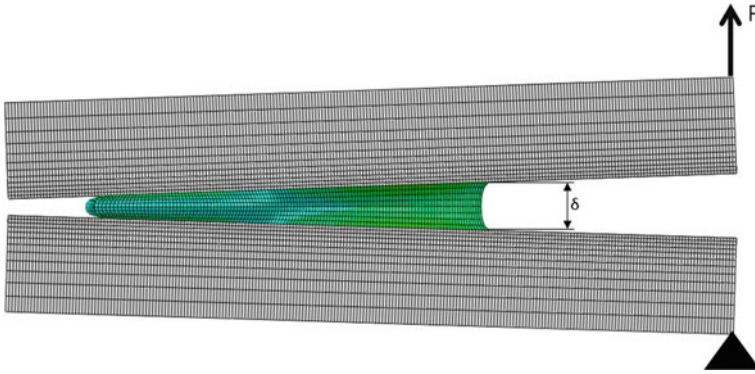
Fig. 6 FE simulation DCB
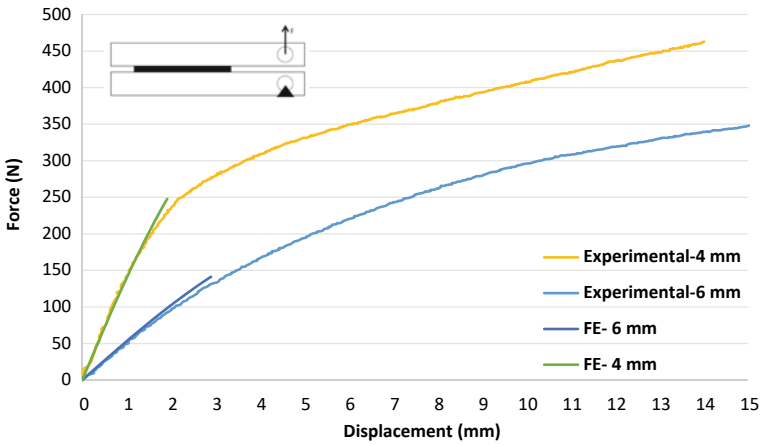
Fig. 7 Experimental results for DCB 4–6 mm bonding of SikaFlex 252

the ability of the adhesive to deform and absorb loads before reaching a critical point of damage.

5 Conclusions

In view of the results obtained, the Mooney Rivlin hyperelastic model has been found to be able to reproduce the behaviour of joints subjected to tearing load with a fair degree of accuracy. These results support the validity of the model and demonstrate its ability to predict adhesive performance in similar situations.

In light of these results, the mechanical characterisation process of the flexible adhesive has been satisfactorily completed. The results obtained provide a solid

understanding of the behaviour of the adhesive under different loading conditions and adhesive thicknesses.

The mechanical characterisation of the adhesive at high temperatures and the fracture characterisation of the highly flexible adhesive are proposed as future lines of work. These lines of work will contribute to improve the understanding of adhesives in different scenarios and to develop more efficient solutions adapted to different conditions of use.

References

Amstutz, C., Bürgi, M., Jousset, P.: Characterisation and FE simulation of polyurethane elastic bonded joints under multiaxial loading conditions. Int. J. Adhes. Adhes. **83**, 103–115 (2018). https://doi.org/10.1016/J.IJADHADH.2018.02.029

Banea, M.D., Da Silva, L.F.M.: Adhesively bonded joints in composite materials: an overview. Proc. Inst. Mech. Eng. Part L: J. Mater. Des. Appl. **223**(1), 1–18 (2009). https://doi.org/10.1243/14644207JMDA219

Banea, M.D., Da Silva, L.F.M., Campilho, R. D.S.G.: The effect of adhesive thickness on the mechanical behavior of a structural polyurethane adhesive. J. Adhes. **91**(5), 331–346 (2014). https://doi.org/10.1080/00218464.2014.903802

Campilho, R.D.S.G., Banea, M.D., Neto, J.A.B.P., Da Silva, L.F.M.: Modelling adhesive joints with cohesive zone models: effect of the cohesive law shape of the adhesive layer. Int. J. Adhes. Adhes. **44**, 48–56 (2013). https://doi.org/10.1016/j.ijadhadh.2013.02.006

Cavezza, F., Boehm, M., Terryn, H., Hauffman, T.: A review on adhesively bonded aluminium joints in the automotive industry. Metals (2020). https://doi.org/10.3390/met10060730

Chiminelli, A., Valero, C., Lizaranzu, M., López, C.I., Canales, M.: Modelling of bonded joints with flexible adhesives. J. Adhes. **95**(5–7), 369–384 (2019). https://doi.org/10.1080/00218464.2018.1562347

Crocker, L.E., Duncan, B.C., Hughes, R.G., Urquhart, J.M.: Hyperelastic modelling of flexible adhesives (1999). https://www.researchgate.net/publication/281283309_HYPERELASTIC_MODELLING_OF_FLEXIBLE_ADHESIVES

Domingues, N.R.E., Campilho, R.D.S.G., Carbas, R.J.C., Da Silva, L.F.M.: Experimental and numerical failure analysis of aluminium/composite single-L joints (2015). https://doi.org/10.1016/j.ijadhadh.2015.10.011

Duncan, B., Crocker, L.: Characterisation of Flexible Adhesives for Design. The National Physical Laboratory (NPL) (2001). https://doi.org/10.47120/npl.mgpg45

Galvez, P., Quesada, A., Martinez, M.A., Abenojar, J., Jesus, M., Boada, L., Diaz, V.: Study of the behaviour of adhesive joints of steel with CFRP for its application in bus structures (2017). https://doi.org/10.1016/j.compositesb.2017.07.018

Hesebeck, O., Wulf, A.: Hyperelastic constitutive modeling with exponential decay and application to a viscoelastic adhesive. Int. J. Solids Struct. **141–142**, 60–72 (2018). https://doi.org/10.1016/J.IJSOLSTR.2018.02.011

Holzapfel, G.A.: Nonlinear Solid Mechanics : A Continuum Approach for Engineering, p. 455. Wiley (2000)

Kim, B., Lee, S.B., Lee, J., Cho, S., Park, H., Yeom, S., Park, S.H.: A comparison among Neo-Hookean model, Mooney-Rivlin model, and Ogden model for chloroprene rubber. Int. J. Precis. Eng. Manuf. **13**(5), 759–764 (2012). https://doi.org/10.1007/s12541-012-0099-y

Kordová, T., Mareška, A., Míka, M.H.: Experimental analysis on the curing and adhesive behaviour of standard moisture-cured and fast-cured polyurethanes used in automotive industry. Manuf. Technol. **22**(2), 168–179 (2022). https://doi.org/10.21062/MFT.2022.029

Loureiro, A.L., Da Silva, L.F.M., Sato, C., Figueiredo, M.A.V.: Comparison of the mechanical behaviour between stiff and flexible adhesive joints for the automotive industry. J. Adhes. **86**(7), 765–787 (2010). https://doi.org/10.1080/00218464.2010.482440

Lu, Y., Broughton, J., Winfield, P.: A review of innovations in disbonding techniques for repair and recycling of automotive vehicles. Int. J. Adhes. Adhes. (2014). https://doi.org/10.1016/j.ijadhadh.2014.01.021

Lubowiecka, I., Rodríguez, M., Rodríguez, E., Martínez, D.: Experimentation, material modelling and simulation of bonded joints with a flexible adhesive. Int. J. Adhes. Adhes. **37**, 56–64 (2012). https://doi.org/10.1016/j.ijadhadh.2012.01.010

Mazlan, N., Chai Hua, T, Sapuan, S.M., Ilyas, R.A.: Evolution of aerospace composite materials. Adv. Compos. Aeros. Eng. Appl. 367–385 (2022). https://doi.org/10.1007/978-3-030-88192-4_18/FIGURES/4

Moreira, D.C., Nunes, L.C.S.: Comparison of simple and pure shear for an incompressible isotropic hyperelastic material under large deformation. Polymer Testing. Accessed July 3, 2021. https://www.sciencedirect.com/science/article/pii/S0142941812002218

Narayana Naik, G.: Single and dual adhesive bond strength analysis of single lap joint between dissimilar adherends (2019). https://doi.org/10.1016/j.ijadhadh.2019.04.016

Pathak, A.K., Dhakate, S.R.: Carbon nanomaterial-carbon fiber hybrid composite for lightweight structural composites in the aerospace industry: synthesis, processing, and properties. Adv. Compos. Aeros. Eng. Appl. 445–470 (2022). https://doi.org/10.1007/978-3-030-88192-4_23/TABLES/3

da Silva, L.F.M., Campilho, R.D.S.G.: Design of adhesively-bonded composite joints. Fatigue Fract. Adhes.-Bonded Compos. Joints 43–71 (2015). https://doi.org/10.1016/B978-0-85709-806-1.00002-1

da Silva, L.F.M., Dillard, D.A., Blackman, B., Adams, R.D.: Testing adhesive joints: best practices (2012)

Adhesion and Surface Treatments

The Effect of Adhesive Strength on Thin-Walled Metal Surfaces Coated with Cataphoresis Application According to Adhesive Thickness

C. Baykara

Abstract Every day, new types of lighter and more durable materials are being discovered for use in production. The methods of processing and joining these materials are also developing in parallel. Therefore, in addition to the development of materials and processing methods, some new regulations in joining processes also play an important role. The adhesion strength of thin-walled specimens that had primer paint and cataphoresis coating applied to them was investigated in this study in accordance with various adhesive thickness to increase the strength of the adhesive method. This investigation revealed that the adhesive bonding thickness and best surface coating in terms of adhesive strength, both of which were seen in the experiment. It is considered that it will play an important role in producing lower weight vehicles by joining different materials making them stronger.

Keywords Reducing to Vehicle Weight · Adhesive Bonding · Cataphoresis Coating Process · Primer Painting Process · Fatigue Analysis

1 Introduction

When using the adhesive method, instead of point contact such as spot welding, riveting and bolting a continuous connection occurs throughout. In addition it provides a homogeneous stress distribution throughout the joint area in bonded joints and good fatigue resistance, due to reducing stress at the joint edges. It also has high shear strength, noise, and vibration during impact (Boban et al. 2023; Yildirim et al. 2023). Its importance in almost every sector of the industry is increasing as time goes by as it provides many advantages such as having a good insulating feature against corrosion (Nasresfahani and Asghari 2023), also preventing contaminants (Gaviolli et al. 2021) entering the joints when joining different types of materials

C. Baykara (✉)
Sakarya University of Applied Science, Technology Faculty, Mechanical Engineering, Sakarya, Türkiye
e-mail: cbaykara@subu.edu.tr

(Baykara 2023). After performing many experimental results it has revealed that overall strength is greatly affected by adhesive thickness (Chen et al. 2023) and adhesive type (Giv et al. 2023) so with the bonding technique adhesive thickness is one of the most important factors for a durable bond to occur.

In addition many researchers have stated that using a tapering end will reduce interfacial tension concentrations (Bouchikhi et al. 2013; Kaufmann and Vallee 2022), the strength and elasticity modulus of the adhesive element (Dengiz and Dödüncü 2023; Mandal et al. 2004), surface roughness (Zhang and Huang 2021; Zhao et al. 2023), primer painting (Baykara 2023; Cui et al. 2021). Also, there are many basic parameters that constitute a new active surface by pre-treatment on the adhesion surface plasma treatment (Shin et al. 2022; Sundriyal et al. 2020) and corona-discharge treatment (Komagata et al. 2020; Zanet et al. 2022).

In this study, a different pre-treatment that replaces the conventional ones is applied to the surface area, such as primer painting, acid bath, fire etching, mechanical roughness and corona treatments, this will be investigated. An alternative application is to apply cataphoresis coating to the adhesion surface instead of conventional methods (Baykara 2023).

The bonding method in some of the automobile industry is widely used. Customers are more accustomed to luxury and security due to this. Also these requirements add weight to the car. These weights boost the fuel ratio in internal combustion vehicles that are constructed today. The cost of fuel and the amounts of CO_2 that are released into the atmosphere by motor vehicles rise as a result of the increase in fuel ratio (Zhang and Xu 2022). Internal combustion vehicles will be phased out in favour of electric vehicles over the next few years. The mobility capabilities and range of these electric vehicles is significantly affected by the addition of heavy items like batteries and hydrogen tanks so for these reasons vehicle manufacturers have been working hard to produce lighter vehicles. The automotive industry is currently working to meet both the conflicting requirements of environmental legislation and customers demands for better performance, more luxury and safety features by developing a lightweight and energy efficient vehicle (Watson et al. 2019; Kim and Cho 2020). Due to this the automobile industry are working to make their vehicles lighter by focusing on specific elements made of different materials like aluminium alloys, a derivative of composite materials. According to studies the body of a vehicle weighs between 20 and 30% of its overall weight, materials such as steel and aluminum give a considerable joining method issue due to their physical and chemical characteristics. Therefore, the welding method can't be used due to their melting points are different for steel and aluminum. It is also necessary to drill a hole in the part to be joined with the bolt and this hole causes the material to weaken so this is why the adhesive method is used to join two different materials. When aluminum series is to be used instead of steel it requires it to be thicker than the steel material (Zhang and Xu 2022).

Customers are increasingly demanding luxury and safety from vehicle manufacturers and these demands naturally cause the weight of the vehicles to increase. For this reason, the fuel ratio increases as a result of the increase in the weight of fossil fuel

vehicles. The cost of fuel and the amounts of CO_2 that are released into the atmosphere by motor vehicles rise as a result of the increase in fuel ratio (Zhang and Xu 2022). Considering that internal combustion vehicles will be gradually be changed to electric vehicles over the next few years electric vehicle weights will be also significantly affected by increasing the mobility and range of electric vehicles also the addition of heavy parts such as batteries and hydrogen tanks. Therefore, automobile manufacturers need to make their vehicles lighter by focusing on components made of different materials, such as different types of aluminum alloys and derivatives of composite material such as FRP. This is why the adhesive bonding method for joining different materials is widely used in the automobile industry.

In this study, the impact of adhesive strength on two chemical treatments used in an automobile factory's painting workshop was investigated. In this section, the phrase "chemical treatment" refers to primer painting or cataphoresis coating. Cataphoresis coating is utilized to protect a car body, it is called Body in White (BIW), from corrosion and is one of these chemical processes. The primer painting that is applied to the car's body (BIW) after the cataphoresis procedure is the other chemical application. The adhesive bonding procedure was also investigated in thin-walled steel specimens that had been cataphoresis coated and primer painted in this research.

2 Materials and Experimental Preparations

In this research paper, fatigue tests will be performed on thin-walled steel specimens whose surface has been activated by different chemical processes and joined with different adhesive bonding thicknesses.

2.1 Materials

The test material used was cold-rolled steel type DC01A with a thickness of 0.8 mm. These types of steel are easier to form at low temperatures and within narrow tolerance ranges, have a smoother surface quality and can be welded with little difficulty. Such steels are frequently utilized in the automobile sector for engine parts, suspension system components, and vehicle bodies (BIW) due to their strength, durability, corrosion resistance, sustainability, light weight, and affordable price.

2.2 Surface preparation

The surfaces of steel test specimens were investigated in three different groups. The first group no chemical treatment such as coating or paint was applied to the surface of the steel specimens and the surfaces were left natural. A thickness of 0.30 µm

primer paint was applied to the second group of steel specimens. In the final group a thickness of $0.20\,\mu m$ cataphoresis coating was applied to the steel specimen surfaces.

2.3 Single-Lap Joint Preparation

The adhesive bonding method will be applied as a joining process on the surface of the prepared specimens. In joining the steel specimens in each group, single lap joint method with different bonding thicknesses of 1.5, 2.5 and 3.5 mm were used as the joining method according to ASTM D1002. In Fig. 1, the geometric sizes and joint detail are displayed. Polyurethane-based Sikaflex 252 is used as the adhesive element.

3 Experimental Test Method

In his earlier research, the author performed a fatigue test on cataphoresis coated specimens using adhesive thicknesses of 1.0, 2.0, 3.0, 4.0, 5.0, and 6.0 mm. The findings of this study showed that the value obtained in the fatigue tests under 0.10 and 0.15 kN load applied to the materials with a 2 mm adhesive thickness and a surface coated in cataphoresis was nearly identical to the result obtained in the single spot welded specimens (Baykara 2023). In this new study, the goal is to identify the most sensitive and effective adhesive thickness by comparing it to the findings from earlier experimental test (Baykara 2023) and numerical analyses (Baykara et al. 2023). The adhesive thicknesses of 1.5, 2.5, and 3.5 mm, which was the intermediate values of the previous adhesive thicknesses were used in an effort to obtain more accurate and sensitive data for the adhesive thickness parameter. The fatigue test device was used to apply the parts from each different groups at five different thresholds: 0.10, 0.15, 0.20, 0.25, and 0.30 kN in one direction. The results regarding the life cycle were then investigated. The environmental temperature during the ISO 9664 fatigue test was 23 °C (±5 °C), and the test's frequency was set to 1 Hz. The device was set to
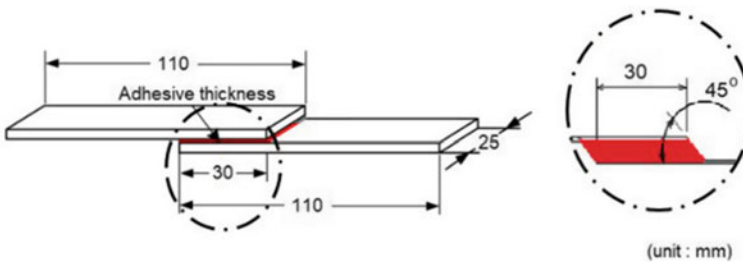
Fig. 1 Single lap joint in adhesive method (Baykara 2023)

return the specimen to its unloaded state after completing the tensile process during the cycle. The loading rate was applied in a one-way variable dynamic as (R = 0.1) to prevent damaging the adhesive element during the compressing operation. The loading value was set to 0.1 instead of −1 to prevent the high load during compression from replacing the bonding surface and damaging the test specimens.

3.1 Experimental Results

The following tables (Tables 1, 2, and 3) present the experimental findings of fatigue tests performed on grouped specimens with various surface groups and thickness.

Table 1 Fatigue test results of specimens without any chemical treatment (Group 1)

Adhesive thickness			
Load (kN)	1.5 (mm)	2.5 (mm)	3.5 (mm)
0.10	Not broken	Not broken	Not broken
0.15	Not broken	Not broken	Not broken
0.20	4257	3851	2578
0.25	1795	2624	2284
0.30	1574	2243	2196

Table 2 Fatigue test results of specimens painted with primer paint (Group 2)

Adhesive thickness			
Load (kN)	1.5 (mm)	2.5 (mm)	3.5 (mm)
0.10	Not broken	Not broken	Not broken
0.15	9282	Not broken	Not broken
0.20	6375	7349	6695
0.25	5489	5752	5447
0.30	4495	4536	4489

Table 3 Fatigue test results of specimens coated with catopheresis coating (Group 3)

Adhesive thickness			
Load (kN)	1.5 (mm)	2.5 (mm)	3.5 (mm)
0.10	Not broken	Not broken	Not broken
0.15	Not broken	Not broken	12,877
0.20	18,321	15,478	9652
0.25	11,553	9954	6820
0.30	9087	7473	4589

Table 4 The FEA based fatigue analysis results for specimens without any chemical treatment

Adhesive thickness			
Load (kN)	1.5 (mm)	2.5 (mm)	3.5 (mm)
0.10	10,000,000	10,000,000	10,000,000
0.15	200,000	100,000	100,000
0,20	10,000	10,000	5775
0.25	2592	2542	2306
0.30	1859	2218	2244

4   Numerical Analysis Results

For this part the numerical analysis tool Ansys was used to simulate the fatigue findings for the adhesive thicknesses of 1.5, 2.5, and 3.5 mm in the specimens classified according to the surface treatment.

4.1   FEA Based Fatigue Analysis Results for Specimens Without Any Chemical Treatment (Group 1)

The findings of the numerical analysis carried out on Ansys are displayed (Table 4 and Fig. 2) while taking into consideration the experimental parameters and the specimen characteristics without any chemical surface treatment.

In the FEA-based fatigue analysis it was found that thin-walled metal specimens when adhesive bonded by various adhesive thicknesses of 1.5, 2.5, and 3.5 mm demonstrated acceptable strength especially for 0,10 kN. It also demonstrates that it can endure a load of 0.15 kN for a considerable amount of time before failing under a load of 0.10 kN (Table 4 and Fig. 2). Additionally, infinite life was seen at all adhesive thicknesses under 0.10 and 0.15 kN loads when checking into the experimental test results in (Table 1).

4.2   FEA Based Fatigue Analysis Results for Specimens Painted with Primer Paint (Group 2)

Table 5 and Fig. 3 display the outcomes of the numerical analysis done on Ansys while accounting for the experimental parameters and the characteristics of the specimens painted with primer.

In the FEA analysis of this group, it has been noted that the specimens of each adhesive thickness exhibit an infinite life, particularly under a load of 0.10 kN, and a resistance within a certain duration under a load of 0.15 kN. The specimens with primer painted surfaces under loads of 0.20, 0.25, and 0.30 kN have
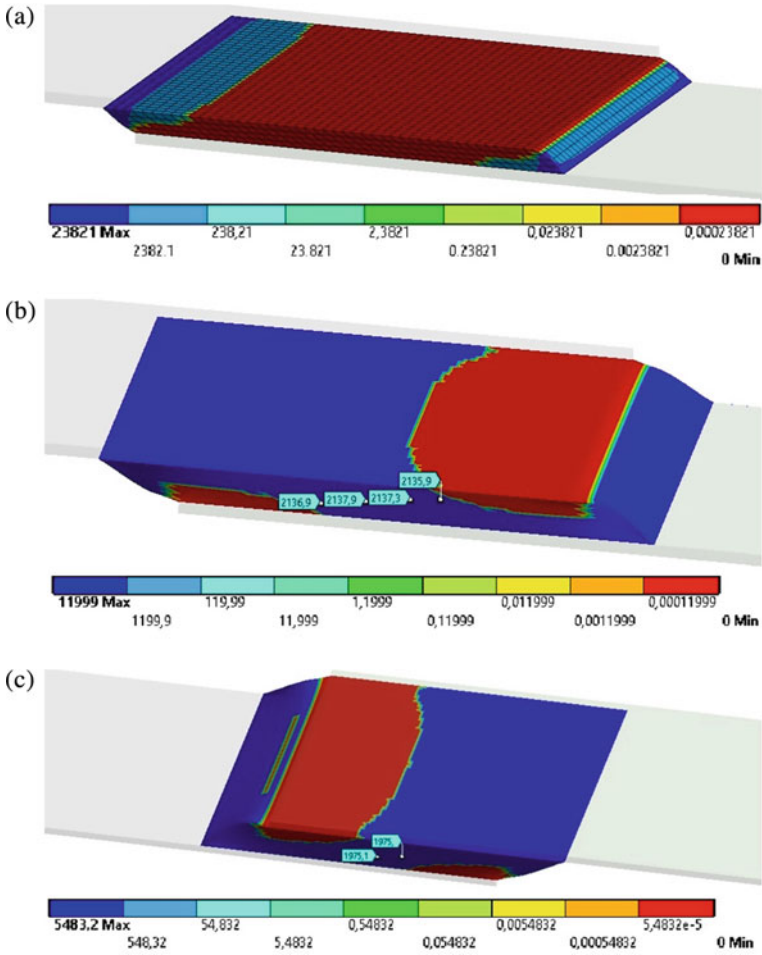
Fig. 2 FEA analysis images of the specimens without any chemical treatment on their surfaces according to adhesive thicknesses of **a** 1.5 mm, **b** 2.5 mm, and **c** 3.5 mm

Table 5 FEA based fatigue analysis results for specimens painted with primer painting

Adhesive thickness			
Load (kN)	1.5 (mm)	2.5 (mm)	3.5 (mm)
0.10	10,000,000	10,000,000	10,000,000
0.15	200,000	100,000	30,000
0,20	8922	10,776	10,000
0.25	6057	7441	6717
0.30	5573	6425	6080

Fig. 3 FEA analysis images of the specimens painted primer paint according to adhesive thicknesses of **a** 1.5 mm, **b** 2.5 mm, and **c** 3.5 mm

been found to have a longer cycle life than comparison of bare specimens s (Fig. 3 and Table 5). In addition to these FEA analysis results, infinite life was seen at all adhesive thicknesses under 0.10 and 0.15 kN loads in adhesive thickness of 2.5 and 3.5 mm. This observation was confirmed by experimental test results in (Table 2) as well. It was determined that the specimens with primed surfaces had a cycle life that was significantly longer than the specimens with bare surfaces at other increasing loads.

4.3 *FEA Based Fatigue Analysis Results for Specimens Coated with Cataphoresis Coating (Group 3)*

It has been noted from the FEA study findings for this category that the specimens of each adhesive thickness exhibit an infinite life, particularly under a load of 0.10 kN, and a resistance within a finite duration under a load of 0.15 kN. This observation

was confirmed by experimental test results in (Table 3) as well. The specimens s with cataphoresis-coated surfaces under loads of 0.20 kN, 0.25 kN, and 0.30 have been found to have a longer life cycle than those studies of specimens painted with primer (Fig. 4 and Table 6). In addition to these FEA analysis results, infinite life was seen on all adhesive thicknesses under 0.10 and 0.15 kN loads in adhesive thickness of 2.5 mm. Additionally, it failed with 3.5 mm of adhesive thickness under a 0.15 kN load. It was found that the specimens coated with cataphoresis coating had significantly longer life cycles than the specimens painted with primer paint at other increasing loads.

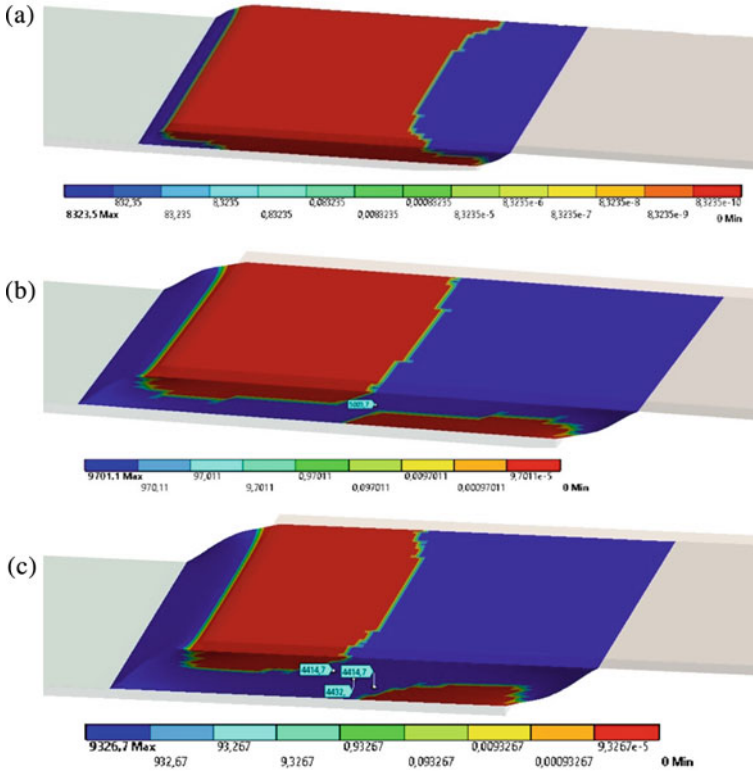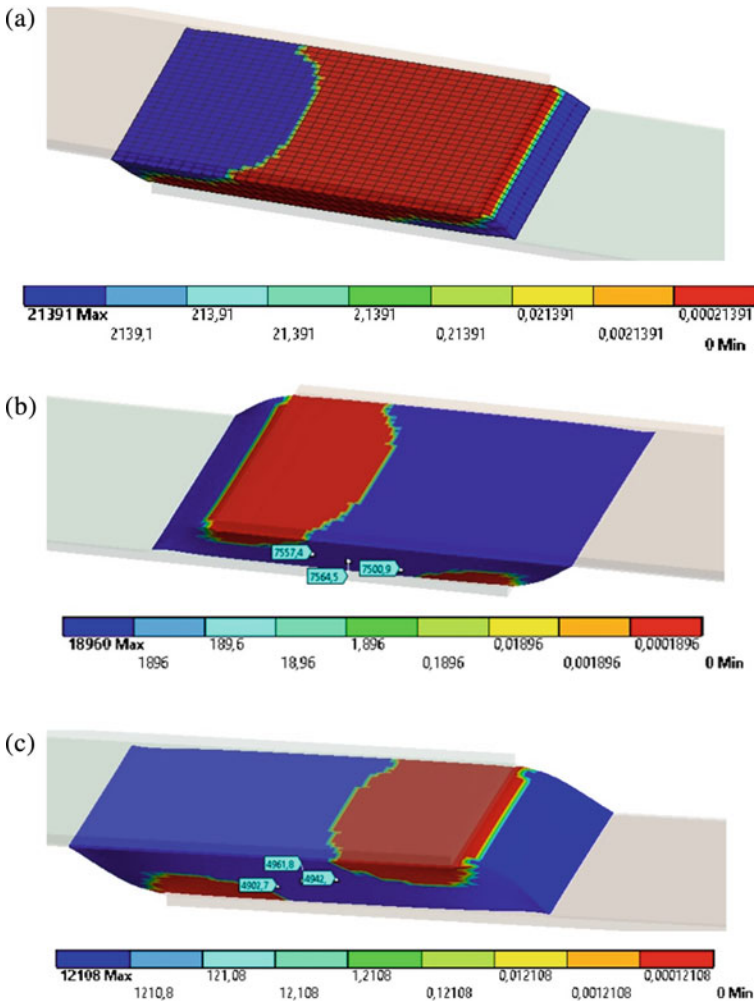**Fig. 4** FEA based fatigue analysis images of specimens coated with catopheresis coating according to adhesive thicknesses of **a** 1.5 mm, **b** 2.5 mm, and **c** 3.5 mm

Table 6 FEA based fatigue analysis results of specimens coated with catopheresis coating

Adhesive thickness			
Load (kN)	1.5 (mm)	2.5 (mm)	3.5 (mm)
0.10	100,000	10,000,000	10,000,000
0.15	200,000	100,000	30,000
0,20	25,000	21,426	13,483
0.25	18,123	16,540	9921
0.30	12,435	14,475	8626

4.4 Comparison Between Experimental and Numerical Results

Based on adhesion thicknesses both experimental and numerical fatigue data for specimens with various surfaces are displayed in Tables 7, 8, and 9. Examining the values in the tables reveals that the life cycle of the specimens with painted surfaces are more than the specimens with bare surfaces and the life cycle of the specimens coated with cataphoresis is even greater than the specimens with painted surfaces (Baykara 2023).

Table 7 Experimental and numerical fatigue results of all specimens at 1.5 mm adhesion thickness

Load (kN)	Bare surface		Surface painted		Surface coated	
	Experimental result	Numerical result	Experimental result	Numerical result	Experimental result	Numerical result
0.10	Not broken	10,000,000	Not broken	10,000,000	Not broken	100,000
0.15	Not broken	200,000	9282	200,000	Not broken	200,000
0.20	4257	10,000	6375	8922	18,321	25,000
0.25	1795	2592	5489	6057	11,553	18,123
0.30	1574	1859	4495	5573	9087	12,435

Table 8 Experimental and numerical fatigue results of all specimens at 2.5 mm adhesion thickness

Load (kN)	Bare surface		Surface painted		Surface coated	
	Experimental result	Numerical result	Experimental result	Numerical result	Experimental result	Numerical result
0.10	Not broken	10,000,000	Not broken	10,000,000	Not broken	10,000,000
0.15	Not broken	100,000	Not broken	100,000	Not broken	100,000
0.20	3851	10,000	7349	10,776	15,478	21,426
0.25	2624	2542	5752	7441	9954	16,540
0.30	2243	22,189	4536	6425	7473	14,475

Table 9 Experimental and numerical fatigue results of all specimens at 3.5 mm adhesion thickness

Load (kN)	Bare surface		Surface painted		Surface coated	
	Experimental result	Numerical result	Experimental result	Numerical result	Experimental result	Numerical result
0.10	Not broken	10,000,000	Not broken	10,000,000	Not broken	10,000,000
0.15	Not broken	100,000	Not broken	30,000	12,877	30,000
0.20	2578	5775	6695	1000	9652	13,483
0.25	2284	2306	5447	6717	6820	9921
0.30	2196	2244	4489	6080	4589	8626

5 Conclusions

In this study, the effects of surface coating and adhesive thickness on the fatigue performance of specimens joined with single lap joints and coated with various chemical applications were investigated.

Thin-walled metal specimens with surfaces joined without the use of any chemicals demonstrated strength at 0.10 kN force, according to experimental fatigue testing and numerical assessments. It failed when a force of specifically 0.15 kN was applied and it did not demonstrate adequate strength at other force values. Specimens s primed with primer paint in adhesive thickness of 1.5, 2.5, and 3.5 mm exhibited resistance at 0.10 and 0.15 kN of loads. When the loading was slightly raised to 0.30 kN, the specimen type failed. According to numerical study, the life cycle in adhesive thickness of 3.5 mm is 6080 at 0.30 kN load level for specimens that have been primed, whereas this number is 8626 life cycle for specimens that have undergone cataphoresis. If the experimental tests are looked at it can be found that these values are 4489 and 4589, respectively. Therefore, both experimental and numerical results confirm each other.

Therefore, it has been demonstrated once more taking into account the findings of this experiment that the cataphoresis bond is more robust in thin-walled adhesive bonded specimens than it was in specimens with wider adhesive thicknesses (Baykara, 2023). In a previous study, adhesive thicknesses of 1, 2, 3, 4, 5, and 6 mm in cataphoresis coated specimens were, had been determined effective adhesive thickness up to 2 mm. The adhesive thicknesses employed in this investigation were 1.5, 2.5, and 3.5 mm, which are intermediate levels from those used in previous studies. The effective adhesive thickness was thus found to be up to 2.5 mm. In other words thickness values were evaluated in this study using a more exact and precise scale. In this investigation, it was found that the effective bonding thickness may reach 2.5 mm, up from the previous research's maximum of 2 mm.

References

Baykara, C., Teke, I.T., Ertas, A.H.: Effects of the single-lap joint on fatigue strength of metals with different surface coatings: a numerical simulation. TransSiberia, E3S Web Conf. **402**, 11011 (2023). https://doi.org/10.1051/e3sconf/202340211011

Baykara, C.: Effects of single-lap joint at different adhesive thicknesses on fatigue strength of metals with different surface coatings. Proc. ImechE Part C: J. Mech. Eng. Sci. **237**(17), 1–18 (2023). https://doi.org/10.1177/09544062231152995

Boban, A., Kurian, S., Pooppally, T.J., Kumar, R.R. et al.: Numerical investigation on the strength of different types of adhesively bonded lap joints. Mater. Today Proc. **72**, 2255–2260 (2023). https://doi.org/10.1016/j.matpr.2022.09.213

Bouchikhi, A.S., Megueni, A., Gouasmi, S.: Effect of mixed adhesive joints and tapered plate on stresses in retrofitted beams bonded with a fiber-reinforced polymer plate. Mater. Des. **50**, 893 (2013). https://doi.org/10.1016/j.matdes.2013.03.052

Chen, K., Wu, Y., Han, W., et al.: Influence of adhesive thickness and defect on mechanical property of adhesive bonded joint of flexible polymer substrate and cable for solar panel application. Int. J. Adhes. Adhes. **126**, 103485 (2023). https://doi.org/10.1016/j.ijadhadh.2023.103485

Cui, E., Jiang, S., Wang, J. et al.: Bond behaviour of CFRP-concrete bonding interface considering degradation of epoxy primer under wet-drycycles. Constr. Build. **292**, 123286 (2021). https://doi.org/10.1016/j.conbuildmat.2021.123286

Dengiz, C.G., Dödüncü, M.: A unified phase-field approach for failure prediction in modulus graded adhesively bonded single-lap joints. Theoret. Appl. Fract. Mech. **127**, 104062 (2023). https://doi.org/10.1016/j.tafmec.2023.104062

Gaviolli, E., Vieire, E.O., da Silva, F.D., et al.: Influence of different contaminants and cleansing agents on bond strength and in situ degree of conversion of composite-adhesive interface. Int. J. Adhes. Adhes. **110**, 102932 (2021). https://doi.org/10.1016/j.ijadhadh.2021.102932

Giv, A.N., Chen, Z., Fu, Q.: Bending behavior and bond analysis on adhesively bonded glulam-concrete panels fabricated with wet bonding technique. J. Build. Eng. **76**, 107140 (2023). https://doi.org/10.1016/j.jobe.2023.107140

Kaufmann, M., Vallee, T.: Topology optimization of adhesively bonded double lap joints. Int. J. Adhes. Adhes. **118**, 103238 (2022). https://doi.org/10.1016/j.ijadhadh.2022.103238

Kim, J.W., Cho, J.U.: Fracture properties on the adhesive interface of double cantilever beam specimens bonded with lightweight dissimilar materials at opening and sliding modes. Compos. B **198**, 108240 (2020). https://doi.org/10.1016/j.compositesb.2020.108240

Komagata, Y., Ikeda, H., Fujio, Y., et al.: Surface modification of feldspar porcelain by corona discharge and its effect on bonding to resin cement with silane coupling agent. J. Mech. Behav. Biomed. Mater. **105**, 103708 (2020). https://doi.org/10.1016/j.jmbbm.2020.103708

Mandal, A.K., Chaudhary, A.K., Jain, V.: The effect of elastic modulus of adhesive on stress-distribution in weld bonded joint of Al6082-T6 sheets. Mater. Today: Proc. **44**, 1999–2004 (2004). https://doi.org/10.1016/j.matpr.2020.12.119

Nasresfahani, M.R., Asghari, S.: Review of nondestructive methods for evaluating adhesive bonding on anodized coatings. Int. J. Adhes. Adhes. **127**, 103491 (2023). https://doi.org/10.1016/j.ijadhadh.2023.103491

Shin, Y., Qiao, Y., Canfield, N., et al.: Significant slowdown of plasma-optimized surface energy deactivation by vacuum sealing for efficient adhesive bonding. Compos. B **240**, 110001 (2022). https://doi.org/10.1016/j.compositesb.2022.110001

Sundriyal, P., Pandey, M., Shantanu, B.: Plasma-assisted surface alteration of industrial polymers for improved adhesive bonding. Int. J. Adhes. Adhes. **101**, 102626 (2020). https://doi.org/10.1016/j.ijadhadh.2020.102626

Watson, B., Nadwani, Y., Worswick, M.: Metallic multi-material adhesive joint testing and modeling for vehicle lightweighting. Int. J. Adhes. Adhes. **95**, 102421 (2019). https://doi.org/10.1016/j.ijadhadh.2019.102421

Yildirim, C., Ulus, H., Beylergil, B., Nadhari, A., et al.: Effect of atmospheric plasma treatment on Mode-I and Mode-II fracture toughness properties of adhesively bonded carbon fiber/ PEKK composite joints. Eng. Fract. Mech. **289**, 109463 (2023). https://doi.org/10.1016/j.engfracmech.2023.109463

Zanet, A., Salvo, M., Casalegno, V.: Surface modification of SiC to improve joint strength via a Corona plasma treatment. Ceram. Int. **48**, 23492–23497 (2022). https://doi.org/10.1016/j.ceramint.2022.04.344

Zhang, D., Huang, Y.: Influence of surface roughness and bondline thickness on the bonding performance of epoxy adhesive joints on mild steel substrates. Prog. Org. Coat. **153**, 106135 (2021). https://doi.org/10.1016/j.porgcoat.2021.106135

Zhang, W., Xu, J.: Advanced lightweight materials for automobiles: a review. Mater. Des. **221**, 110994 (2022). https://doi.org/10.1016/j.matdes.2022.110994

Zhao, K., Hu, Z., Wang, B., Li, Q., Xu, Y.: Effect of roughness and adhesive on the strength of concrete-to-concrete interfaces cast from 3D-printed prefabricated plastic formworks. Constr. Build. Mater. **368**, 130423 (2023). https://doi.org/10.1016/j.conbuildmat.2023.130423

Adhesive Properties of Polyurethane Paint Coatings Modified with Multi Walled Carbon Nanotubes for Hardwood Protection

Karolina Brzozowska, Agnieszka Chowaniec-Michalak, Paweł Niewiadomski, and Łukasz Sadowski

Abstract The article presents the results of the adhesive properties of polyurethane paint coatings modified with Multi Walled Carbon Nanotubes for hardwood protection. The study shows how the addition of MWCN in proportions 0, 1, 2 and 4% affect the mechanical properties of the coating on oak wood substrates. Pull-off strength test, Shore D hardness test and cross-cut test were performed in this study. For the pull-off strength test, the highest average (5.76 MPa) was obtained for the addition of 1% of MWCN, while for the Shore D hardness test, it was obtained for the addition of 4% of MWCN (72.5). The addition of MWCN resulted in a slight improvement in hardness and increased the pull off strength of the coating.

Keywords Polyurethane coating · Multi walled carbon nanotubes · Wood · Adhesion · Hardness

1 Introduction

Wood is a material commonly used in construction, not only for structural reasons, but also for finishing. In terms of finishes, wood works for floors, stairs treads, walls and furniture. Often chosen wood is oak, which is characterized by such properties as

K. Brzozowska · A. Chowaniec-Michalak (✉) · P. Niewiadomski · Ł. Sadowski
Department of Materials Engineering and Construction Processes, Wroclaw University of Science and Technology, Wroclaw, Poland
e-mail: agnieszka.chowaniec@pwr.edu.pl

K. Brzozowska
e-mail: karolina.brzozowska@pwr.edu.pl

P. Niewiadomski
e-mail: pawel.niewiadomski@pwr.edu.pl

Ł. Sadowski
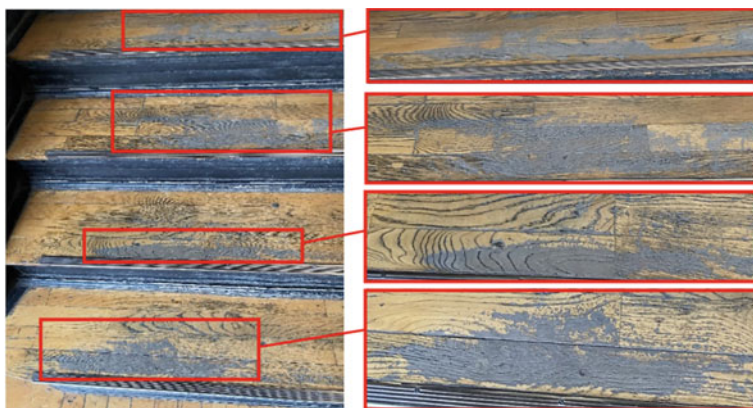e-mail: lukasz.sadowski@pwr.edu.pl

41

Fig. 1 View of wooden steps with abrasions caused by frequent foot traffic

above-average durability, high hardness, strength and abrasion resistance. As a result, it will perform on stair treads with high traffic, because these areas are particularly prone to higher usage, due to the movement of people mostly in the middle of the step (Fig. 1). For this reason, it is necessary to properly protect the wood, e.g. with suitable impregnations.

On today's market there is a huge selection of impregnates, used to protect wooden surfaces, which can be divided into air-drying, reaction-curing, water-soluble, stains, oils and paint coatings (Papadopoulsa et al. 2019). Of the aforementioned, paint coating is the most effective impregnator, as it protects against moist, mechanical damage and chemicals. Of all the paint coatings available today, polyurethane paint coating is the most common choice, due to its high hardness coefficient and abrasion resistance. However, coatings, even the highest ones trough use deteriorate over time. In addition, in order to reduce the weak points of wood, related to sensitivity to moist, low resistance to biological destruction (termites, fungi), modifications of coatings are used (Sandberg et al. 2017).

Research involving the addition of nanoparticles not only to buildings materials (Sobolev 2015), but also to coatings that protect wood surfaces in order to improve their properties, is increasingly being conducted. In Zvekić et al. (2011), ZnO nanoparticles were added to polyurethane varnish, which significantly inhibit microbial activity. In Zhu et al. (2023), the addition of silica sol to UV-curable waterborne acrylic improved the abrasion resistance, hardness and impact resistance mechanical properties of the coating.

Although new materials are emerging in the field of nanotechnology, carbon nanotubes are the most promising of all nanoparticles (Saeed 2013). Carbon nanotubes are divided into those consisting of a single layer—Single Wall Carbon Nanotubes (SWCN) and multiple walls—Multi Wall Carbon Nanotubes (MWCN). Due to their unique properties such as small size, high strength (Nochaiya and Chaipanich 2011), average Young's modulus of about 1000 GPa or deformation

od 12% (Hu et al. 2014), they are eagerly used as an additive for construction materials. In studies conducted, the addition of 0.045% carbon nanotubes to concrete increased compressive strength and tensile strength by 26.69% (Madhavi et al. 2013) or improved flexural strength and ductility (Abu et al. 2012). The application of 2% carbon nanotubes to an asphalt mixture improved the mixture's rheological properties, resistance to permanent deformation and fatigue strength (Staub de Melo et al. 2018; Azarhoosh et al. 2022). In Dehghan et al. (2014) 2% of MWCN, which were dispersed using Triton, were added to epoxy. The addition improved the tensile strength of epoxy (33%) and increased the elastic modulus (26%). Kaymakci et al. (2016) showed that as the amount of MWCN increased, the flexural and tensile properties of wood polymer nanocomposites increased. David et al. (2022) showed that treatment methods based on MWCN with the addition of zinc oxide, the addition of silver nanoparticles dispersed in a solution of poly(3-hydroxybutyrate-co-hydroxyvalerete) on oak wood primers significantly improved the compressive strength of the tested samples.

Based on the literature review, which indicates a significant interest in the topic of carbon nanotubes as an additive to various materials and coatings, it was decided to study the effect of MWCN on the mechanical properties of the coating. Analyzing the literature, it was also noted that there are not many studies involving the addition of MWCN to polyurethane coatings for wood protection, including a study that was conducted on softwood samples (Brzozowska and Chowaniec 2023), in which a pull-off strength test for 1 and 4% MWCN content showed a slight increase for pine samples. However, no studies were found in which only carbon nanotubes (without additives in the form of other nanoparticles) were used for a polyurethane coating to protect hardwood surfaces. Due to unique properties of the MWCN, it was decided to study their influence on the mechanical properties of the tested coating using the pull-off strength test, cross-cut test and Shore D hardness test. The focus was on the pull-off strength test and cross-cut test due to the importance of proper adhesion of the coating to the wood substrate to prevent delamination. It was also decided to test the hardness of the coating using Shore D hardness because it ensures the durability of the coating during use.

2 Materials and Methods

2.1 Materials

The wood used for this study is hardwood—oak (*Quercus* L.) is a species of wood that is characterized by high durability, compressive strength and tensile strength (along the fibers), or high hardness.

Of the available polyurethane paint coatings, the frequently used HartzLack Super Strong HS Gloss was selected, which mostly consists of n-butyl acetate (15–12%),
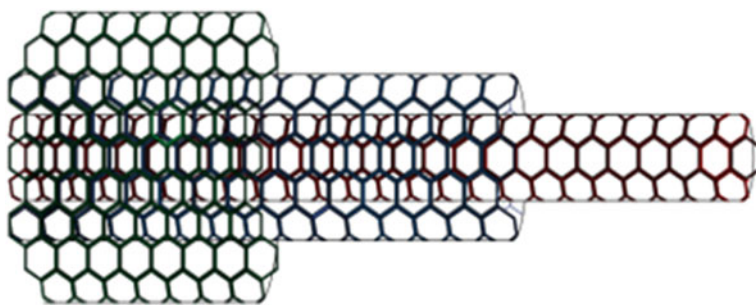
Fig. 2 Schematic drawing of MWCN

Table 1 Mix proportions of the polyurethane paint coating with MWCN (ration in g/100 g of thenmixture)

Materials	P-C0 (g)	P-C1 (g)	P-C2 (g)	P-C4 (g)
Polyurethane varnish (P)	100	99	98	96
Carbon nanotubes (C)	0	1	2	4

xylene (8–12%), aromatic polisocyanate (11–15%), polisocyanate prepolymer (1–11%).

MWCN were selected from the available types of carbon nanotubes, which were purchased from Cheap Tubes Inc. (Brattleboro, VT, USA) (Fig. 2). From the producer's information, it is known that their outer diameter 30–50 nm, inner diameter 5–10 nm, length 10–20 μm, specific surface area 60 m^2/g and true density 2.1 g/cm^3.

2.2 Mix Proportions

Table 1 shows the mixture of polyurethane paint coating with MWCN in the following percentages by weight: 0, 1, 2, and 4%.

2.3 Preparation of the Samples

The oak samples were dried in drying tunnel (during the application of the first layer, the average humidity of the samples was 7.55%), and then cut to dimensions of 200 × 200 × 40 mm. Four portions of the polyurethane paint coating with the addition of MWCN 0%, 1%, 2%, 4%, respectively, were prepared. Before applying the first layer, the surface of the wood was sanded with 150 grit sandpaper. After applying the first layer with a 50 mm brush, the surface was waited for 24 h, and then the
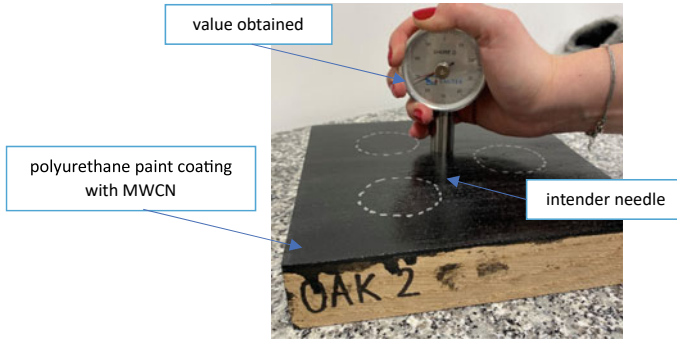
Fig. 3 View of the Shore D hardness test of a polyurethane paint coating with the addition of 2% of MWCN on oak sample

surface was sanded with 220 grit sandpaper, and another layer was applied (a total of 3 layers of mixture were applied). After application the surface was waited for 7 days (according to the producer's recommendations), and then testing was performed.

2.4 Testing Procedure

2.4.1 Hardness Tests

The hardness test was measured with the Shore D durometer (model: HBD 100-0 SAUTER, Switzerland), in accordance with ISO 868:2003. The measurement was made by inserting the intender needle at a distance of 9 mm from the edge and a minimum of 6 mm from each other by pressing the base of the hardness tester to the surface of the wood substrate (Fig. 3). After reaching stability, the hardness index showed the appropriate value in the range of 0 to 100.

2.4.2 Pull-Off Test

According to ASTM D4541, the pull-off strength test was used to determine the pull-off strength of the polyurethane coating on the wooden substrate. Initially, circle surfaces with radius of 50 mm and a depth of 5 mm were cut at three points to each sample. The next step was to clean and degrease the surface of the steel discs and wooden surface with acetone. Using an epoxy glue, the discs were glued to the designated places and left for 7 days for the glue to set. Then, the pull-off strength tests were started using an automated DY-216 machine (Proceq, Switzerland) (Fig. 4). The pull-off strength was automatically calculated by the device.
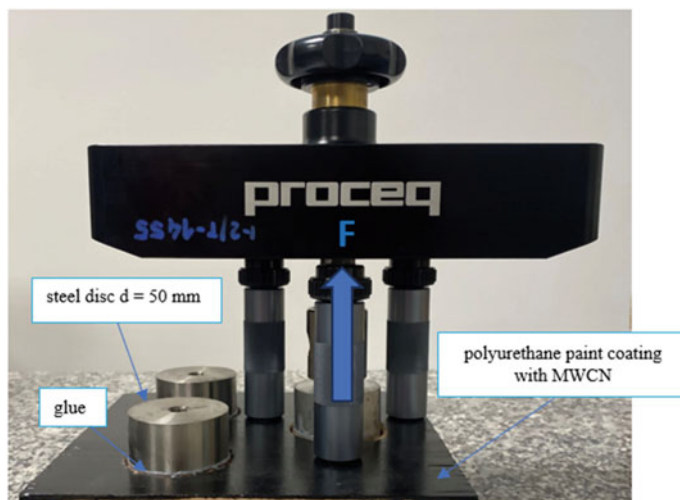
Fig. 4 View of pull-off test of a polyurethane paint coating with the addition of Multi Wall Carbon Nanotubes on oak sample

2.4.3 Cross-Cut Test

According to ISO 2409, a series of cuts were made with a suitable knife for wooden substrates (2 mm) over a 20 mm section, followed by a second series perpendicular to the first series. The knife was guided by a single decisive movement with constant pressure. This procedure was aimed at obtaining a grid of cuts. After the grid of cuts was made, the surface was gently cleaned with a soft brush to remove any loose flakes of coating. Next, a suitable standard tape of about 75 mm in length was selected and adhered to the center of the grid of cuts and gently pressed with a finger. Once the tape was properly adhered, it was peeled off in a smooth single motion in 0.5–1 s at a 60° angle (Fig. 5).

3 Results and Analysis

3.1 Shore D Hardness Test

Table 2 highlights Shore D hardness results for an polyurethane coating with addition of 0, 1, 2 and 4% by weight of MWCN on oak samples. In the case of oak sample without addition of MWCN, the average hardness was 70. The addition of 1, 2 and 4% of MWCN showed an increase in hardness compared to the sample without MWCN by 1,1 and 3 respectively. Standard deviation and coefficient of variation

STEP I
Performing the first series of cuts

STEP II
Performing the second series of cuts, perpendicular to the first series

STEP III
Cleaning the surface with a brush

AFTER 5 MINUTES

STEP IV
Pressing the tape to the center of the cut grid with a finger

STEP V
Peeling off the tape in a smooth motion at a 60-degree angle
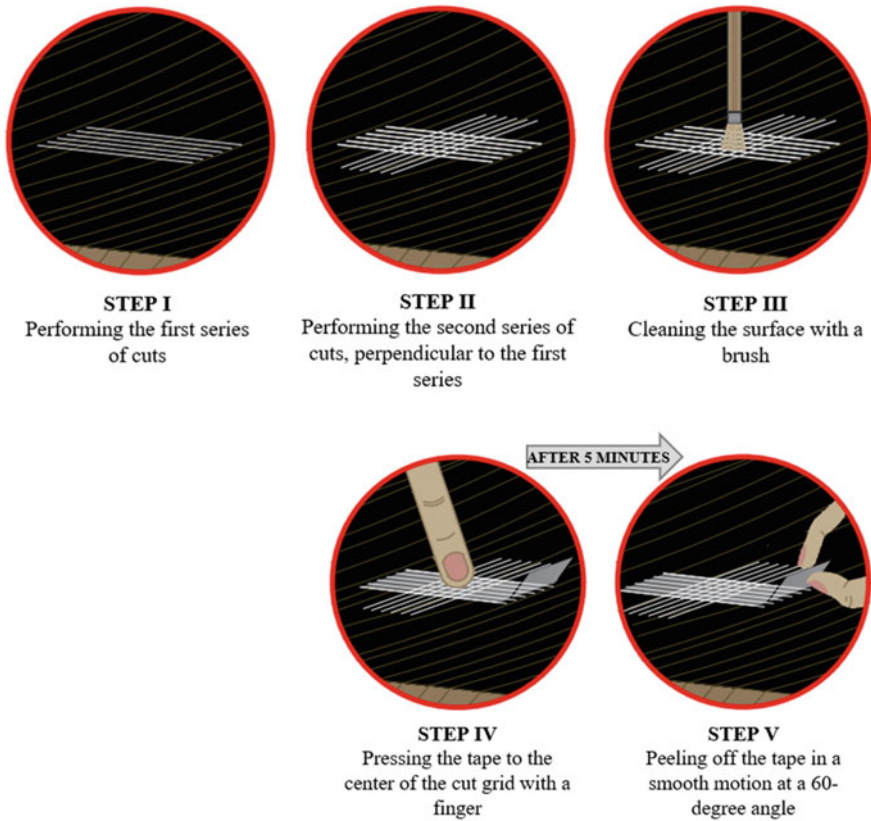
Fig. 5 Steps for cross-cut test

tend to decrease with each sample tested. The highest value was noticed for sample with 4% MWCN—73 MPa $\pm$ 2.69 MPa (CV 3.71%).

3.2 Pull-Off Strength Test

Table 3 highlights pull-off strength results for an polyurethane coating with addition of 0, 1, 2 and 4% by weight of MWCN on oak samples.

The average pull-off for oak samples without addition of MWCN was 3.70 MPa. The addition of 1, 2 and 4% of MWCN showed an increase compared to oak sample only covered with polyurethane paint coating. Comparing with other samples P-C1 showed the highest score 5.76 MPa $\pm$ 1.35 MPa (CV 24%). It was noted that for the samples, containing the MWCN additive, there were partial adhesion of the coating (adhesive failure), which was not observed for the polyurethane paint coating alone (cohesive failure) (Fig. 6).

Table 2 Summary of Shore D hardness results of the polyurethane coating with the addition of MWCN (0, 1, 2, and 4% by weight) on oak samples

Sample	The MWCN content (%)	Single results (MPa)	Average pull-off strength (MPa)	Standard deviation (MPa)	Coefficient of variation (%)
P-C0	0	74; 78; 65; 74; 70; 61	70	5.79	8.24
P-C1	1	74; 65; 68; 75; 71; 71	71	3.40	4.81
P-C2	2	69; 70; 73; 65; 74; 74	71	3.24	4.57
P-C4	4	72; 78; 72; 73; 70; 70	73	2.69	3.71

Table 3 Summary of pull-off strength of the polyurethane coating with the addition of MWCN (0, 1, 2, and 4% by weight) on oak samples

Sample	The MWCN content (%)	Single results (MPa)	Average pull-off strength (MPa)	Standard deviation (MPa)	Coefficient of variation (%)
P-C0	0	3.06; 4.07; 3.97	3.70	0.46	12
P-C1	1	4.53; 5.09; 7.64	5.76	1.35	24
P-C2	2	4.07; 4.53; 4.48	4.36	0.21	5
P-C4	4	5.22; 4.58; 5.19	5.00	0.29	6

3.3 Cross-Cut Test

Each of tested coatings with the addition of the appropriate content of MWCN was characterized by the fact that after the cross-cut test, no part of the coating detached, no cracks were visible and the edges of the cuts remained smooth. For this reason the adhesion of 0 was determined, which means that the edges are smooth and none of the coating square from the cut grid was detached (Fig. 7).

4 Conclusions

The study investigated the influence of Multi Wall Carbon Nanotubes (MWCN) on the mechanical properties of polyurethane paint coating for oak wood. The Shore D hardness, pull-off strength and cross-cut were tested. Based on the research, the following conclusions were drawn:

(1) In the case of Shore D hardness, the addition of 1, 2 and 4% MWCN caused a slight improvement in hardness by 1, 1, and 3 respectively.

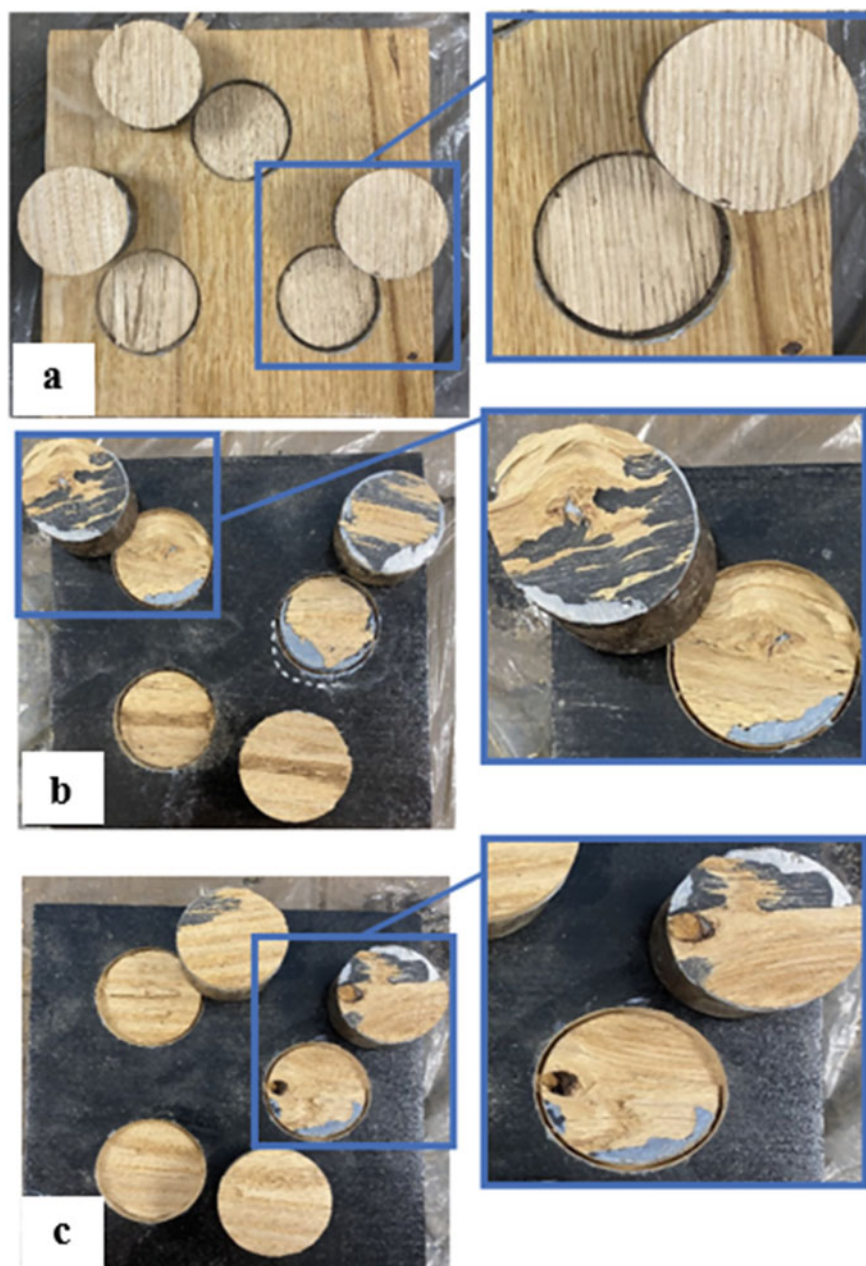**Fig. 6** An exemplary view of samples after the pull-off test: **a** for the polyurethane paint coating without MWCN, **b** for the polyurethane paint coating with 1% MWCN, **c** for polyurethane paint coating with 2% MWCN
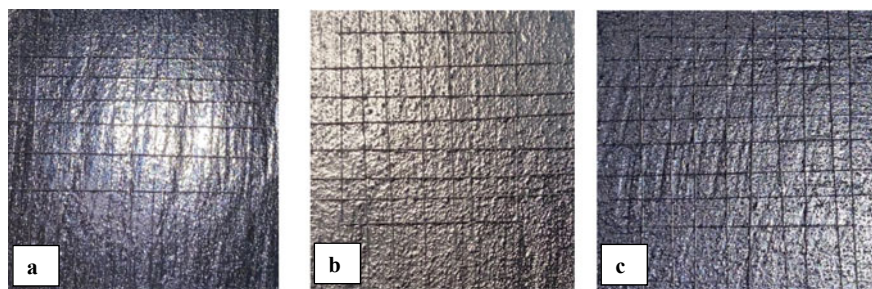
Fig. 7 A View of cut samples in the cross-cut test: **a** for polyurethane paint coating with 1% MWCN, **b** for polyurethane paint coating with 2% MWCN, c for polyurethane paint coating with 4% MWCN

(2) The pull-off strength test showed that for 1, 2 and 4% MWCN, a higher result was obtained. In addition, for samples with MWCN content, partial adhesion of the coating, which was not the case for the sample without MWCN.

(3) For the cross-cut test, no effect was noticed, classified as 0, which means that the edges of the cuts were smooth, and none of the coating square was peeled off.

(4) The addition of MWCN changes the appearance of oak wood, and with each layer of the paint coating the color of the coating becomes darker and darker.

Given the properties of Multi Wall Carbon Nanotubes affecting the coating, but also their high price, the use of the mixture may be profitable only on small surfaces, e.g. on stair treads. Therefore, the important properties to focus on in the next tests are abrasion resistance and surface roughness.

References

Abu, A.-R., Ashour, A., Tyson, B.: On the aspect ratio effect of multi-walled carbon nanotube reinforcements on the mechanical properties of cementitious nanocomposites. Constr. Build. Mater. **35**, 647–655 (2012)

Azarhoosh, A., Koohmishi, M., Vahedi, J.: Effect of carbon nanotubes on fatigue cracking of asphalt mixtures modified by styrene-ethylene/propylene-styrene. J. Adhes. **99**, 1832–1856 (2022)

Brzozowska, K., Chowaniec-Michalak, A.: Towards modification of polyurethane paint coatings for softwood protection: preliminary studies of the use of multi walled carbon nanotubes. Proc. Eng. Mech. 8–16 (2023)

David, M., Ion, R., Grigorescu, R., Iancu, L., Constantin, M., Stirbescu, R., Gheboianu, A.: Wood surface modification with hybrid materials based on multi-walled carbon nanotubes. Nanomaterials **12**(12), 1990 (2022)

Dehghan, M., Al-Mahaidi, R., Sbarski, I., Mohammadzadeh, E.: Surfactant-assisted dispersion of MWCNTs in epoxy resin used in CFRP strengthening systems. J. Adhes. **91**, 461–480 (2014)

Hu, Y., Luo, D., Li, P., Li, Q., Sun, G.: Fracture toughness enhancement of cement paste with multi-walled carbon nanotubes. Constr. Build. Mater. **70**, 332–338 (2014)

Kaymakci, A., Ayrilmis, N., Gulec, T., Tufan, M.: Preparation and characterization of high-performance wood polymer nanocomposites using multi-walled carbon nanotubes. J. Compos. Mater. **51**, 1187–1195 (2016)

Madhavi, T., Pavithra, P., Sushmita, B., Raj, S., Singh, S.: Effect of multiwalled carbon nanotubes on mechanical properties of concrete. Int. J. Sci. Res. **2**, 166–168 (2013)

Nochaiya, T., Chaipanich, A.: Behavior of multi-walled carbon nanotubes on the porosity and microstructure of cement-based materials. Appl. Surf. Sci. **257**, 1941–1945 (2011)

Papadopoulsa, A., Taghiyari, H.: Innovative wood surface treatments based on nanotechnology. Coatings **9**(12), 866 (2019)

Saeed, I.: Carbon naotubes—properties and applications: a review. Carbon Lett. **14**, 131–144 (2013)

Sandberg, D., Kutnar, A., Mantanis, G.: Wood Modification technologies—a review. iForest Biogeosci. For. **10**, 895–908 (2017)

Sobolev, K.: Nanotechnology and nanoengineering of construction materials. Nanotechnol. Constr. 3–13 (2015)

Staub de Melo, J., Trichês, G., Torres de Rosso, L.: Experimental evaluation of the influence of reinforcement with multi-walled carbon nanotubes (MWCNTs) on the properties and fatigue life of hot mix asphalt. Constr. Build. Mater. **162**, 369–382 (2018)

Zhu, Y., Li, Z., Feng, Y., Qi, W., Li, S., Wang, X., Chen, M.: Enhancement of wood coating properties by adding silica sol to UV-curable waterborne acrylics. Forests **14**(2), 335 (2023)

Zvekić, D., Srdić, V., Kamaran, M., Matavulj, M.: Antimicrobial properties of ZnO nanoparticles incorporated in polyurethane varnish. Process. Appl. Ceramics. **5**, 41–45 (2011)

The Effect of the Synergistic Application of Waste Granite Powder and Linen Fibers on the Adhesive Properties of Ecological Epoxy Coatings

Łukasz Kampa and Łukasz Sadowski

Abstract The coating was obtained by combining epoxy resin, granite powder (a waste material), and linen fibers (a renewable material). The first part of the paper describes all the ingredients and the method of preparing the concrete substrate. Afterwards, the way of modifying the coating is presented. The effect of two additives was analyzed: granite powder in amounts ranging from 0 to 50% (variable in 10% increments) in relation to the weight of the resin, and flax fibers in amounts ranging from 0 to 1.5% (varying in 0.5% increments) in relation to the weight of the resin. The reference sample was prepared without the addition of powders and fibers. The study focused on obtaining the highest possible pull-off strength. The greatest increase in strength was achieved with the addition of 1.5% of linen fibers and 30% of granite powder. In this case, the pull-off strength was equal to 3.09 MPa ($\sigma = 0.17$ MPa), which is 0.46 MPa (17.5%) better than the result obtained for the reference sample. Nine out of twenty-three modified coatings achieved a greater strength than the reference coating. The second part of the article presents a cost-economic analysis, and shows that the addition of granite powder significantly reduces the cost of the coating, and also that the fibers have a negligible effect on the total cost of the coating.

Keywords Epoxy resin · Granite powder · Natural fibers · Pull-off strength · Cost analysis

1 Introduction

The methods of modifying resin coatings, which are presented in Sect. 1.3, shows that such surfaces have great potential. In addition, the construction industry is increasingly focusing on reducing the environmental impact of building materials and entire buildings. The manufacturers of construction products try to produce them from

Ł. Kampa (✉) · Ł. Sadowski
Department of Materials Engineering and Construction Processes, Wroclaw University of Science and Technology, Wybrzeże Wyspiańskiego 27, 50-370 Wroclaw, Poland
e-mail: lukasz.kampa@pwr.edu.pl

waste and renewable materials that do not deteriorate quality parameters. Papers [1–3] describe the positive effect of granite powder on the technical and operational parameters of epoxy coatings. Moreover, this material is waste, a by-product of the manufacturing of granite products, and does not have many applications. It is used to a small extent as a ballast or, due to its chemical composition, as a fertilizer in agriculture. However, the scale of use of this raw material is much lower than its "production". Therefore, it is most often stored in heaps, and pollutes the surrounding natural environment by being dispersed by the wind.

Natural fibers are one of many ecological materials that are used in epoxy coatings. The effect of coconut fibers on epoxy resins is presented in paper [4]. Due to the fact that it is a renewable material, it can be successfully used on a large scale, and it does not deteriorate the quality of coatings (confirmed by the conducted tests).

When considering the above characteristics of waste and natural materials, it was decided to combine granite powder and linen fibers in epoxy resin. Such a procedure aims to obtain a coating that will have less of an impact on the environment, and which will in turn allow for a smaller consumption of the resin. Due to the problems related with the disposal of resins, this coating will also be easier to dispose of. A coating with an increased strength is expected to be obtained due to the implemented modifications.

2   Literature Survey

Floors are one of the most important parts of industrial facilities [5]. They should provide at least 25 years of trouble-free operation, with ongoing maintenance only required. It is estimated that their implementation may amount to as much as 20% of the costs related to an entire construction [5]. Therefore, it is necessary to take into account their proper execution, especially in terms of quality, because any damage leads to costly repairs of the surface and its decommissioning (downtime in the plant's production).

2.1   Floor Construction

The top (usable) layer of a floor is laid on a structural element, or is permanently connected to a bonding layer [6]. The definition of an industrial floor does not include residential surfaces, roads and streets. Industrial floors must have an adequate load-bearing capacity, durability, and evenness of the surface itself, and also be resistant to mechanical, chemical or thermal factors [5]. Due to the growing demand for warehouse and production space, the design of such floors is becoming more and more important. The construction of a typical industrial floor is schematically shown in Fig. 1.
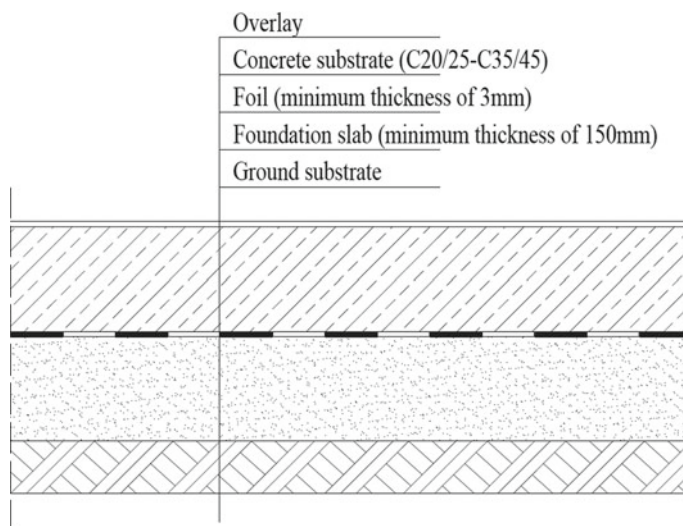
Overlay

Concrete substrate (C20/25-C35/45)

Foil (minimum thickness of 3mm)

Foundation slab (minimum thickness of 150mm)

Ground substrate

Fig. 1 Cross-section through a typical industrial floor applied on the ground

A typical industrial floor consists of several layers [6]. The main layers are the concrete substrate, foundation slab and ground substrate. The concrete substrate is a load-bearing layer, usually made of class C20/25–C35/45 concrete, and is exposed to loads and other destructive factors. In special cases, it is a reinforced concrete element or a prestressed concrete element. Fiber concrete, i.e. concrete reinforced with dispersed fiber, has been gaining popularity in recent years [7]. In this composite, the brittle cement matrix is reinforced using fiber. Strength is increased by reducing all kinds of matrix scratches and by the participation of fibers in load transfer. Cracks occur due to the exceeding of the tensile strength of concrete. When designing, it is necessary to keep in mind the causes of cracks, such as plastic shrinkage, drying shrinkage, excessive loading, or local stretching caused by e.g. the point pressure of a rack foot. Fibers can be made of various materials. Steel ones are used when concrete is exposed to impact, fatigue, abrasion or bending loads. In turn, glass and polypropylene fibers prevent the formation of scratches and shrinkage cracks. Various types of joints, such as anti-shrinkage, working or expansion joints, are important elements of the concrete substrate.

The next element of a floor is the slip layer. It should be made of foil with a thickness of at least 3 mm and a weight of at least 140 g/m^2 [5]. It is used to reduce the friction between the foundation slab and the concrete substrate, thanks to which it is possible to use larger distances between expansion joints and working joints. It also reduces the tensile forces in the slab, especially in the case of high forces caused by long-term loads. It prevents the substructure from mixing with the concrete mixture during its placement, as well as the loss of batch water from it. When exposed to the heat of cement hydration, it reduces the stress caused by the heating and cooling of the concrete. When using concrete with steel fibers, the performance of the slab

should be carefully analyzed. In this case, the friction may be substantially reduced, which will in turn cause large gaps (at expansion joints) between slabs, due to which some slabs will "work" significantly, while others will not do any "work".

The foundation slab is the leveling layer under the concrete substrate. It transfers loads from the concrete substrate to the ground [5]. At the same time, it also allows for the deformation of the concrete substrate, and provides homogeneous support for it. If the foundation slab is compacted uniformly, it also prevents keyboarding of individual slabs. A foundation slab should provide the required (design) bearing capacity and evenness, as well as durability and resistance. The thickness of this layer should be a minimum of 15 cm, and its final size depends on the frost zone (in the case of pavements outside building structures) and the provision of an adequate bearing capacity. Publications that describe the relationship between the size of the grains in the soil and the minimum thickness of the foundation slab can also be found [8]. This relationship is presented in Table 1.

Apart from thickness, the type of aggregate used is also important in the case of foundation slabs. Most often, the following are used: gravel-sand mixtures, crushed stone, wedge, soil stabilized with hydraulic binders, or a layer of non-structural concrete (base, low class). The final choice regarding the foundation slab belongs to the designer, who needs to take into consideration the loads that will act on the floor. The most important loads in this case are usually concentrated (point) loads: dynamic (e.g. from a moving forklift) and long-term (e.g. from a rack foot) loads. Deviations with regards to the level of the foundation slab should not be more than 2 cm over a 4 m section.

Ground substrate is understood as the layer of soil below the lower part of the foundation slab, which is affected by impacts from the concrete substrate [5]. The surface of this layer should be level (the permissible deviation is 3 cm over a 4 m section, unless the soil is subjected to hydraulic stabilization, then the deviation should not exceed 2 cm). Soil tests should be performed to the depth of the impact zone of the structure in load-bearing soils. However, it should not be less than 3 m, and in the case of organic, embankment and anthropogenic soils, not less than 2 m below the bottom of their load-bearing layers. The basic requirements for the soil include: uniformity of settlement, compatibility, bearing capacity, frost resistance, and low heave. This means that the soil should be homogeneous. In the case of soils with different parameters, uneven subsidence may occur in the place of their contact. In such situations, soil replacement or mechanical or chemical stabilization is used.

Table 1 Relationship between the thickness of the foundation and the grain size of the soil [8]

Soil grain size (mm)	Minimum thickness of the foundation slab (cm)
To 32	12
To 45	15
To 56	18
To 63	20

2.2 Top Floor Layer

Currently, there are many ways to finish the top layer of a floor. The choice of a specific solution belongs to the designer. It is selected based on the criteria that the floor must meet, such as: abrasion resistance, chemical resistance, water tightness, dust resistance, impact resistance, the ability to keep it clean, or anti-slip properties.

The execution of any floor should be preceded by a detailed assessment of the technical condition of the concrete substrate. The following must be checked [9]: compressive strength (a minimum of 25 MPa is required), pull-off strength (a minimum of 1.5 MPa is required), the presence of a cement laitance, humidity (not more than 4% in the surface layer), unevenness (the required inclination), and the cleanliness of the substrate (e.g. whether it is greasy). In addition, it is assumed that the temperature of the substrate should be within the range of 8–40 °C, and at the same time at least 3 °C above the dew point temperature. Relative air humidity should not exceed 75%.

When, as a result of the conducted tests, the pull-off strength is too low (<1.5 MPa), it is necessary to sand or mill the surface (which is contaminated with oily substances). In turn, grinding helps to level the surface. If there is an excess of cement laitance, shot blasting, sandblasting or milling is necessary. Shot blasting creates cavities in the material and makes it rougher [10]. This is due to the ejection of steel shot from the rotor. This treatment is dust-free, and thanks to it the required degree of opening of the surface pores is obtained. Sandblasting involves the shooting of a pen under high pressure (the diameter of the pen grains should be matched to the surface) [11]. As a result, the floor is cleaned, and different levels of roughness can be obtained. Milling is used to remove corroded fragments of the floor, or to remove the old one [12]. A milling device consists of rows of cutters with diamond teeth that are attached to a rotor. As a result of the rotational movement, the cutters hit the floor and cause it to crack and crumble. In the case of when the top floor layer is only dusty or muddy, sweeping and vacuuming is a sufficient treatment. As a result of these operations, it is worth priming the surface, which strengthens the near-surface layer by filling pores and reducing water absorption. This unifies the concrete surface.

In order to increase the strength of the floor, overlay made of dry sprinkles, impregnations, cement-based screeds (or cement-polyurethane screeds) or screeds are used. Concrete and cement overlays are the most popular (approx. 70% of surfaces), but resin floors are becoming more and more common (approx. 25%). To a lesser extent, ceramic, bitumen, anhydrite floors, etc. are used.

Top floor layers, depending on the used material, can have different thicknesses, and can therefore be divided into [5]: impregnations and varnish coatings, thin-layer coatings, and mineral and resin screeds.

When making concrete floors, the DST (Dry Shake Topping) system is most often used, in which surface hardening takes place with the use of special powders applied to the fresh floor. After spreading the product, the surface is smoothed with trowels. The powder is a mixture of cement, fine aggregate, silica fume pigment and other additives. The detailed composition is a trade secret of a given company [13].

These sprinkles work only in the near-surface layer (2–4 mm), but they significantly improve functional properties, such as hardness, abrasion resistance, and impact strength. Moreover, they prevent the absorption of oils or greases by the concrete. Such floors are also less dusty.

Another method of making mineral top floor layers involves DSP technology (Densfiled Systems containing homogenously arranged ultra-fine Particles). This method is also suitable for regenerating old floors [14]. With this technique, it is possible to obtain a compressive strength of several hundred megapascals, which is due to the high density of cement particles, and a low w/c ratio. As a result, these floors achieve the following strengths: 110–180 MPa for compression and 12–18 MPa for bending. They are also more resistant to abrasion and impact. Their water absorption varies, and is in the range of 2.0–3.5%. They are also characterized by high adhesion to the old floor (9 MPa), and a greater chemical and temperature resistance when compared to ordinary concrete.

Resin top floor layers are becoming more and more popular. There are several types of such floors, which differ with regards to the used binder: epoxy, polyurethane, acrylic, epoxy-polyurethane, and vinyl-ester [5]. They are made as coatings that are poured or puttied, and have a thickness of about 3 mm. They have many advantages, which include: their chemical resistance; their availability in many colors; and the fact that they do not age, are non-slip, are anti-electrostatic, and can be used inside and outside buildings [15]. Their disadvantages include the higher cost of their execution when compared to concrete floors, their low resistance to thermal shock, and their toxicity.

Epoxy surfaces are the most popular among all the resin top floor layers (50–60% of all epoxy surfaces). They are characterized by good technical parameters: tensile strength of up to 20 MPa; compressive strength of up to 90 MPa; bending strength of up to 40 MPa; their high resistance to abrasion, impact, acids and lubricants; and also their high hardness [5]. However, they are not flexible, and due to this a proper preparation of the substrate is required (it must have a high stiffness). They are also not resistant to UV rays, and depending on the manufacturer, they can be made of two or three components.

Polyurethane floors can be used in specific conditions. They have a high impact strength at low temperatures [16]. In addition, they are characterized by a high mechanical strength and a greater resistance to thermal shock when compared to epoxy floors—up to 90 °C when compared to approx. 65 °C in the case of epoxy coatings. They are also characterized by high stretchability, which reaches up to 160%. The substrate for these coatings must be dry, which is why the priming layer is often made of epoxy resins. One- or two-component solutions are available on the market.

Epoxy-polyurethane floors are a modification of the two previous solutions. They have high abrasion resistance and high flexibility [5]. Such floors can consist of several layers, and their total thickness can reach up to 25 mm. Varnish coatings are used as primer layers. Thin layers (0.5–1 mm) work well when there is not a lot of

traffic, and thick layers (1.5–5 mm) are resistant to high mechanical loads and aggressive environments. Putty layers (3–25 mm) are used in specialized conditions—heavy loads and very aggressive environments.

Polymethylmethacrylate coatings have similar properties to epoxy floors (high strength, high impact resistance, etc.), but they set in a short time (1–3 h) [5]. Acrylic surfaces also set quickly. An important advantage involves the possibility of applying them at even sub-zero temperatures. They are most often offered as ternary resins.

Ceramic floors are used in food-related facilities, commercial facilities, and when high mechanical strength and chemical resistance are required [5]. They consist of a layer of chemical insulation, stoneware, clinker or stoneware tiles, and a binder. The strength of such floors is determined by the type of tile and the jointing material. The correctness of the bonding is important with regards to these top floor layers—air voids under the tiles are unacceptable, because they significantly reduce the strength of such surfaces.

2.3 Modifications of Resin Floor Coatings

Due to an increasing use of resin coatings in industrial, warehouse, service and residential facilities, the modification of their properties is the subject of many scientific publications that aim to adapt the properties of such coatings to specific working environments. This can be achieved by appropriate modification of the substrate, or by changing the composition of the resin. The following sections of this paper present specific solutions regarding this matter.

Modification of the substrate may involve the providing of an appropriate structure of the substrate, or the changing of its composition. The goal of such actions is usually to obtain better strength parameters. Grinding the surface of concrete, which contains aggregate of more than 4 mm, allows the pull-off strength of resin to be increased [17], and it is therefore seen as the most effective method. When a smaller size of aggregate is used, it is possible to resign from grinding without strength being reduced. Sanding the concrete surface can be replaced by brushing the fresh concrete with a paintbrush [18]. This does not reduce the pull-off strength, but is a faster and more convenient solution. In turn, the use of texturing in the form of "+" signs on the surface of fresh concrete allows the strength of the floor to be increased. The optimal depth of such a texture is 12 mm. The subject of obtaining the appropriate roughness of the substrate by brushing is also presented in papers [19, 20].

The composition of the resin is also often modified. This is a more simple solution than the modification of the substrate layer. The improvement of properties is obtained by adding various types of materials, even waste materials. The addition of glass powder to the epoxy resin in an amount of 7.4–35.9% improves the pull-off strength of such a mixture [21]. The optimal solution is to use 19.4% of glass powder. Larger amounts of this additive result in an increase of the density of the resin, which in turn reduces the strength and makes the application more difficult. The improvement of the floor parameters was even possible without mechanical treatment of the substrate.

The conducted tests showed that the glass powder penetrated from the coating to the substrate, and filled the pores. This resulted in improved properties. Ultra-fine glass fiber also improves the mechanical properties (hardness, adhesion) and anti-corrosion properties of the resin [22].

Natural and artificial fibers are also popular for modifying resin coatings, and polypropylene fibers improve the pull-off strength of such coatings [23]. Horizontal adhesion on the cement grout substrate (with the addition of 1% of fibers) was equal to 3.3 MPa, while on the cement mortar substrate (with the addition of 0.5% fiber) it amounted to 3.93 MPa. This is a very high value. Moreover, ultrasonic testing did not show a significant densification of the samples' structures (with the addition of fibers) in their near-surface zone. In turn, the microstructural analysis showed very good coverage of the subsurface zone by resins made with additives. Polypropylene fibers, which are used as a filling material in epoxy composites, delay thermal decomposition and, when there is a sufficiently high content of them, increase the thermal stability of resin coatings [24]. Epoxy composites, in combination with synthetic fibers, or the mixture of synthetic fibers with carbon fibers, have improved mechanical properties, including their impact strength [25]. Coconut fibers also increase the pull-off strength of resin coatings [4], with the addition of 0.5–1.0% of such fibers being the best solution. It was noted that the addition of larger amounts of coconut fibers caused a significant decrease in the pull-off strength, even to a level below that obtained for the reference sample. Good filling of pores in the near-surface zone was confirmed by ultrasonic tests. Article [26] presents a comparison of coconut fibers and polypropylene fibers in terms of their mechanical properties and the cost of their manufacturing. A greater increase in strength of the resin was obtained when using synthetic fibers, with the costs of making these coatings being almost the same as the cost of executing the reference coating. This shows that the parameters of coatings can be improved at a low cost. In turn, carbon fibers are able to improve the cracking resistance and thermal parameters of the epoxy resin [27].

All kinds of rock powders, due to the properties of the original rocks, are also popular as materials that can be used for the modification and strengthening of resin coatings. Waste granite powder is the subject of many scientific works [1–3]. It increases the pull-off strength of concrete. The best material solution (10–20% of the powder in relation to the weight of the resin) obtained a strength of up to 3.4 MPa! In addition, a floor containing granite powder is more resistant to thermal shock (by more than 20 °C). Interestingly, the authors of the above mentioned publications also noticed that there is a relationship between pull-off strength and thermal shock resistance: the higher the strength, the greater the resistance. The conducted economic analysis showed that the addition of waste powder allows significant savings in the execution of such a floor to be obtained. Due to the negligible cost of a kilogram of powder in relation to the cost of resin, it can be assumed that the addition of each percent of granite powder reduces its cost by the same number, i.e. when adding 20% of the powder, the cost of producing the coating decreases by 20% when compared to the reference coating. In turn, quartz powders are perfect as a filler for resin coatings [28]. The pull-off strength of such coatings is increased and amounts to 3.3 MPa. The authors stated that this filler can be used in amounts of up to 29% of the coating's

weight. Raj et al. [29] conducted a comparison of carbon fiber reinforced composites based on three-phase epoxy resin and commercial epoxy resin. Mechanical properties, chemical resistance and thermal properties were checked. After the tests, better parameters were found in the case of three-phase epoxy resin. Kasemura et al. [30] conducted research on the modification of epoxy resin with silicone-containing block copolymers. As a result of such a combination, an improvement in hydrophobicity was obtained, but such coatings were characterized by a lower pull-off strength.

Wirries et al. [31] defined a novel in situ method to determine resin volumetric shrinkage. The method uses shrinkage measurements in a rotary rheometer, while observing the sample with a laser distance sensor.

The methods of modifying resin coatings presented in the above text present great potential in the possibilities that can be obtained thanks to appropriate modifications of the coatings. Moreover, in the construction industry, more and more attention is focused on the lower impact of building materials and entire building structures on the natural environment. Manufacturers of construction products try to produce them from waste materials that are renewable and at the same time do not deteriorate the quality parameters. The positive impact of the addition of granite powder on the technical and functional parameters of epoxy coatings is presented in the above works. Additionally, this material is a waste, a by-product of the production of granite products. It doesn't have much use. It is used to a small extent as ballast or, due to its chemical composition, as a fertilizer in agriculture. However, the scale of use of this raw material is much lower than its "production", which is why it is most often stored in piles, thus polluting the surrounding natural environment by being blown away by the wind.

The ecological material used in epoxy coatings is among others fibers of natural origin. The influence of coconut fibers on epoxy resin is presented in the above works. Due to the fact that it is a renewable material, it can be successfully used on a large scale, and as research has confirmed, it does not deteriorate the quality of coatings.

Taking into account the above characteristics of waste and natural materials, in the design part of this work it was decided to combine granite powder and flax fibers in epoxy resin. The resulting coating will have less impact on the environment and will allow for less resin consumption. Due to the problems with resin disposal, this coating will also be easier to dispose of. The expected effects of such a mixture are primarily an increase in strength. Moreover, in order to determine the best quality parameters, it was decided to use artificial intelligence.

3 Materials and Methods

3.1 Preparation of the Concrete Substrate

The research began with the preparation of the concrete substrate. It was decided to use C25/30 class concrete, which is the minimum class of concrete that is required by epoxy resin manufacturers [32]. The substrate was made using a dry concrete mix that is available on the market. The technical data sheet of this mix shows that the size of the aggregate is up to 4 mm, and the recommended layer thickness should be from 20 to 150 mm (80 mm was used). The exact recipe of the mix is a secret of the producer.

The concrete slab was made on a 120 × 80 cm pallet. The dimensions result from the fact that 24 test fields (dimensions 20 × 20 cm) were meant to be obtained. Such a test field size is the minimum area required in order to perform four pull-off strength tests for each of the coatings. Details of this are explained in Sect. 4.6. The sides of the mold were made of boards, which enabled the required slab thickness (8 cm) to be obtained. Then, the inside of the mold was lined with construction foil in order to facilitate the demolding of the element and to prevent a loss of mixing water (Fig. 2b). All the necessary mix ingredients (200 kg) was prepared in a concrete mixer (Fig. 2a, i, c). The mix was combined with the necessary amount of water (2.5 l/25 kg of the dry mix) and thoroughly mixed for about 5–6 min. The finished mix was placed in the mold, compacted with an internal vibrator, with its surface then being leveled (Fig. 2d). Three cubic samples measuring 10 × 10 × 10 cm were also made to determine the class of the obtained concrete. The slab was covered with foil to avoid evaporation of any water, and then cured for 28 days in standard conditions [33].

3.2 Waste Granite Powder

The used granite powder came from a Polish mine—Strzeblowskie Kopalnie Surowców Mineralnych Sp. z o. o., and has the trade symbol MS063D-01. Its chemical composition, which is provided by the manufacturer, is presented in Table 2 [34]. The granulation of the powder is 63 μm (admissible residue on the control sieve is 7%), and its grain distribution is shown in Fig. 3a. Figure 3b shows a photo of the used powder.

3.3 Linen Fibers

The used fibers came from tow linen, which results from the processing of linen stalks. They are manufactured by Unipak under the trade name Unigarn, and are
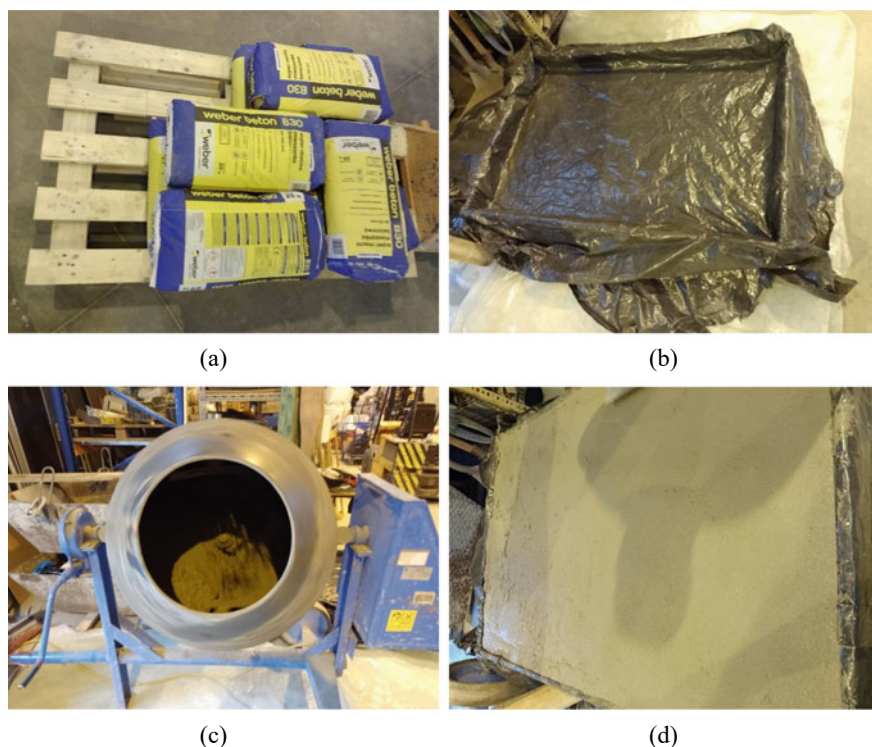
Fig. 2 Preparation of the concrete substrate: **a** bags with the dry concrete mix, **b** prepared mold, **c** mixing of the concrete mix, **d** leveling of the surface of the concrete substrate

Table 2 Basic technical parameters of the used granite powder (based on data provided by the manufacturer [34])

Chemical parameters	Value [%]
SiO_2	74.00–78.00
Al_2O_3	12.50–14.00
Fe_2O_3	0.20–0.40
TiO_2	Max. 0.05
$K_2O + Na_2O$	7.50–8.50
MgO	Max. 0.50
CaO	Max. 0.50
Losses during the test	Max. 1.00

mainly used to seal threaded connections. They are a non-absorbent material that can operate at temperatures up to 130 °C, have no perceptible odor, and their density is 1.5 g/cm^3 [35]. The commercial product is shown in Fig. 4a, and the chopped fibers used for the tests can be seen in Fig. 4b. Their length was about 10–12 mm.
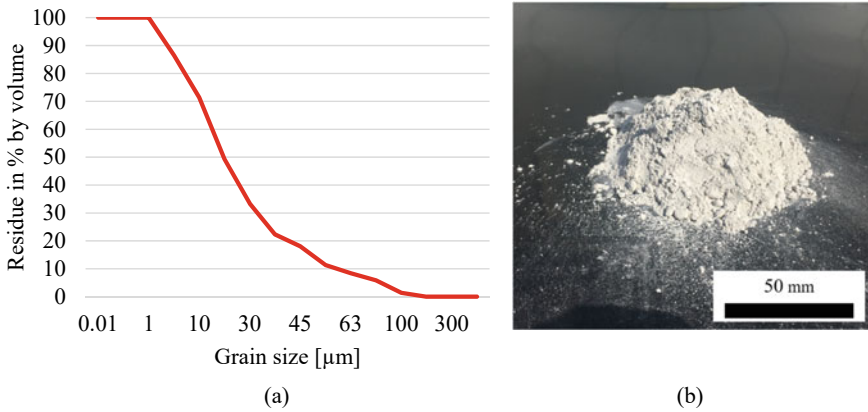
(a)   (b)

Fig. 3 Properties of the used granite powder: **a** particle size distribution (based on data provided by the manufacturer [34]), **b** photo of the powder

(a)   (b)

Fig. 4 Test fibers: **a** tow linen, **b** prepared, chopped test fibers

3.4 Epoxy Resin

The epoxy resin used in the tests was Meteor Primer resin (Si-Tech Sp. Z o. o., Dobra 9, 05–306 Jakubów), which is usually applied in primer layers. In the tests, it was modified, but no other surface layers were used. The resin had the following parameters: a density of 1.0–1.2 g/cm3, a viscosity of 400–600 MPa*s, a pot life (at 20 °C) of 20–30 min, and full hardening after 24 h. The resin is the result of the reaction of bisphenol A with epichlorohydrin (epoxy resin—average molecular weight ≤ 700). Its basic parameters are: reaction to fire—Bfl-s1, release of corrosive substances—SR, abrasion resistance ≤ AR1, impact resistance ≥ IR4, and pull-off adhesion ≥ B1.5 (manufacturer's data [32]). The ratio of component A to B was 100:45.

3.5 Preparation of the Epoxy Coating

The previously prepared concrete substrate was ground using an angle grinder with a diamond disc for grinding concrete surfaces (Fig. 5a). This process was done with water so as not to pollute the environment. This treatment allowed the cement laitance to be removed from the surface. After grinding, the surface was washed with water using a pressure washer, which resulted in a clean surface of the slab being obtained (Fig. 5b and a close-up in Fig. 5c).

After a few days, which were necessary for the slab to dry in natural conditions, the surface was degreased with acetone. Individual test fields were then separated (Fig. 5d) using a bitumen roofing sealant (non-reactive with epoxy resin). Each field was 20 × 20 cm. The slab had a total size of 120 × 80 cm, which allowed 24 research fields to be obtained.

The used epoxy resin consisted of two components: A and B (ratio 100:45). It was modified with granite powder in the amount of 0, 10, 20, 30, 40, 50 and 60% of the total weight of the resin, and with linen fibers in the amount of 0, 0.5, 1.0 and

(a)   (b)
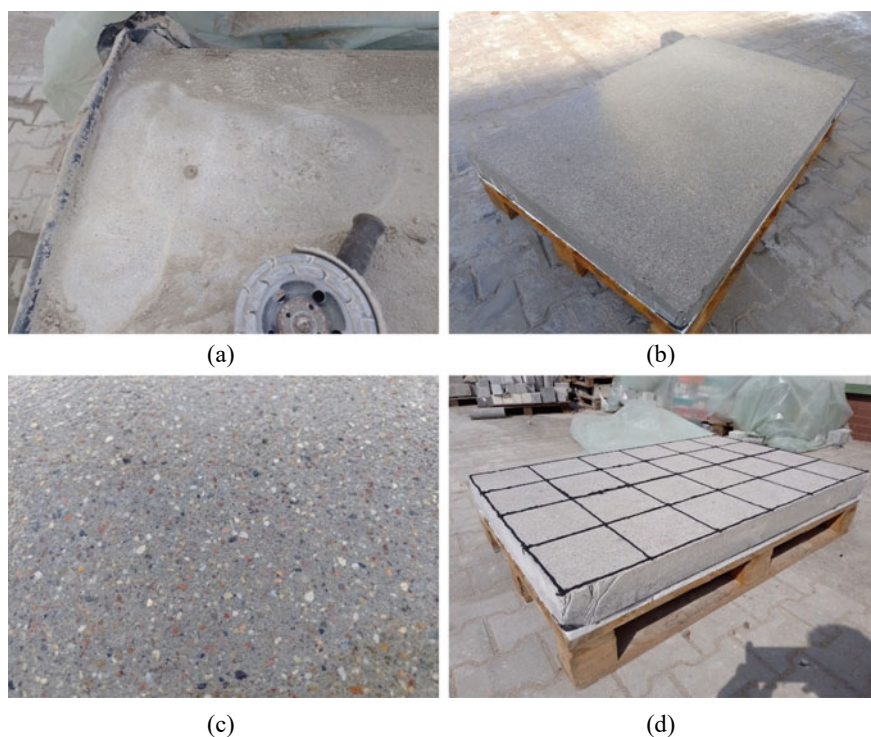
(c)   (d)

Fig. 5 Preparation of the slab for the resin coating: **a** the surface during grinding, **b** the surface washed using a pressure washer, **c** close-up of the washed surface, **d** separate test fields on the surface of the concrete slab

1.5% of the total weight of the resin. The arrangement of the test fields on the slab is shown in Fig. 6. Coating preparation stages: (a) arrangement of test fields on the slab, (b) component A, (c) adding the appropriate amount of linen fibers, (d) adding a measured amount of granite powder to the already mixed components, (e) adding component B.

a. The sample containing 0% powder and 0% fibers was made as the reference sample. The individual stages of preparing the coating were as follows. First, the appropriate amount of component A was measured (Fig. 6b), a measured amount of granite powder was added (Fig. 6c), and the ingredients were then mixed. Fibers
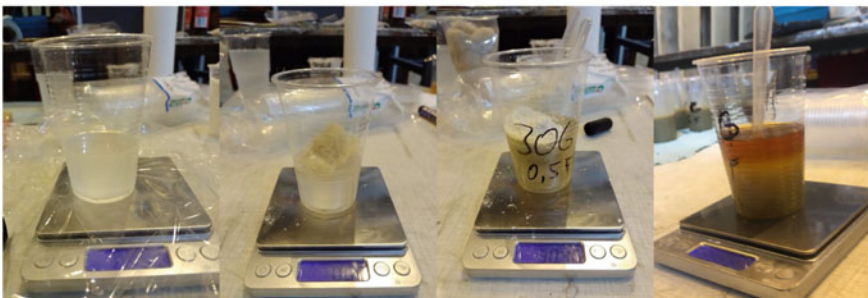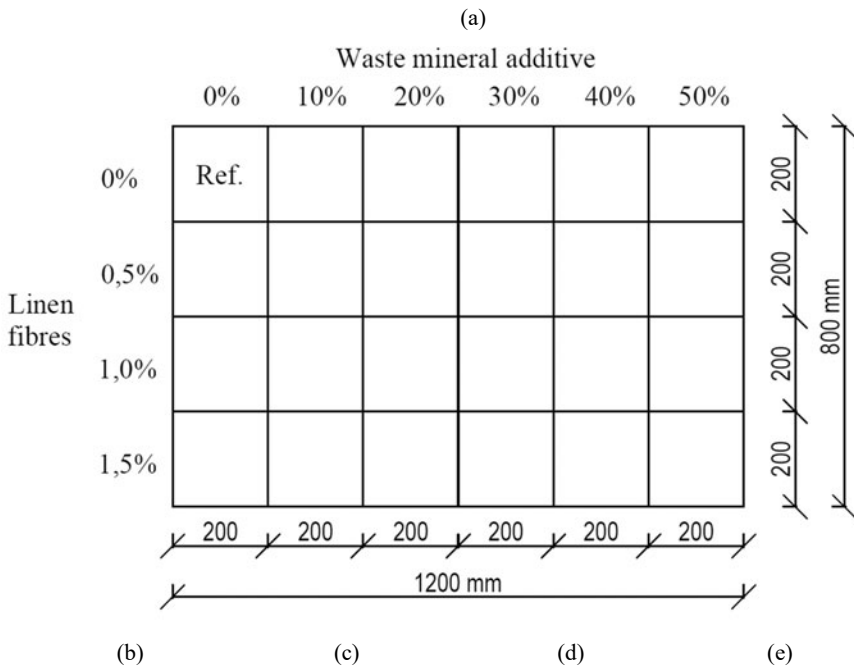

Fig. 6 Coating preparation stages: **a** arrangement of test fields on the slab, **b** component A, **c** adding the appropriate amount of linen fibers, **d** adding a measured amount of granite powder to the already mixed components, **e** adding component B

were added to the mixlater (Fig. 6. Coating preparation stages: (a) arrangement of test fields on the slab, (b) component A, (c) adding the appropriate amount of linen fibers, (d) adding a measured amount of granite powder to the already mixed components, (e) adding component B.

(d), but they caused difficulty in mixing due to the fact that they were very dry. This resulted in the thickening of the mix, especially due to the fact that there was a large amount of powder and fibers. After mixing the three components, there was a one hour break. Component B was then added (Fig. 6e) and everything was thoroughly mixed again. The resins prepared in this way were placed on the appropriate test fields, with a coating thickness of about 3 mm being obtained. The coating was compacted and deaerated with a hard bristle brush, but due to a large amount of fibers and powder, there were difficulties with the even distribution of fibers over the entire surface of the sample.

3.6 Pull-Off Strength Test

About two weeks after the application of the coating, preparations for the pull-off strength test were started. The surface of the resin was sanded with fine sandpaper in order to level any unevenness, as well as to increase the adhesion of the bonding agent to the coating. Then, four boreholes with a diameter of 50 mm were made on each of the coatings to a depth of about 5 mm. A diagram of their distribution on the test field is shown in Fig. 7a, with the cross-section through the slab being shown in Fig. 7b. A diamond drill was used for this purpose. In the initial phase of the drilling, a drill stabilization device was also used. The operation was interrupted to cool down the foraminifera, and to not increase the temperature of the coating. After making all the holes, the resin surface was thoroughly cleaned, dusted, and degreased with acetone. The surface of the steel discs was also degreased. The bonding between the steel disc and the coating was made using Epidian 5 epoxy resin with Z1 hardener from Ciech Sarzyna (Nowa Sarzyna), which was applied to both surfaces. The ratio of ingredients was 100:12. Afterwards, the disc was pressed against the surface of the coating, and excess glue was removed. A constant pressure was ensured in the initial phase of the binding.

After the adhesive layer had cured (after about a week), the pull-off strength test was started. The first stage involved the screwing of a screw connector into a steel disc using a round head, which in turn ensured an articulated connection of the disc with the jaw of the device (Fig. 7d). After positioning and leveling the device, the pull-off strength test was started (Fig. 7c). It took 100 s, and the load was increased at a rate of 0.05 MPa/s. The device used in the study was the Proceq Dy-216, which enables results to be recorded, and a graph of load increase over time to be created. The entire procedure was performed in accordance with ASTM D4541 [36], which states that e.g. at least 3 tests for a given coating need to be performed (4 were performed due to the need to acquire more data; a diagram of the location of the pull-off strength tests is shown in Fig. 7a), and that an appropriate distance between
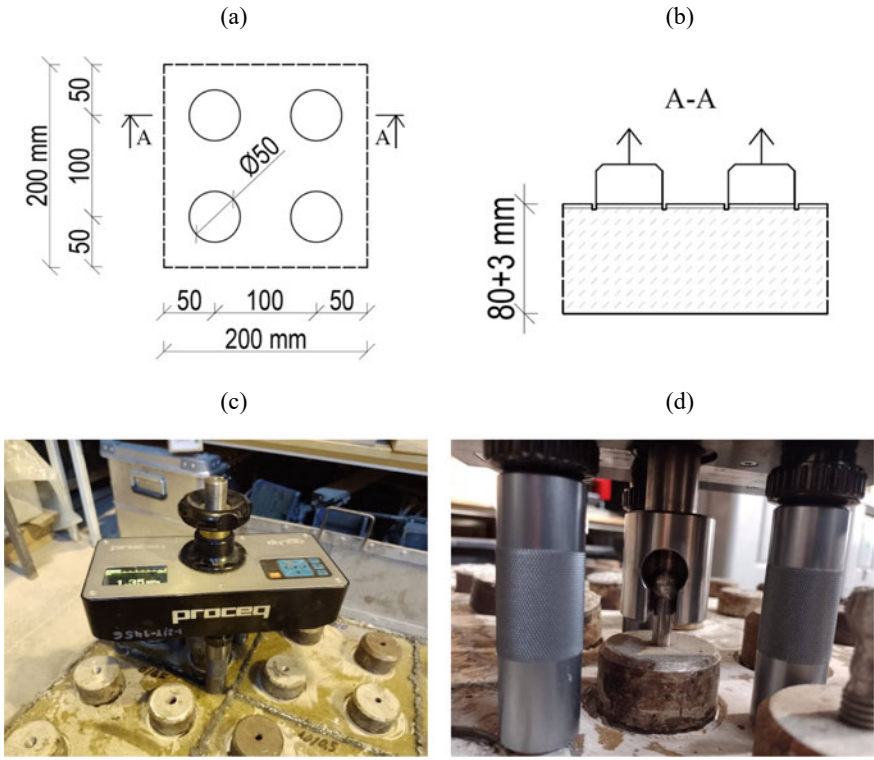
Fig. 7 The pull-off strength test: **a** diagram of the location of the pull-off strength tests on the test field, **b** the cross-section through the sample during the tests, **c** the testing device, **d** the connection between the steel disc and the device for measuring the pull-off strength using a connector with a round head

the test fields (equal to a minimum of five times the thickness of the coating (Fig. 7a, b)) needs to be maintained. In this study, a distance of 15 mm was kept.

4 Results

4.1 Determination of the Class of Concrete

According to the declaration of the manufacturer of the concrete mix that was used to make the concrete substrate, it was supposed to be of C25/30 class. This was verified by making four $10 \times 10 \times 10$ cm cubes in order to perform the destructive tests with the use of a hydraulic press. The tests were performed to check their compressive strength, and were carried out after 28 days in accordance with standard [37].
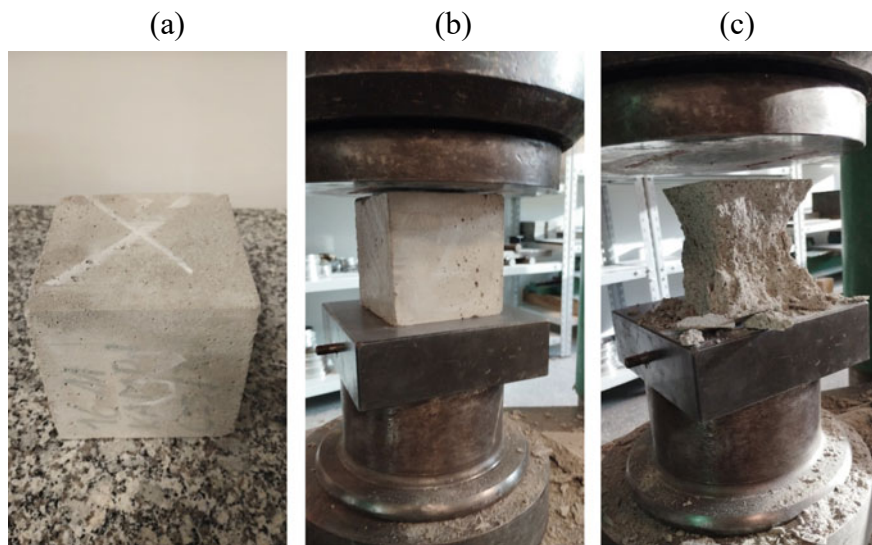
Fig. 8 The concrete strength test: **a** sample prepared for testing, **b** sample placed in a hydraulic press, **c** damaged sample after testing

In Fig. 8a, one of four samples is shown. First, the basic dimensions of each sample were measured, with the obtained results being presented in Table 3. Three measurements were taken at the bottom and at the top of the sample in two directions (A and B). The height was measured on each side. In addition, the sample was weighed in order to determine its density. Figure 8b shows a sample placed in a hydraulic press, and Fig. 8c shows the already damaged sample. The sample obtained a classic shape of an hourglass after destruction.

Compressive strength was calculated based on the following formula:

$$f_{ci} = \frac{P}{A_{mean}}$$

f_{ci}—Compressive strength,

P—The force that destroys a concrete sample,

A_{mean}—Compression surface.

However, the strength results were obtained for samples with the dimensions of $10 \times 10 \times 10$ cm. In order for the achieved strength results to correspond to those required by the standard (a cube sample with a side length of 15 cm), these values should be multiplied by 0.9. Therefore, strengths equal to: 21.02, 21.06, 21.56 and 21.40 MPa were obtained. Compliance of the obtained value of the compressive strength of concrete with that from the standard concerning concrete is considered to be confirmed if both of the following criteria are met simultaneously (Table 4).

As a result of the conducted calculations, the following was obtained:

Table 3 Summary of measurement results for the cubic samples (explanation of symbols can be found in the above text)

No	Sample designation	Top		Bottom		H	Weight	Destructive force	Compressive strength	Density
		A	B	A	B					
		[mm]				[mm]	[g]	[kN]	[MPa]	[kg/m³]
1	1	100.88	99.83	101	99.71	99.82	2070.96	235	23.36	2060.2
		100.85	99.89	100.58	99.72	100				
		101.14	100.19	99.85	100	100.09				
		Average cross-sectional area		Average cross-sectional area		99.76				
		100.96	99.97	100.48	99.81					
		10,092.64		10,028.58						
		10,060.61								
2	2	101	99.79	99.95	99.93	99.74	2059.35	234	23.40	2064.2
		100.8	99.72	99.15	99.88	99.86				
		99.7	100.28	99.82	100	99.72				
		Average cross-sectional area		Average cross-sectional area		99.73				
		100.5	99.93	99.64	99.9367					
		10,042.97		9957.69						
		10,000.33								

(continued)

Table 3 (continued)

3									
3	99.82	100	99.91	100.31	99.88	2064.73	238	23.95	2074.8
	99.3	99.92	98.62	99.96	99.97				
	99.7	99.84	98.9	99.87	100.34				
	Average cross-sectional area				100.43				
	99.607	99.92	99.143	100.047					
	9952.70		9918.96						
	9935.83								
4	101	99.97	99.84	99.86	100.12	2071.2	238	23.78	2069.0
	100.57	100.25	99.55	99.84	100.17				
	99.75	99.95	100	99.9	99.92				
	Average cross-sectional area				99.9				
	100.44	100.06	99.797	99.8667					
	10,049.69		9966.36						
	10,008.03								

Table 4 Compliance conditions for the compressive strength of concrete

Concrete production	Number of samples n	Criterion 1—average value from n samples f_{cm}	Criterion 2—single score f_{ci}
Initial	3	$\geq f_{ck} + 4$	$\geq f_{ck} - 4$
Continuous	15	$\geq f_{ck} + 1.48 s_R$	$\geq f_{ck} - 4$

$\overline{R} = f_{cm} = 21.26\,\text{MPa}$—average compressive strength of concrete

$R_{i,\min} = 21.02\,\text{MPa}$—the smallest obtained strength value

Therefore:

$f_{cm} = 21.26\,\text{MPa} > f_{ck} + 4 = 34\,\text{MPa}$ condition not fulfilled

$f_{ci} = 21.02\,\text{MPa} > f_{ck} - 4 = 26\,\text{MPa}$ condition not fulfilled

The conditions were not met, which ultimately means that the class of concrete was lower than that declared by the manufacturer.

4.2 Pull-Off Strength Results

All the connections between the steel discs and the coatinghad a rupture in the concrete substrate (cohesive type). This means that all the modified layers adequately strengthened the near-surface layer. It is worth noting that even in the case of a large amount of fibers and powder, there was no cohesive failure. This was despite the high density of the resin and the problems with its even distribution. The resin then still had sufficient fluidity to fill the near-surface pores in the concrete.

Figure 9 shows the dependence between the pull-off strength of the epoxy resin coating and the substrate with regards to the amount of added granite powder and linen fibers. The strength of the reference sample was 2.63 MPa. Nine out of the 23 modified samples obtained a higher value. The largest of them was 3.09 MPa ($\sigma = 0.17$ MPa), which is 0.46 MPa (17.5%) better than the reference sample. This value was obtained with the addition of 1.5% of linen fibers and 30% of granite powder. Interestingly, a very similar result (3.02 MPa ($\sigma = 0.29$ MPa), which is 0.39 MPa (14.8%) more than the reference sample) was obtained for the sample containing no fibers and only 20% of the powder. The sample with the addition of 30% of the powder (no fibers), and the sample containing 1.5% fibers and 40% of the powder obtained very similar results—2.91 MPa ($\sigma = 0.29$ MPa) and 2.93 MPa ($\sigma = 0.10$ MPa), respectively. A result of about 2.80 MPa was obtained for the sample containing 40% of the powder, and also for the sample with 1% of the fibers and 50% of the powder. The addition of 0.5% of the fibers and 50% of the powder increased the strength by 0.11 MPa. The addition of 1% of the fibers and 30% of the powder also increased the strength slightly (by 0.01 MPa). The remaining samples did not have an increase in strength. These results show that the addition of granite powder
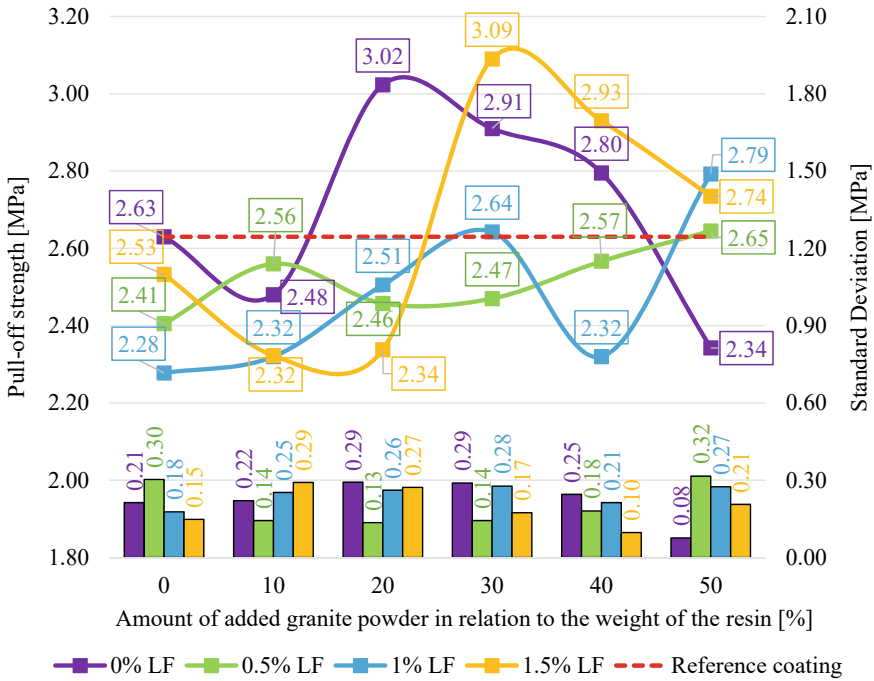
Fig. 9 Dependence between the pull-off strength of the epoxy resin coating and the substrate with regards to the amount of added granite powder and linen fibers

from 20 to 40% increases the strength of the resin itself, while at the same time maintaining its appropriate viscosity for filling the near-surface pores. Importantly, all the coatings obtained values greater than 1.5 MPa, i.e. the value declared by the resin's manufacturer.

The presence of fibers in the resin had no direct effect on strength. This is confirmed by the first part of the graph (in Fig. 10), which correlates with the lack of powder being added. All values were lower than the reference sample (even by 0.49 MPa). A similar graph was obtained for the sample with 10% of the powder. Moreover, in this case, all the samples obtained a lower value of pull-off strength than the reference sample.

5   Cost-Economic Analysis

In today's difficult times, everyone is looking to save money. It is no different in the construction industry, where building materials of lower price, but often of lower quality, appear more and more often. However, in some cases, the use of cheaper
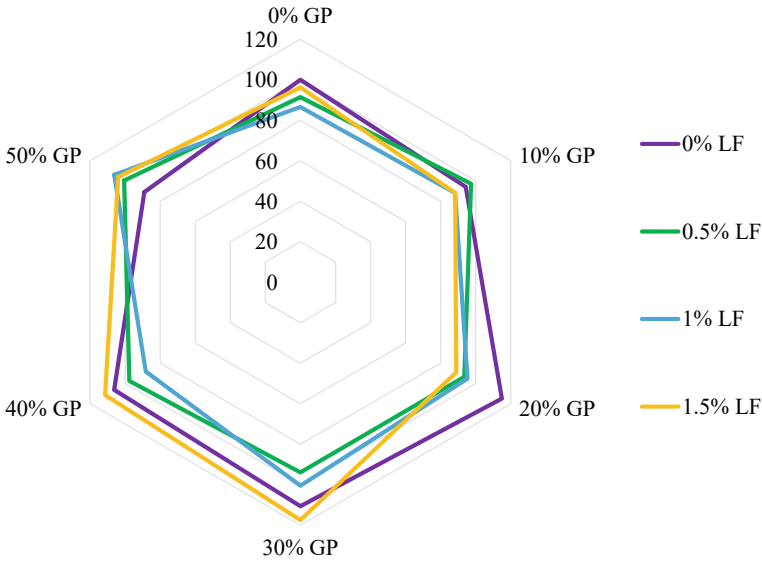
Fig. 10 Mechanical Performance Ratio (MPR) with regards to the amount of granite powder and linen fibers

substitutes or fillers does not necessarily mean that the material parameters deteriorate. The granite powder and linen fibers used in this study are a good example of this. They are cheap raw materials, and at the same time, as presented in the above points, they even allow pull-off strength to be increased.

A cost-economic analysis was carried out to understand the costs of producing such coatings. However, only the costs related to the purchase of the epoxy resin, granite powder and linen fibers were presented. The cost of the coating was not included due to its constant value, which is independent of the composition of the mix. The price of the components was assumed to be as follows: resin -12€/kg, granite powder—0.04€/kg, and linen fiber—10€/kg.

A list of the costs of individual types of coatings is presented in Table 5. In order to compare the production costs with the mechanical properties, the compressive strengths of the coatings are also given. Significant cost savings can be seen when adding larger amounts of granite powder. However, in the case of adding only fibers, the costs increase slightly, but when adding just powder, the total costs are lower than that of the reference coating. The cost of the highest-strength coating is 2.15€/m^2, which is as much as 0.85€/m^2 lower than for the reference coating (3.00€/m^2). In turn, the cheapest coating costs 1.55 €/m^2, which is almost half the value of the reference coating, and its strength is 2.34 MPa. This shows how to easily reduce the cost of coatings, while at the same time increasing their strength.

Table 5 Summary of the costs of the tested coating with regards to the amount of added granite powder and linen fibers

No	Epoxy resin [%]	GP [%]	LF [%]	Epoxy resin cost [€/m²]	GP cost [€/m²]	LF cost [€/m²]	Total cost [€/m²]	Pull-off strength [MPa]
1	100	0	0	3.00	0	0	3.00	2.63
2	90	10	0	2.70	0.01	0	2.71	2.48
3	80	20	0	2.40	0.02	0	2.42	3.02
4	70	30	0	2.10	0.03	0	2.13	2.91
5	60	40	0	1.80	0.04	0	1.84	2.80
6	50	50	0	1.50	0.05	0	1.55	2.34
7	99.5	0	0.5	2.99	0	0.02	3.01	2.41
8	89.5	10	0.5	2.69	0.01	0.02	2.72	2.56
9	79.5	20	0.5	2.39	0.02	0.02	2.43	2.46
10	69.5	30	0.5	2.09	0.03	0.02	2.14	2.47
11	59.5	40	0.5	1.79	0.04	0.02	1.85	2.57
12	49.5	50	0.5	1.49	0.05	0.02	1.56	2.65
13	99.0	0	1.0	2.97	0	0.04	3.01	2.28
14	89.0	10	1.0	2.67	0.01	0.04	2.72	2.32
15	79.0	20	1.0	2.37	0.02	0.04	2.43	2.51
16	69.0	30	1.0	2.07	0.03	0.04	2.14	2.64
17	59.0	40	1.0	1.77	0.04	0.04	1.85	2.32
18	49.0	50	1.0	1.47	0.05	0.04	1.56	2.79
19	98.5	0	1.5	2.96	0	0.07	3.02	2.53
20	88.5	10	1.5	2.66	0.01	0.07	2.73	2.32
21	78.5	20	1.5	2.36	0.02	0.07	2.44	2.34
22	68.5	30	1.5	2.06	0.03	0.07	2.15	3.09
23	58.5	40	1.5	1.76	0.04	0.07	1.86	2.93
24	48.5	50	1.5	1.46	0.05	0.07	1.57	2.74

5.1 Mechanical and Cost Analysis of the Tested Coatings

In order to compare the mechanical parameters (pull-off strength) of the coatings, the Mechanical Performance Ratio (MPR) was used:

$$MPR = \frac{F_{mizes}}{F_{Ref.}} \times 100\% [\%]$$

MPR—Mechanical Performance Ratio,

F_{mizes}—Pull-off strength of a given sample,

$F_{Ref.}$—Pull-off strength of the reference sample.

In order to compare the obtained results, the Mechanical Performance Ratio (MPR) was calculated using ΔMPR:

$$\Delta MPR = \frac{MPR_{series}}{MPR_{Ref.}}[-]$$

MPR_{series}—Mechanical Performance Ratio of a given sample,

MPR_{Ref}—Mechanical Performance Ratio of the reference sample.

Figure 10 shows the MPR graph with regards to the amount of added granite powder and linen fibers. It can be seen that the highest strengths were obtained with no addition of fibers, and with the addition of 1.5% of fibers. At the same time, most results were concentrated within the 90–100% MPR range. It is worth noting that strengths close to that of the reference coating can be obtained with the addition of 50% of the powder. This is good information due to the very limited costs of such a coating.

The cost of producing epoxy resin coatings mainly depends on the costs related to their ingredients and their location. In order to determine the individual costs of materials in relation to their importance for the composition of the mix, the Effective Cost Ratio (ECR) was calculated:

$$ECR = \frac{C_{mixes}}{C_{Ref}} \times 100\%[\%]$$

ECR—Effective Cost Ratio,

C_{mixes}—The cost of making a given sample,

C_{Ref}—Cost of making a reference sample.

$$\Delta ECR = \frac{ECR_{mixes}}{ECR_{Ref}}[-]$$

ECR_{mixes}—Effective Cost Ratio a given sample

ECR_{Ref}—Effective Cost Ratio a reference sample.

Figure 11 shows the Effective Cost Ratio (ECR) with regards to the amount of added granite powder and linen fibers. It can be seen that all the lines coincide. This means that linen fibers are of little importance for the cost of the coating. The cost of granite powder is of primary importance. In general, it can be assumed that the addition of every 10% of the powder reduces the cost of the coating by about 10%, which further confirms the usefulness of using granite powder in resins.

Table 6 shows a summary of the Mechanical Performance Ratio (MPR) and Effective Cost Ratio (ECR) for all the tested coatings.
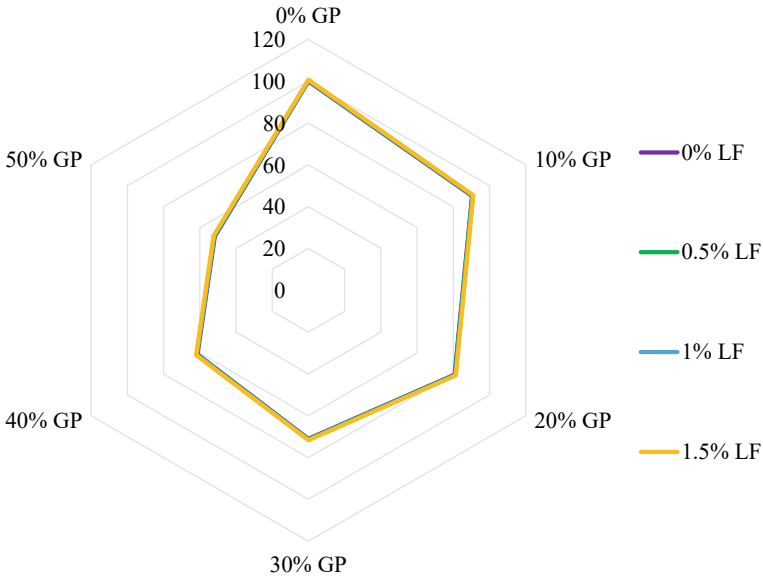
Fig. 11 Effective Cost Ratio (ECR) with regards to the amount of granite powder and linen fibers

Figure 12 shows the graph of MPR and ECR with regards to the amount of granite powder and linen fibers. This simple diagram allows the right solution to be easily chosen, depending on what is needed—the greatest cost reduction or the greatest increase in durability.

The results are shown in colors that refer to the addition of powder, and shapes that refer to the addition of fibers. Most of the results (10) were classified to the group of lower cost and lower strength. Importantly, from the point of view of this study, 5 results were classified to the group of lower cost and higher strength, and refer to mixtures with:

- 40% GP and 0% LF,
- 40% GP and 1.5% LF,
- 50% GP and 0.5% LF,
- 50% GP and 1% LF,
- 50% GP and 1.5% LF,

Three results were classified to the group of lower cost and lower strength, and 4 results to the group of higher cost and higher strength. It is worth noting that the addition of powder had a very large effect on the total cost of the coating, and that the fibers had a negligible effect.

Table 6 List of MPR and ECR coefficients for the tested coatings

No	Epoxy resin [%]	GP [%]	LF [%]	MPR [%]	Δ MPR	ECR [%]	Δ ECR
1	100	0	0	100	1.00	100	1.00
2	90	10	0	94	0.94	90	0.90
3	80	20	0	115	1.15	81	0.81
4	70	30	0	111	1.11	71	0.71
5	60	40	0	106	1.06	61	0.61
6	50	50	0	89	0.89	52	0.52
7	99.5	0	0.5	91	0.91	100	1.00
8	89.5	10	0.5	97	0.97	91	0.91
9	79.5	20	0.5	93	0.93	81	0.81
10	69.5	30	0.5	94	0.94	71	0.71
11	59.5	40	0.5	98	0.98	62	0.62
12	49.5	50	0.5	101	1.01	52	0.52
13	99.0	0	1.0	87	0.87	100	1.00
14	89.0	10	1.0	88	0.88	91	0.91
15	79.0	20	1.0	95	0.95	81	0.81
16	69.0	30	1.0	100	1.00	71	0.71
17	59.0	40	1.0	88	0.88	62	0.62
18	49.0	50	1.0	106	1.06	52	0.52
19	98.5	0	1.5	96	0.96	101	1.01
20	88.5	10	1.5	88	0.88	91	0.91
21	78.5	20	1.5	89	0.89	81	0.81
22	68.5	30	1.5	117	1.17	72	0.72
23	58.5	40	1.5	111	1.11	62	0.62
24	48.5	50	1.5	104	1.04	52	0.52

6 Conclusions

The use of rock powders is the subject of many studies. In turn, natural fibers are rarely used in the construction industry to modify the properties of construction products. The combination of the three ingredients presented in this article (epoxy resin, granite powder and linen fibers) is a big novelty. Until now these materials have not been used together. The conducted strength and cost-economic analysis confirms the validity of these tests. The addition of granite powder in the amount of 0–50% (variable every 10%) in relation to the mass of resin, and the addition of linen fibers in the amount of 0–1.5% (variable every 0.5%) in relation to the mass of resin, was tested. The main conclusions from the study are:
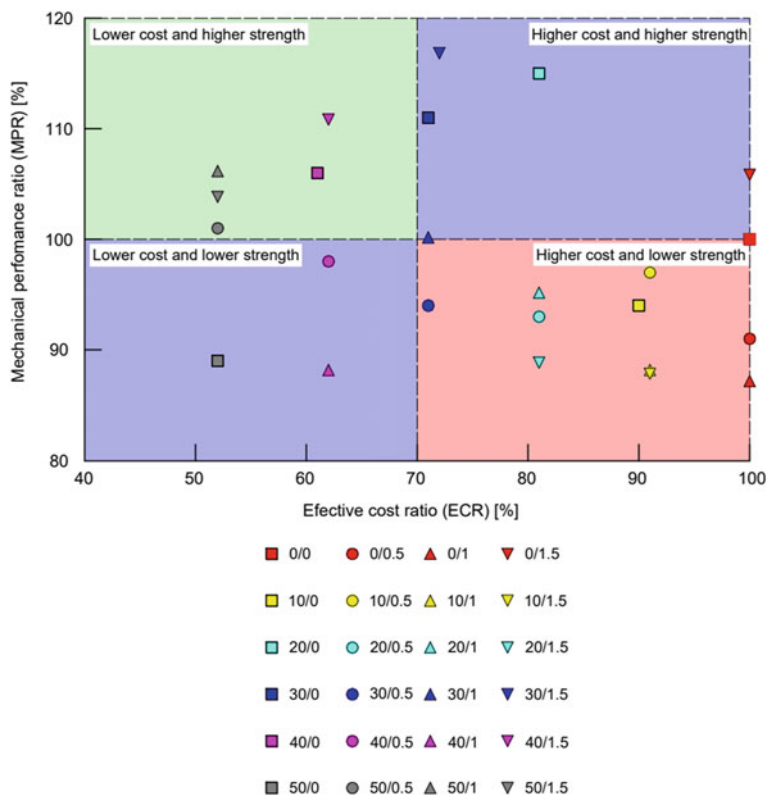
Fig. 12 Mechanical Performance Ratio (MPR) and Effective Cost Ratio (ECR) for the tested coatings with regards to the amount of granite powder and linen fibers

- an increase in strength was found in the case of 9 coatings, and the highest value was 3.09 MPa ($\sigma = 0.17$ MPa), which is 0.46 MPa (17.5%) better than that of the reference coating. This value was obtained with the addition of 1.5% of linen fibers and 30% of granite powder,
- a cost-economic analysis showed that the addition of granite powder results in a significant cost reduction, while the addition of fibers does not significantly affect the cost. 5 coatings were characterized with a lower cost and higher strength. This allows the designer to freely select a specific material solution,
- the use of rock powders, even waste ones, is the right direction for research concerning the modification of resin coatings. A similar conclusion can be drawn in the case of natural fibers. This research shows that it is good to use waste and natural materials to reduce the consumption of toxic materials such as epoxy resin.

References

1. Kampa, Ł, Chowaniec, A., Królicka, A., Sadowski, Ł: Adhesive properties of an epoxy resin bonding agent modified with waste granite powder. J. Coat. Technol. Res. **11998**, 2022 (2022)
2. Kampa, Ł., Sadowski, Ł.: Engineering technology and preparation of coating systems made with epoxy resin-based bonding agents modified with the addition of granite powder sourced from quarry Wastes. In: da Silva, L.F.M., Adams, R.D. (eds.) 6th International (2021)
3. Chowaniec, A.: The effect of the viscosity and the contact angle on the pull-off strength of epoxy resin modified with waste granite powders. In: 6th International Conference on Adhesive Bonding 2021 (pp. 83–102). Springer, Cham (2021)
4. Sadowski, Ł., Kampa, Ł., Chowaniec, A., Królicka, A., Żak, A., Abdoulpour, H., Vantadori, S.: Enhanced adhesive performance of epoxy resin coating by a novel bonding agent. Constr Build Mater **301** (2021)
5. Hajduk, P.: Projektowanie podłóg przemysłowych. PWN, Warszawa (2013)
6. Drozd W., Kowalik M.: Współczesne posadzki przemysłowe. Przegląd Budowlany 7–8 (2014)
7. Zych, T.: Współczesny fibrobeton – Możliwość kształtowania elementów konstrukcyjnych i form architektonicznych. Czasopismo Techniczne, Wydawnictwo Politechniki Krakowskiej (2010)
8. Seidler, P.: Handbuch Industriefussböden. Planung, Ausführung, Instandhaltung, Sanierung, 3 vollig neubearbeitete und erweitete Auflage, Expertverlag 1994, 4 Auflage, Expertverlag (2001)
9. Zając, G.: Posadzki w parkingach wielopoziomowych i garażach podziemnych. Materiały Budowlane **9**, 433 (2008)
10. https://ciecie-betonu.pl/offer/12/srutowanie-betonu
11. https://www.kaercher.com/pl/professional/know-how-dla-profesjonalistow/piaskowanie-hyd ropiaskowanie-piaskowanie-na-mokro.html
12. https://www.apconbuilding.pl/srutowanie-betonu-szlifowanie-czy-frezowanie-co-wybrac/
13. https://matbau.com/wp-content/uploads/2020/11/KT_NANOTOP.pdf
14. Hajduk, P.: Projektowanie podłóg przemysłowych. Wydawnictwo Naukowe PWN, Warszawa (2013)
15. https://www.sicon.pl/blog/posadzki-zywiczne-wady-i-zalety/
16. https://sztuka-architektury.pl/article/12390/posadzki-zywiczneepoksydowe-vs-poliuretanowe
17. Sadowski, Ł., Czarnecki, S., Hoła, J.: Evaluation of the height 3D roughness parameters of concrete substrate and the adhesion to epoxy resin. Int. J. Adhes. Adhes. (2016)
18. Krzywiński, K., Sadowski, Ł: The effect of texturing of the surface of concrete substrate on the pull-off strength of epoxy resin coating. Coatings **9**, 143 (2019)
19. He, Y.J., Mote, J., Lange, D.A.: Characterization of microstructure evolution of cement paste by micro computed tomography. J. Cent. South Univ. **20**, 1115–1121 (2013)
20. Mirmoghtadaei, R., Mohammadi, M., Samani, N.A., Mousavi, S.: The impact of surface preparation on the bond strength of repaired concrete by metakaolin containing concrete. Constr. Build. Mater. **80**, 76–83 (2015)
21. Chowaniec, A., Sadowski, Ł., Żak, A.: The chemical and microstructural analysis of the adhesive properties of epoxy resin coatings modified using waste glass powder. Appl. Surf. Sci. **504**, 144373 (2020)
22. Hao, Y., Liu, F., Shi, H., Han, E., Wang, Z.: The influence of ultra-fine glass fibers on the mechanical and anticorrosion properties of epoxy coatings. Prog. Org. Coat. **71**, 188–197 (2011)

23. Kampa, Ł., Chowaniec, A., Królicka, A., Sadowski, Ł.: The effect of the addition of polypropylene fibers to primer on the pull-off strength of epoxy resin coatings. Materials 4674 (2020)
24. Prabhu, T.N., Hemalatha, Y.J., Harish, V., Prashantha, K., Iyengar, P.: Thermal degradation of epoxy resin reinforced with polypropylene fibers. J. Appl. Polym. Sci. **104**, 500–503 (2007)
25. Dutra, R.C.L., Soares, B.G., Campos, E.A., Silva, J.L.G.: Hybrid composites based on polypropylene and carbon fiber and epoxy matrix. Polymer **41**, 3841–3849 (2000)
26. Kampa, Ł., Sadowski, Ł., Królicka, A.: The use of synthetic and natural fibers in epoxy coatings: a comparative mechanical and economic analysis. Int. J. Adhes. Adhes. 103017 (2021)
27. Dong, W., Liu, H., Park, S., Jin, F.: Fracture toughness improvement of epoxy resins with short carbon fibers. J. Indus. Eng. Chem. 1220–1222 (2014)
28. Chowaniec, A., Czarnecki, S., Sadowski, Ł.: The effect of the amount and particle size of the waste quartz powder on the adhesive properties of epoxy resin coatings. Int. J. Adhes. Adhes. **117** (2022)
29. Raj, M., Raj, L., Maheta, J., Patel, S.: Comparative studies on carbon fiber reinforced composites based on trifunctional epoxy resin and commercial epoxy resin. Polym. Polym. Compos. **29**(8), 1282–1290 (2021)
30. Kasemura, T., Komatu, C., Nishihara, H., Takahashi, S., Oshibe, Y., Ohmura, H., Yamamoto, T.: Surface modification of epoxy resin with silicone-containing block copolymers. J. Adhes. 0021–8464 (1993)
31. Wirries, J., Mayer, B., Rütters, M.: A novel in situ method to determine volume shrinkage of curing adhesives. J. Adhes. (2023)
32. https://www.sitech.net.pl/
33. PN-EN 13670: Wykonywanie konstrukcji z betonu
34. https://sksm.pl/product/maczki-skaleniowo-kwarcowe
35. https://unipak.dk/application/files/7116/4665/9178/Unigarn_PL-pl_v2_0.pdf
36. ASTM D4541-17: Standard Test Method for Pull-off Strength of Coatings Using Portable Adhesion Testers, pp. 1–6. ASTM International: West Conshohocken, PA, USA (2017)
37. PN-EN 13791: Ocena wytrzymałości betonu na ściskanie w konstrukcjach i prefabrykowanych wyrobach betonowych

Joint Design

Investigation of Adherend Thickness in Thin-Ply Hybrid Laminates

Farin Ramezani ⓘ**, João C. M. Salazar, Ricardo J. C. Carbas** ⓘ**, Eduardo A. S. Marques** ⓘ**, and Lucas F. M. da Silva** ⓘ

Abstract The use of composite materials has been continuously increasing, hinged on its multiple advantages such as their high strength-to-weight ratio. However, this type of material is known for its anisotropic properties that may lead to premature failure of the composite laminate, stemming from the delamination of the adherend in an adhesively bonded composite joint. This study aims to study the effect of adherend thickness in uni-directional (UD) hybrid composite single lap joints reinforced by thin-ply and investigate the joint strength and failure mode. Tensile tests were carried out to evaluate the parameters mentioned experimentally, and numerical models were developed to reproduce the joint behavior. Experimental results show that adherend thickness has a minor effect on the joint strength in hybrid composite joints reinforced by thin-ply. However, a considerable change in the failure mode was observed.

Keywords Adhesive bonding · Cohesive zone modeling · Thin-ply · Single lap joints · Hybrid composite laminates

1 Introduction

The utilization of composite materials within the field of mechanical engineering, particularly in the production of automotive, aeronautical, and aerospace components and structures, has exhibited a consistent upward trajectory in recent times [1]. This upward trajectory is projected to persist, primarily due to the inherent advantages offered by these materials, including enhanced performance characteristics and their ability to maintain a lightweight profile when compared to traditional metallic

F. Ramezani · R. J. C. Carbas (✉)
Institute of Science and Innovation in Mechanical and Industrial Engineering, Rua Dr Roberto Frias, 4200-465 Porto, Portugal
e-mail: rcarbas@fe.up.pt

J. C. M. Salazar · R. J. C. Carbas · E. A. S. Marques · L. F. M. da Silva
Department of Mechanical Engineering, Faculty of Engineering, University of Porto, Rua Dr Roberto Frias, 4200-465 Porto, Portugal

materials [2, 3]. These attributes align well with the pressing need for increased efficiency and reduced weight, both of which are pivotal in curbing energy consumption in aircraft and automobile operations.

Composite materials are widely acknowledged for their distinct structural properties, characterized by their anisotropic mechanical behavior. These materials exhibit varying degrees of strength in different directions, with one orientation typically demonstrating significant strength while other orientations may exhibit lower strength and even brittleness. Among the frequently employed composite materials in this field, carbon fiber-reinforced plastic (CFRP) stands out. When subjected to loads perpendicular to the fiber direction, CFRP is known to exhibit a specific response, delamination, a phenomenon in which the layers within the composite begin to separate. This delamination can lead to premature failure of the composite structure [4]. Numerous research endeavors have explored techniques aimed at modifying joints to mitigate delamination in adhesively bonded composite joints [4–7]. However, the incorporation of these techniques often necessitates an additional production step, resulting in increased production costs. Moreover, the intricate nature of these methods often limits their practical application [8, 9].

In recent times, the introduction of advanced spread tow techniques has ushered in the production of thinner plies with a more uniform fiber distribution and reduced resin-rich regions, which deviates from conventional methods [10]. This results in plies characterized by a more homogenous fiber distribution and smaller resin-rich regions [10], allowing for the achievement of a remarkably thin-ply thickness, as low as 0.02 mm. Generally, plies with a thickness of less than 100 μm are referred to as thin-plies [11]. The reduction in the thickness of individual layers significantly increases the number of potential layers within a given plate thickness, thereby expanding the design possibilities [12], Additionally, it results in a greater number of interfaces in thin-ply laminates, which, in turn, reduces shear stresses [12, 13]. Furthermore, thin-ply laminates are renowned for their ability to postpone the initiation of matrix damage mechanisms, suppress transverse microcracking [13] and minimize free edge delamination [12, 14] under static, fatigue, and impact loads. Due to their exceptional resistance to damage and delamination, thin-ply laminates have the potential to exhibit elevated interlaminar shear properties [15] and strain energy [16] in comparison to conventional plies. Consequently, thinner composite plies are recognized for their superior in situ transverse strength [13].

In a previous study conducted by the authors [17], it was demonstrated that substituting conventional composite layers with thin-ply layers in the adherends of a single lap joint can significantly enhance the strength of the composite joint, as well as improve the failure mode (by reducing delamination) under static loads. The authors attribute this change to the improved ductility of the laminate, which can delay delamination [18]. Moreover, experimental observation clearly demonstrated that the presence of thin-plies acts as a barrier against crack propagation.

The present study delves into the influence of adherend thickness in hybrid single lap joints (SLJs) reinforced with thin-ply layers. In order to gain a deeper insight into how adherend thickness impacts the strength and failure characteristics of hybrid single lap joints strengthened with thin-ply materials, a series of experimental

tests were conducted. Specifically, hybrid single lap joints, where 25% of the total adherend thickness was composed of thin-ply material, referred to as "hybrid (25% thin-ply) [17]," were fabricated and examined. The adherend thicknesses considered for these joints were 3.0, 3.6, and 4.0 mm. The experimental results indicate that the thickness of the adherend has a limited impact on the overall strength of hybrid composite joints reinforced with thin-plies. However, a noteworthy change in the failure mode was readily apparent.

2 Experimental Details

2.1 *Adhesive*

The adhesive utilized in this study was an epoxy structural adhesive, provided in film form, under the commercial designation Scotch Weld AF 163-2k (3 M, Saint Paul, Minnesota, USA), possessing the following material properties: Young's modulus (E) of 1.5 GPa, shear modulus (G) of 0.6 GPa, tensile strength (σ) of 46.9 MPa, shear strength (τ) of 46.8 MPa, and fracture energy ($G_{IC} = 4.05$ and $G_{IIC} = 9.77$ N/mm) [19]. The curing process for the adhesive adhered to the manufacturer's recommendations, involving heating at 130 °C for a duration of 2 hours.

2.2 *Adherend*

2.2.1 Conventional Composite

The selection of materials for the configurations under investigation was undertaken with great care to ensure their suitability for possible aerospace applications. Accordingly, a unidirectional prepreg carbon-epoxy composite featuring a ply thickness of 0.15 mm was meticulously chosen, bearing the commercial designation "Texipreg HS 160 T700" (Seal Spa, Legnano, Italy). This material boasts the following crucial properties: Young's modulus ($E_1 = 109.0$ and $E_2 = 8.8$ GPa), shear modulus ($G_{12} = 4.3$ and $G_{13} = 3.2$ GPa), and fracture energy ($G_{IC} = 0.6$ and $G_{IIC} = 1.2$ N/mm) [20, 21]. These selections were made with the primary objective of aligning the study with potential applications within the aerospace sector.

2.2.2 Thin-Ply

In the context of this investigation, a carefully chosen thin-ply material was employed, specifically a unidirectional carbon-epoxy prepreg composite with a ply thickness of 0.075 mm, oriented at 0°. This particular material is denoted by the commercial

reference "NTPT-TP415" and is sourced from North Thin-Ply Technology, Poland. It possesses the following material properties: Young's modulus (E_1 = 101.7 and E_2 = 5.7 GPa), shear modulus (G_{12} = 3.0 and G_{13} = 3.0 GPa), and fracture energy (G_{IC} = 0.7 and G_{IIC} = 0.8 N/mm) [22]. The choice of this material aligns seamlessly with the research objectives and its potential applications.

2.3   Single Lap Joint Manufacturing

The fabrication process for creating the single lap joints involved a meticulous layer-by-layer assembly, combining both traditional composite and thin-ply prepregs to achieve the desired thickness of the adherends. In the case of the hybrid single lap joint, which incorporated 25% thin-ply material and had an adherend thickness of 3.6 mm, 18 plies of conventional composite were combined with 12 plies of thin-ply material on the adherend tops (equivalent to 6 layers of thin-ply on each adherend top, as depicted in Fig. 1). This combination resulted in a composite composition consisting of 25% thin-ply material. To facilitate bonding, an additional layer of adhesive was applied between the adherends. The single lap joints (SLJs) were manufactured according to the geometry illustrated in Fig. 2.

A mold was employed to ensure the thickness of the adherends and adhesive, and to enable easy removal of the specimens from the mold after curing, a release agent was applied. Figure 3 shows the manufactured specimens before the curing process. The study also investigated the effect of the curing sequence on the mechanical properties of the joints by comparing joints where the composite and adhesive were

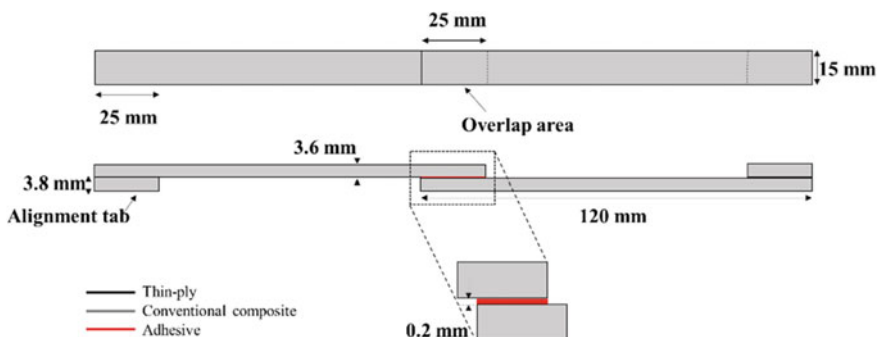**Fig. 1** Scheme design of hybrid (25% thin-ply) single lap joint

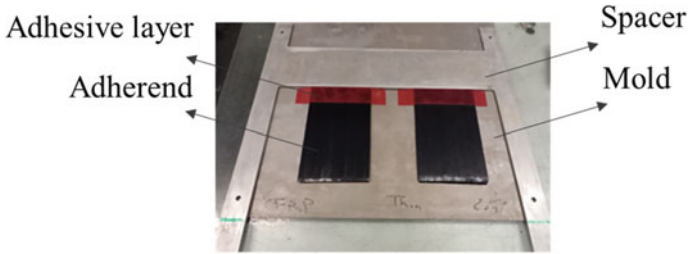**Fig. 2** Schematic design of the manufactured specimens

Fig. 3 Manufactured specimens before the curing process

cured simultaneously (co-cured) with joints where these components were cured separately. The results indicated that, in the case of the AF163-2k adhesive used in this study, the curing sequence did not significantly influence the mechanical properties of the joints. Consequently, a one-step curing process was adopted as the preferred manufacturing method, offering benefits such as reduced production time and energy consumption. The joint assemblies were cured at 130 °C for a duration of two hours, following the manufacturer's recommended procedure.

2.4 Testing Condition

The single lap joints (SLJs) underwent testing in an Instron 8801 servo hydraulic testing machine, equipped with a 100 kN load cell. The tests were conducted at a constant crosshead speed of 1 mm/min. It's important to note that all tests were carried out under controlled laboratory environmental conditions, with a room temperature of 24 °C and a relative humidity of 55%. For each configuration under analysis, the testing process was repeated four times to ensure data consistency and reliability. Figure 4 presents the intact and damaged specimen in testing machine.

3 Numerical Details

Numerical models employing the finite element method and utilizing Abaqus software were created to simulate the behavior of the configurations under investigation. To streamline the problem and minimize computational time, two-dimensional (2D) static load models were generated. The boundary conditions were set up as illustrated in Fig. 5, with the left end of the joint being fixed, while a displacement was applied to the right end to replicate the loading conditions. Specifically, a displacement of 1 mm was imposed on the numerical models, a value determined based on experimental findings to ensure the occurrence of failure.
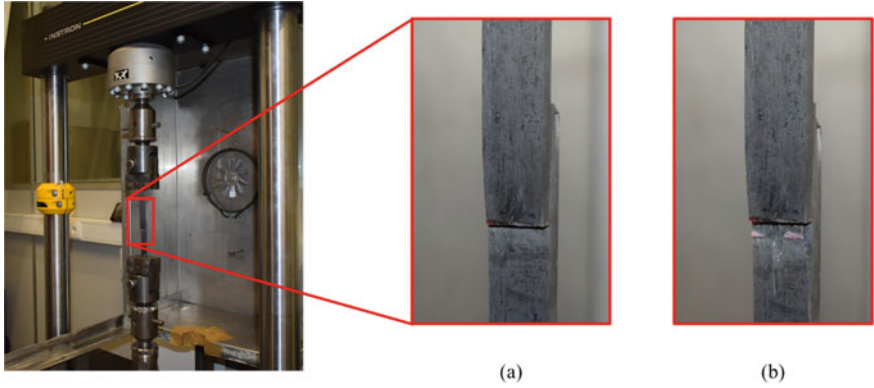
Fig. 4 **a** Intact, **b** failed specimen in testing machine
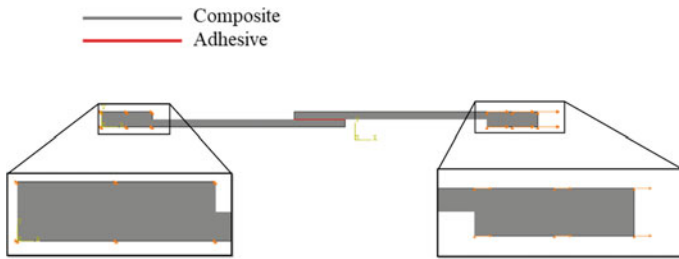

Fig. 5 Boundary condition of simulated single lap joints

To model the adhesive behavior, cohesive zone modeling (CZM) was employed, utilizing four-node elements (cohesive quadrilateral elements). The simulation also took into account nonlinear geometric effects. Solid cohesive elements, governed by traction–separation laws, were applied to the adhesive layer in all models to replicate the evolution of damage, including its initiation and propagation.

Cohesive behavior was precisely defined using a traction–separation law, which has been demonstrated to effectively represent delamination in composite laminates. A similar CZM based approach was incorporated into the composite materials, whether they were conventional or thin-ply composites, to simulate delamination consistent with the experimental failure mode observed (refer to Fig. 6).

The CZM layers were positioned at specific distances from the adherend-adhesive interface, depending on the thickness of the adherends (3.0, 3.6, or 4.0 mm). These distances approximately matched the experimentally measured position of the delamination plane from the adhesive layer. Notably, the thickness of the cohesive layer corresponded to that of a single equivalent composite ply (0.075 mm for thin-ply and 0.15 mm for the conventional composite).

A biased mesh distribution was applied to all the models, with a more refined mesh located near the edges of the overlap, with less detail near the extreme ends
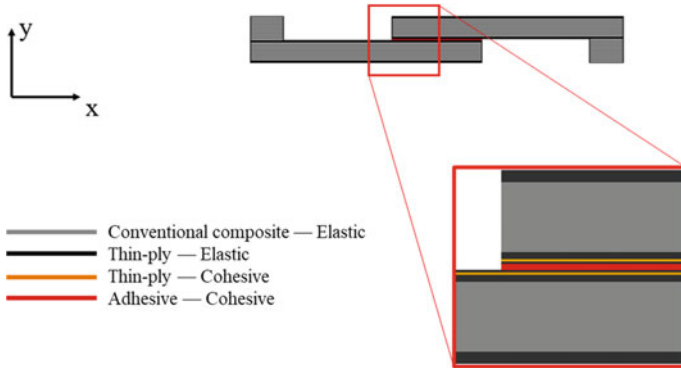
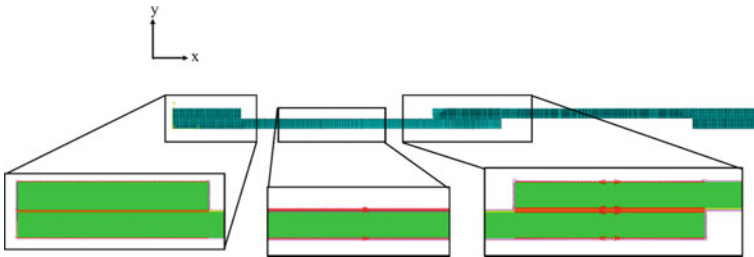**Fig. 6** Representative experimentally obtained load–displacement curves for

Fig. 7 Mesh distributions for single lap joint

of both adherends, making the model lighter to process. Double and single biased meshed were applied in the x direction to the bondline and the adherend respectively, with seed size ranging from 0.2 to 0.5 mm (see Fig. 7). On the extreme ends of the adherends and the end tabs, a mesh with 0.5 mm was implemented mm in the x direction. The mesh was uniform through the thickness (y direction) with a size of 0.2 mm for all configurations. The resulting mesh consisted of approximately 15,000 elements.

4 Results

Manufactured specimens were submitted to uniaxial tensile tests. Figures 8 and 9 presents a representative experimentally obtained load–displacement curve and obtained failure mode for the mentioned configurations respectively. The results of the experiments reveal that the increase of the adherend thickness results in a venial increase in the joint strength of the hybrid composite joints that have been enhanced with thin-ply reinforcement. Nevertheless, a significant modification in the failure mode was observed. The failure mode changes from a full delamination failure

surface of the composite joint with 3.0 mm adhered thickness to partial delamination when increased up to 4.0 mm. Figure 8 also presents the numerically obtained load–displacement curve for the mentioned configurations. As seen the increase in the adherend thickness from 3.0 to 3.6 mm does not affect the tensile strength of the composite joint, this is while the increase of the adhered thickness from 3.6 to 4 mm of the hybrid (25% thin-ply) composite single lap joint leads to a slight increase in the tensile strength of the composite joint.

Figure 10 presents a comparison between the numerical and experimentally obtained results. As seen, the numerical and experimentally obtained results are in a good agreement. The experimental result obtained by the authors in the previous study was presented [17]. As seen the use of hybrid (25% thin-ply) single lap joints could increase the failure load up to 90% (in the case of 3.6 mm adherend thickness). This is known to be due to the improved ductility of the laminate, which can delay delamination [18]. Moreover, experimental observation clearly demonstrated that the presence of thin-plies acts as a barrier against crack propagation therefore improve the failure mode (by reducing delamination) under static loads [17]. However, adherend thickness has a negligible effect on the joint strength in hybrid composite joints reinforced by thin-ply. This is while a considerable change in the failure mode was observed changing from fully delaminated failure surface (from 3.0 mm adherend thickness) to partial delamination when increased up to 4.0 mm.
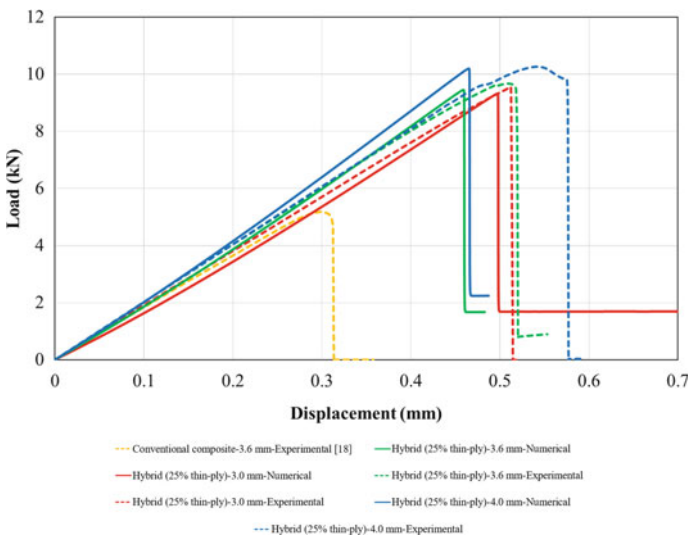

Fig. 8 Representative experimentally obtained load–displacement curve for reference conventional composite, hybrid (25% thin-ply) single lap joint with 3.0, 3.6, and 4.0 mm adherend thickness and related numerical models
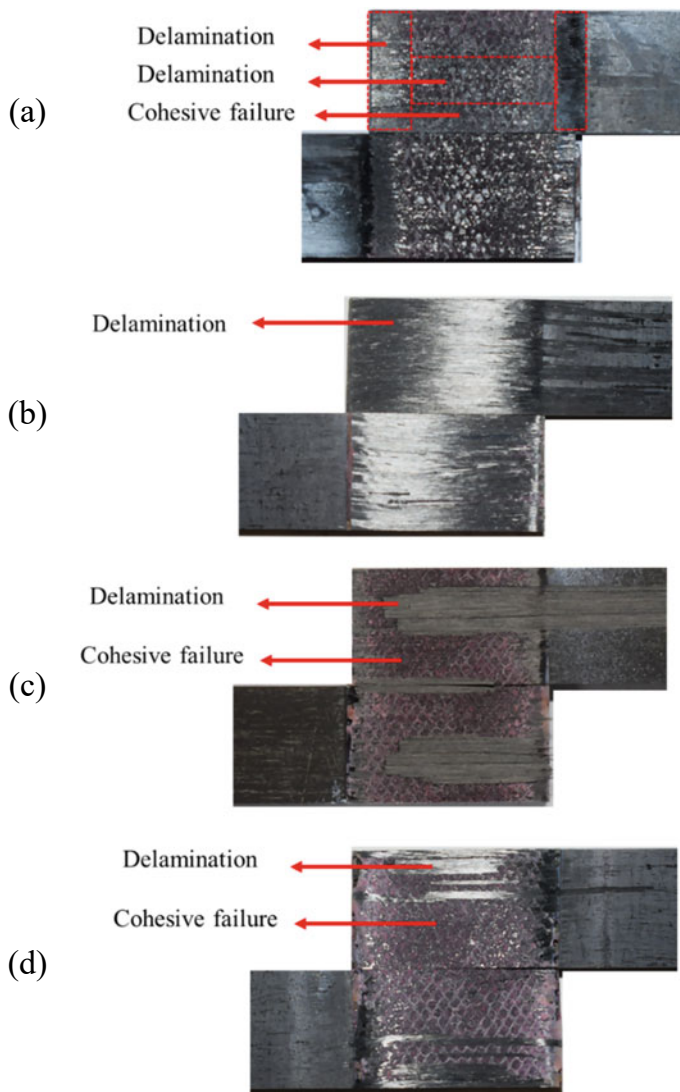
Fig. 9 Failure surface of **a** reference conventional composite with the adherend thickness of 3.6 mm [17] and hybrid (25% thin-ply) single lap joint with **b** 3.0, **c** 3.6 and **d** 4.0 mm adherend thickness
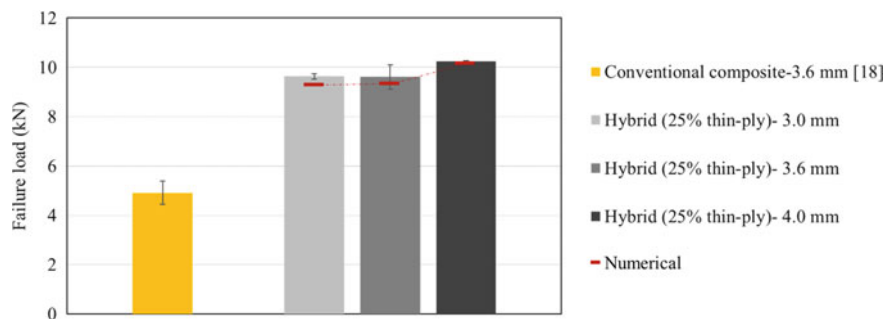
Fig. 10 Average experimentally obtained failure load for hybrid (25% thin-ply) single lap joint with 3.0, 3.6, and 4.0 mm adherend thickness in comparison with the equivalent numerical result

5   Conclusion

This study examines the influence of adherend thickness on the performance of hybrid composite single lap joints strengthened with thin-ply reinforcement. Three different adherend thicknesses were considered and the manufactured specimen was conducted to tensile test. From the experimentally obtained results and the numerical models produced the main conclusions are:

- A marginal rise in the failure load was noted when the adherend thickness was increased in the hybrid composite joint reinforced with thin-ply.
- A notable alteration in the failure mode was clearly evident, changing the failure mode from full delamination to partial delamination.
- Numerical models employing finite element methods were generated to replicate the behavior of the configurations. Cohesive zone modeling was used to model the failure in the adhesive layer and delamination in the composite adherends. The numerical models show good agreement with the experimentally obtained results.

Data Availability Statements Not Applicable.

Conflict of Interest   Not Applicable.

References

1. Sahu, P., Gupta, M.: A review on the properties of natural fibres and its bio-composites: effect of alkali treatment. Proc. Inst. Mech. Eng. L: J. Mater.: Des. Appl. **234**, 198–217 (2020). https://doi.org/10.1177/1464420719875163

2. Zhou, M., Gu, W., Wang, G., Zheng, J., Pei, C., Fan, F., Ji, G.: Sustainable wood-based composites for microwave absorption and electromagnetic interference shielding. J. Mater. Chem. A. **8**, 24267–24283 (2020). https://doi.org/10.1039/d0ta08372k

3. Budzik, M.K., Wolfahrt, M., Reis, P., Kozłowski, M., Sena-Cruz, J., Papadakis, L., Nasr Saleh, M., Machalicka, K.V., Teixeira de Freitas, S., Vassilopoulos, A.P.: Testing mechanical performance of adhesively bonded composite joints in engineering applications: an overview. J Adhes. **98**, 2133–2209 (2022). https://doi.org/10.1080/00218464.2021.1953479

4. Zhou, X., Li, J., Qu, C., Bu, W., Liu, Z., Fan, Y., Bao, G.: Bending behavior of hybrid sandwich composite structures containing 3D printed PLA lattice cores and magnesium alloy face sheets. J. Adhes.Adhes. **98**, 1713–1731 (2022). https://doi.org/10.1080/00218464.2021.1939015

5. Ramezani, F., Simões, B.D., Carbas, R.J.C., Marques, E.A.S., da Silva, L.F.M.: Developments in laminate modification of adhesively bonded composite joints. J. Mater. **16**, 568 (2023). https://doi.org/10.3390/ma16020568

6. Akhavan-Safar, A., Ramezani, F., Delzendehrooy, F., Ayatollahi, M.R., da Silva, L.F.M.: A review on bi-adhesive joints: benefits and challenges. Int. J. Adhes.Adhes. **114**, 103098 (2022). https://doi.org/10.1016/j.ijadhadh.2022.103098

7. Ramezani, F., Nunes, P.D.P., Carbas, R.J.C., Marques, E.A.S., da Silva, L.F.M.: The joint strength of hybrid composite joints reinforced with different laminates materials. J. Adv. Join. Process. **5**, 100103 (2022). https://doi.org/10.1016/j.jajp.2022.100103

8. Verpoest, I., Wevers, M., de Meester, P.: 3D-fabrics for composite sandwich structures. 535–541 (1989). https://doi.org/10.1007/978-94-009-1123-9_74

9. Dransfield, K., Baillie, C., Mai, Y.-W.: Improving the delamination resistance of CFRP by stitching—a review. Compos. Sci. Technol. **50**, 305–317 (1994). https://doi.org/10.1016/0266-3538(94)90019-1

10. Amacher, R., Cugnoni, J., Botsis, J., Sorensen, L., Smith, W., Dransfeld, C.: Thin ply composites: experimental characterization and modeling of size-effects. Compos. Sci. Technol. **101**, 121–132 (2014). https://doi.org/10.1016/j.compscitech.2014.06.027

11. Arteiro, A., Catalanotti, G., Xavier, J., Linde, P., Camanho, P.P.: A strategy to improve the structural performance of non-crimp fabric thin-ply laminates. Compos. Struct. **188**, 438–449 (2018). https://doi.org/10.1016/j.compstruct.2017.11.072

12. Kötter, B., Karsten, J., Körbelin, J., Fiedler, B.: CFRP thin-ply fibre metal laminates: influences of ply thickness and metal layers on open hole tension and compression properties. J. Mater. **13**, 910 (2020). https://doi.org/10.3390/ma13040910

13. Wisnom, M.R., Khan, B., Hallett, S.R.: Size effects in unnotched tensile strength of unidirectional and quasi-isotropic carbon/epoxy composites. Compos. Struct. **84**, 21–28 (2008). https://doi.org/10.1016/j.compstruct.2007.06.002

14. Kim, R.Y., Soni, S.R.: Experimental and analytical studies on the onset of delamination in laminated composites. J. Compos. Mater. **18**, 70–80 (1984). https://doi.org/10.1177/002199838401800106

15. Huang, C., He, M., He, Y., Xiao, J., Zhang, J., Ju, S., Jiang, D.: Exploration relation between interlaminar shear properties of thin-ply laminates under short-beam bending and meso-structures. J. Compos. Mater. **52**, 2375–2386 (2018). https://doi.org/10.1177/0021998317745586

16. Kupski, J., Zarouchas, D., Teixeira de Freitas, S.: Thin-plies in adhesively bonded carbon fiber reinforced polymers. Compos. B. Eng. **184**, 107627 (2020). https://doi.org/10.1016/j.composites b.2019.107627

17. Ramezani, F., Carbas, R.J.C., Marques, E.A.S., da Silva, L.F.M.: Study of hybrid composite joints with thin-ply-reinforced adherends. J. Mater. **16**, 4002 (2023). https://doi.org/10.3390/ma16114002

18. Ramezani, F., Carbas, R.J.C., Marques, E.A.S., Ferreira, A.M., da Silva, L.F.M.: A study of the fracture mechanisms of hybrid carbon fiber reinforced polymer laminates reinforced by thin-ply. Polym. Compos. **44**, 1672–1683 (2023). https://doi.org/10.1002/pc.27196

19. Morgado, M.A., Carbas, R.J.C., dos Santos, D.G., da Silva, L.F.M.: Strength of CFRP joints reinforced with adhesive layers. Int. J. Adhes.Adhes. **97**, 102475 (2020). https://doi.org/10.1016/j.ijadhadh.2019.102475

20. Campilho, R.D.S.G., de Moura, M.F.S.F., Domingues, J.J.M.S.: Modelling single and double-lap repairs on composite materials. Compos. Sci. Technol. **65**, 1948–1958 (2005). https://doi.org/10.1016/j.compscitech.2005.04.007

21. Machado, J., Marques, E., Campilho, R., da Silva, L.F.: Mode I fracture toughness of CFRP as a function of temperature and strain rate. J. Compos. Mater. **51**, 3315–3326 (2017). https://doi.org/10.1177/0021998316682309

22. Ramezani, F., Carbas, R., Marques, E.A.S., Ferreira, A.M., da Silva, L.F.M.: Study on out-of-plane tensile strength of angle-plied reinforced hybrid CFRP laminates using thin-ply. Mech. Adv. Mater. Struct. 1–14 (2023). https://doi.org/10.1080/15376494.2023.2165742

Utilizing the Anti-Plane Punch-Through Shear Specimen for Mixed-Mode I/III Fracture Analysis of Epoxy Resins

Jamal Bidadi, Alireza Akhavan-Safar, Hamed Saeidi Googarchin, and Lucas F. M. da Silva

Abstract The primary objective of this study is to introduce and analyze a test geometry designed for measuring the shear fracture resistance of cracked epoxy resins under anti-plane loading conditions. This geometry is denoted as the anti-plane punch-through shear (APPTS) specimen. The APPTS specimen is a rectangular beam that has been weakened by two parallel pre-cracks separated by a specific longitudinal distance (S). This specimen is then subjected to anti-plane punch shear loads, commonly known as mode III loading. Initially, the APPTS specimen is modeled numerically using the contour integral method within the Abaqus code. This modeling approach helps to characterize the distribution of normalized stress intensity factors (SIFs) along the pre-crack front. The numerical simulations are conducted across a wide range of normalized pre-crack lengths relative to the specimen width (referred to as a/w), as well as normalized longitudinal distances (S) relative to the specimen length (referred to as S/L). The obtained results reveal that despite the application of an anti-plane shear load (mode III loading), the crack front of the APPTS specimen consistently experiences a combination of tensile stress (mode I) and anti-plane shear stress (mode III). This combination results in a negligible contribution of mode II stress in the crack front stress distribution. Furthermore, as the a/w ratio increases, there is a respectively a decrease and increase trend in the

J. Bidadi · H. S. Googarchin (✉)
Automotive Fluids and Structures Analysis Research Laboratory, School of Automotive Engineering, Iran University of Science and Technology (IUST), Tehran, Iran
e-mail: hsaeidi@iust.ac.ir

J. Bidadi
e-mail: jamal_bidadi@auto.iust.ac.ir

A. Akhavan-Safar
Institute of Science and Innovation in Mechanical and Industrial Engineering (INEGI), Porto, Portugal
e-mail: aAkhavan-safar@inegi.up.pt

L. F. M. da Silva
Faculty of Engineering, Department of Mechanical Engineering, University of Porto, Porto, Portugal
e-mail: Lucas@fe.up.pt

influence of modes I and mode III on the stress state of the crack front. In other words, by increasing the *a/w* ratio, the mode I stress does not reach zero, while mode III increases signifying the dominance of mode III loading. In addition to this, the ratio of normalized mode I to mode III SIFs indicates that when the *S/L* ratio is relatively low, the mode III stress state at the crack front becomes more dominant compared to the mode I stress state. In conclusion, the obtained normalized SIFs can be utilized as essential input parameters in theoretical criteria aimed at predicting the punching shear fracture envelope of cracked epoxy resin components during experimental tests.

1   Introduction

Epoxy resins are extensively utilized across various sectors, serving as the matrix phase in fiber-reinforced polymer composites and contributing to the production of diverse bulk epoxy-engineered components used in vehicles. The presence of defects, including voids, notches, and cracks within the structure of polymeric engineering materials, especially within adhesively bonded joints, is generally inevitable [1–5]. To ensure the structural integrity and load-bearing capability of such constructions, it becomes imperative to evaluate the mechanical behavior of the bulk epoxy resin components compromised by cracks. Fracture mechanics methods are employed to investigate the behavior of components with cracks. Among these methods, a crucial parameter is the stress intensity factor (SIF), which characterizes the stress state at the crack tip. In brittle or semi-brittle materials, the fracture resistance is determined by their critical SIF in cracked specimens. As depicted in Fig. 1, structures with cracks often experience failure not only in pure mode I (tensile mode) or pure mode II (in-plane shear mode) but also under mixed-mode I/III loading conditions. Therefore, the assessment of fracture behavior, particularly in cases involving pure mode III or mixed-mode I/III loading conditions, holds significant importance in the design of practical components. In a recent study [5], epoxy adhesive fracture behavior was explored under mixed mode (I/III) conditions via a custom apparatus. Butt joints with a pre-crack in the adhesive layer were created and tested. Using SIFs calculated from experimental data, modes I and III fracture energies were obtained from a 3D finite element analysis (FEA) using XFEM. The results demonstrated the suitability of XFEM for mixed I/III loading of the tested joints. However, it should be noted that in bonded structures, the stress distribution within the adhesive layer is notably influenced by the properties and geometry of the substrates. Accordingly, in some studies the fracture behaviour of bulk materials was investigated.

The mixed-mode I/II fracture behavior of bulk epoxy resin components has been the focus of extensive research to date, leading to the proposition of a wide variety of test specimens for the assessment of mixed-mode I/II fracture toughness. In this
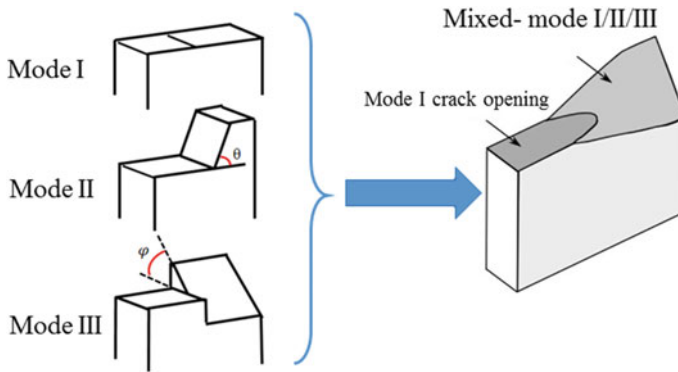
Fig. 1 Schematic view of the crack face deformation modes in engineering materials
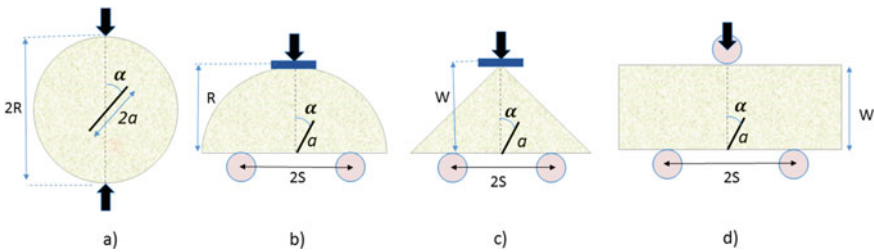

Fig. 2 Various types of test specimens utilized for mixed-mode I/II crack face deformation in polymeric materials: **a** Brazilian disk, **b** semi-circular, **c** triangular shapes, and **d** rectangular-beam

regard, various geometries, such as the semi-circular [6, 7], Brazilian disk [8], rectangular beam [9, 10], triangular shapes [11, 12], and rectangular-beam have frequently been employed in numerous studies (refer to Fig. 2).

As mentioned above, the mixed-mode I/III crack face critical deformation represents one of the other most prevalent failure modes in bulk epoxy resin components, yet it has received limited attention in the literature [13–17]. In the literature, several test setups have been proposed for evaluating the fracture resistance of bulk polymeric materials under pure mode III or mixed-mode I/III conditions. Examples include the compact tension (CT) specimen with a specialized fixture [14, 15], the anti-plane four-point bend (APFPB) method [18], and most recently, the ENDB (edge-notched disk bend) specimen introduced by Aliha et al. [13]. These setups have been employed to study the mixed-mode I/III fracture behavior of engineering polymers containing edge crack (see Fig. 3).

important to note that a concentrated load can potentially influence the outcomes obtained, as it leads to stress concentration at the loading points. This alteration in stress distribution subsequently impacts the mode mixity at the crack front. However, in case of a rather uniformly distributed load across the component's surface the stress at cracked region will be different for the same load level. Under such conditions,
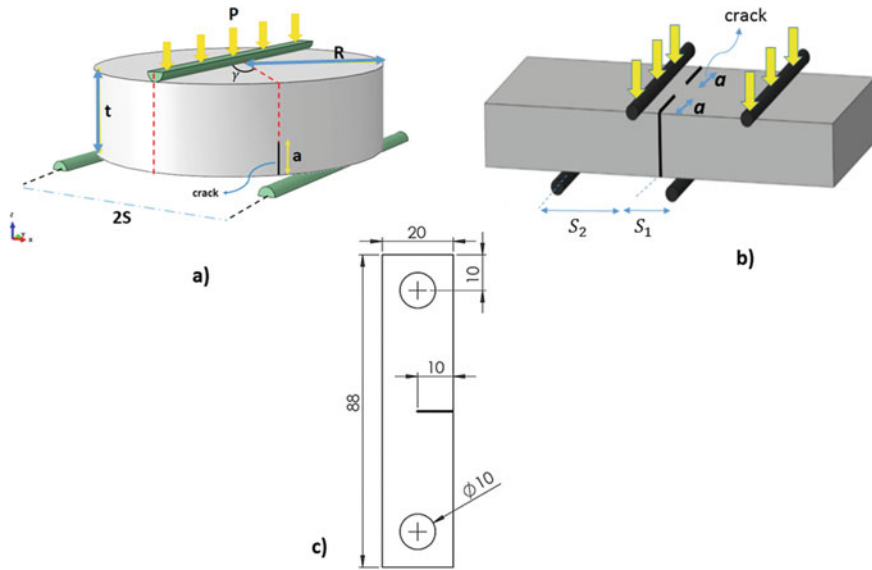
Fig. 3 Various types of test specimens utilized for mixed-mode I/III crack face deformation in polymeric materials: **a** edge-notched disk bend (ENDB), **b** anti-plane four-point bend (APFPB), **c** compact-tension (CT). (dimensions are in mm)

the crack within the specimen will be subjected to a confining stress. The application of the testing method while considering confining stress has been observed in various non-polymeric materials using punch-through shear test specimen [19]. The punch-through shear test specimen is a rectangular beam weakened by two parallel pre-cracks separated by a specific longitudinal distance which is loaded under in-plane (mode II) shear confining stress. Further examples of applying confining stress through the punch-through shear test specimen in mode II loading can be found in references [20, 21]. In a research study conducted by Rao et al. [22], the practicality of the cracked punch-through shear specimen was experimentally explored to assess the mode III fracture resistance of rock materials under confining stress. They showed that the pre-crack length has a substantial effect on the fracture resistance values. A review of the literature reveals the absence of any work regarding the application of this specimen to resins and adhesives. However, it should be noted that geometric parameters such as the normalized pre-crack length (a/w) ratio and the arrangement of the two parallel pre-cracks significantly influence the ultimate results. This specific investigation has not yet been pursued in existing literature, and the present study aims to address this research gap. Therefore, the aim of this paper is to present a comprehensive dataset of normalized stress intensity factors acquired via finite element modeling of the punch-through shear specimen under anti-plane (mode III) loading conditions. The fracture parameters introduced in this study provide the tools for analyzing the mixed-mode I/III fracture behavior of the anti-plane punch-through shear specimens. It should be highlighted that the practical

applicability of the analyzed specimen needs validation through the testing of various types of resins and adhesives in subsequent research efforts.

2 Anti-Plane Punch-Through Shear Specimen

The geometry and loading conditions of the anti-plane punch-through shear specimen are shown in Fig. 4. The external load is applied to the surface of A_1 while the A_2, and A_3 are the zone of supports. In these conditions, the specimen is under the bending moment in addition to the sheer force as shown in Fig. 4. As can be seen in the shear force and bending moment diagrams shown in Fig. 5, in addition to the sheer force, a bending moment is also present on the crack planes and the crack tip is under combined mixed-mode tensile- out-of-plane shear loading conditions. It should be noted that all dimensions are in millimeter scale and the two crack planes are exactly parallel to each other. The $L \times W \times t$ dimensions are $240 \times 40 \times 40$ mm, respectively. The geometrical dimension ratio such as the crack length to specimen width (a/w), and the longitudinal distance between two crack planes to specimen length (S/L) are the considered variable listed in Table 1. The effects of these parameters on the fracture parameters is investigated in the next section.

3 Finite Element Analysis (FEA)

The SIF is an important tool in the design of cracked components. Due to the lack of an effective analytical framework and formula for calculating the stress intensity factors in the anti-plane punch-through shear specimen, a finite element method was established to assess the SIFs distribution within the cracked body. There are several numerical methods for calculating SIFs such as the contour integral method, virtual crack growth method, and displacement method. Here, the contour integral technique was utilized through the Abaqus 6.14. As shown in Fig. 5, three-dimensional finite element models of the anti-plane punch-through shear specimen were analyzed using the second-order elements (20-node bricks) in the FE code. After a mesh convergence study, a total number of 19,761 elements were employed for the simulation of all specimen. For producing the square root singularity of the stress/strain field, the singular elements with the middle nodes at quarter-point positions were considered in the first ring of elements surrounding the crack tip. The region around the crack tip was meshed using a cylinder with at least 13 rings of elements, that each of consider 64 quadrilateral elements in the circumferential direction. For applying the boundary conditions of bottom supports, zero displacements in y-direction ($u_2 = 0$) are selected at the bottom areas A_2 and A_3. To prevent the slip of specimen, a node is constraint in x-direction ($u_1 = 0$). A reference pressure of $P = 500$ MPa was applied on the top surface (A_1 area) along the width of specimen. The material properties such as Young's modulus and Poisson's ratio are taken respectively $E = 1850$ MPa
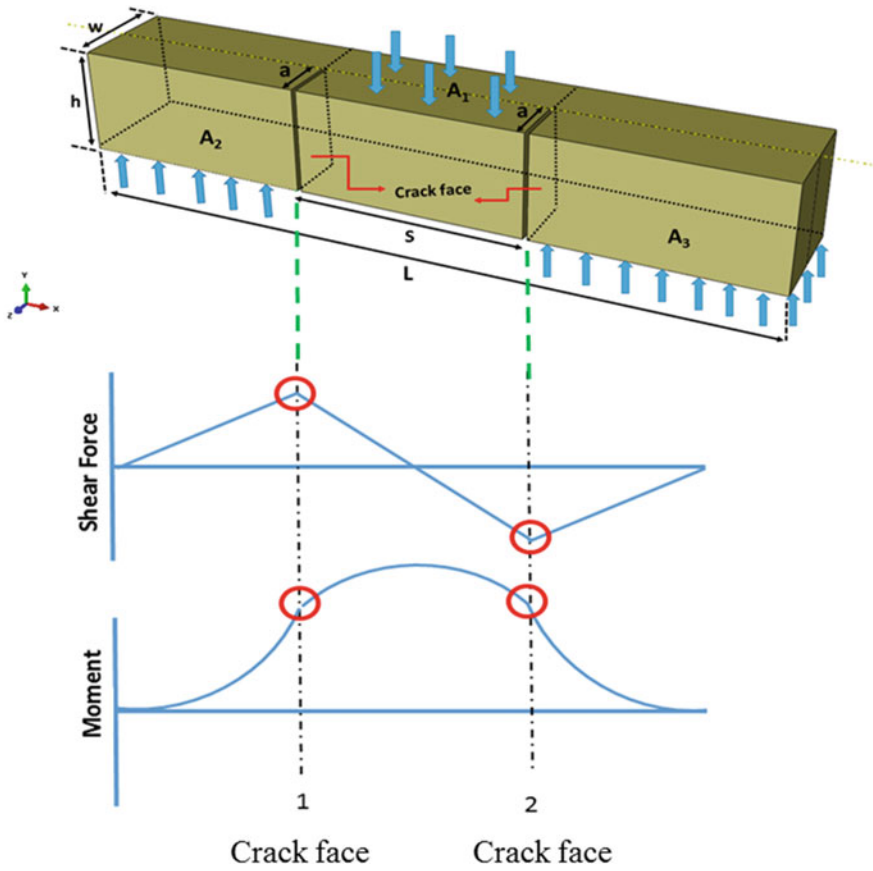
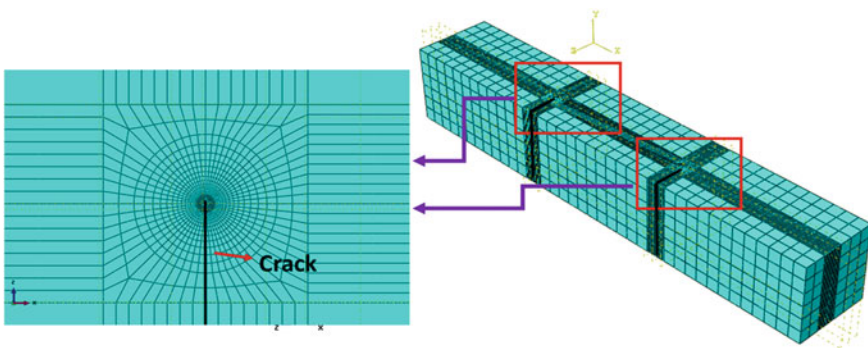**Fig. 4** Geometry and loading conditions of the anti-plane punch-through shear specimen

Fig. 5 The finite element mesh used for the specimen and its details around the crack tip

Table 1 Specimen dimensions and loading conditions

$L \times W \times h$ (mm $\times$ mm $\times$ mm)	a/w	S/L	S (mm)	a (mm)
$240 \times 40 \times 40$	0.2	0.25	60	8
		0.33	79.2	8
		0.4	96	8
		0.5	120	8
		0.6	144	8
	0.3	0.25	60	12
		0.33	79.2	12
		0.4	96	12
		0.5	120	12
		0.6	144	12
	0.4	0.25	60	16
		0.33	79.2	16
		0.4	96	16
		0.5	120	16
		0.6	144	16
	0.55	0.25	60	22
		0.33	79.2	22
		0.4	96	22
		0.5	120	22
		0.6	144	22
	0.6	0.25	60	24
		0.33	79.2	24
		0.4	96	24
		0.5	120	24
		0.6	144	24
	0.7	0.25	60	28
		0.33	79.2	28
		0.4	96	28
		0.5	120	28
		0.6	144	28

and $\nu = 0.32$ (typical values for brittle epoxy resins and adhesives) for numerical modeling of specimen.

The stress intensity factors K_I, K_{II}, and K_{III} for the anti-plane punch-through shear specimen are functions of the crack length (a), nominal stress (S_n), and geometry factors (Y_I, Y_{II}, Y_{III}) that can be written as Eqs. (2–4) based on the linear elastic fracture mechanic theory. It's important to note that the nominal stress (S_n) represents the stress induced in the uncracked beam under the loading and boundary conditions

depicted in Fig. 4. This stress value is obtained using the static equilibrium solution as shown Eq. (1):

$$Sn = \frac{3}{2} \frac{PSL}{h^2} \tag{1}$$

$$K_I = Sn\sqrt{\pi a} Y_I \tag{2}$$

$$K_{II} = Sn\sqrt{\pi a} Y_{II} \tag{3}$$

$$K_{III} = Sn\sqrt{\pi a} Y_{III} \tag{4}$$

It should be noted that the values of K_I, K_{II}, and K_{III} in Eqs. (2–4) are obtained from the FE analysis. Also, S_n is obtained by substituting the applied stress in the FE analysis ($P = 500$ MPa) and geometrical dimensions of the specimen. Finally, the normalized stress intensity factors or geometry factors (Y_I, Y_{II}, Y_{III}) are obtained by dividing the value of K_I, K_{II}, K_{III} to $Sn\sqrt{\pi a}$ as bellow:

$$Y_I = \frac{K_I}{Sn\sqrt{\pi a}} \tag{5}$$

$$Y_{II} = \frac{K_{II}}{Sn\sqrt{\pi a}} \tag{6}$$

$$Y_{III} = \frac{K_{III}}{Sn\sqrt{\pi a}} \tag{7}$$

4   Results and Discussion

As the center of the crack front is a critical point for fracture initiation and propagation occurring in cracked structures, hence, a dimensionless parameter (i.e. *z/w*) was introduced in the FE model for defining the center of the crack front in the anti-plane punch-through shear specimen. This dimensionless parameter, *z/w*, (where z is the distance from the located origin at the center of the crack front) holds the key to precisely defining and characterizing the central region of the crack front within the context of an anti-plane punch-through shear specimen. By utilizing this parameter, we are able to effectively pinpoint the specific location along the crack front that plays a pivotal role in the fracture process. Therefore, all results of stress intensity factors were extracted for *z/w* = 0 which shows the mid-section location of the specimen.

The variations of geometry factors for modes I, II, and III (Y_I, Y_{II}, and Y_{III}, respectively) in the mid-section of the specimen for different crack depth ratios of

$a/w = 0.2$ to 0.7 and various values of *S/L* are shown in Figs. 6, 7, and 8. As shown in these Figs, by increasing the crack depth ratios (*a/w*), the mode I geometry factor (Y_I) decreases and conversely Y_{III} increases. Also by increasing the *S/L* ratio both mode I and mode III geometry factors increased. The variations of Y_{II} show that, in the absence of the mode II component which has a very negligible value in the mid-section of the specimen, in general, this specimen experiences mixed mode I/ III loading.

For a better understanding, the ratio of Y_I/Y_{III} is shown in Fig. 9. As can be seen from Fig. 8, the ratio of Y_I/Y_{III} is always between 0.01 and 0.12 for all the a/w and *S/L* ratios. This finding demonstrates that, with increasing the *a/w* and decreasing *S/L* ratio, the contribution of mode III is more than mode I in crack plane deformation due to the small amount of bending moment at the crack tip,
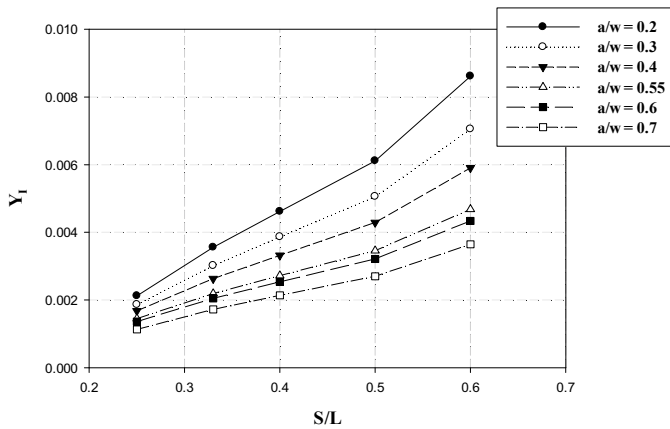

Fig. 6 Variations of Y_I for different crack length and *S/L* ratios in the mid-section of specimen
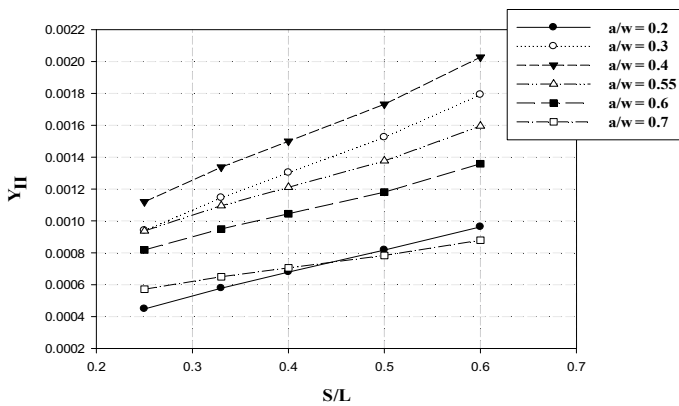

Fig. 7 Variations of Y_{II} for different crack length and *S/L* ratios in the mid-section of specimen
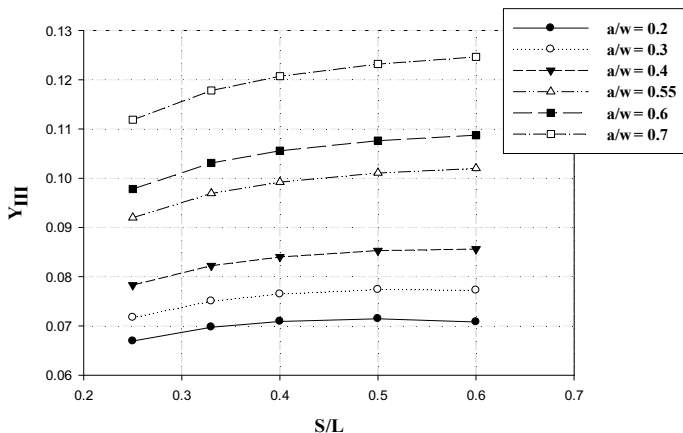
Fig. 8 Variations of Y_{III} for different crack length and *S/L* ratios in the mid-section of specimen

and with these geometry conditions the specimen is suitable for determining mode III fracture toughness of engineering materials, although there will be slight effects due to mode I loading conditions. The findings from the analysis also underscore that the acceptable range for the *S/L* ratio should not extend below *S/L* = 0.25. Put simply, when considering shorter distances, it becomes evident that the mode I stress intensity factor assumes negative values, indicative of a compressive loading state exerted upon the crack front. However, it's crucial for the mode I stress intensity factor to maintain a positive value, signifying the appropriate tension loading state. The outcomes of this study were exclusively confined to numerical analysis. Therefore, the suitability and applicability of the examined specimen ought to be corroborated through experimental and theoretical validation. This entails conducting a series of empirical tests and employing analytical prediction tools across a spectrum of resins and adhesives.

5 Conclusions

The anti-plane punch-through shear specimen was employed to derive distributions of normalized stress intensity factors under out-of-plane punch shear loading. The shear force and flexural bending distributions, along with the stress intensity factors extracted via the finite element method, revealed that despite the application of out-of-plane punching shear load to the specimen, the crack planes of the specimen experienced simultaneous tensile and shear deformation at the crack tip under specific conditions. For example, with a reduction in the longitudinal distance between the two crack planes (S) and an increase in the crack length (a), the influence of mode I was lessened in comparison to mode III. The most significant finding of this research
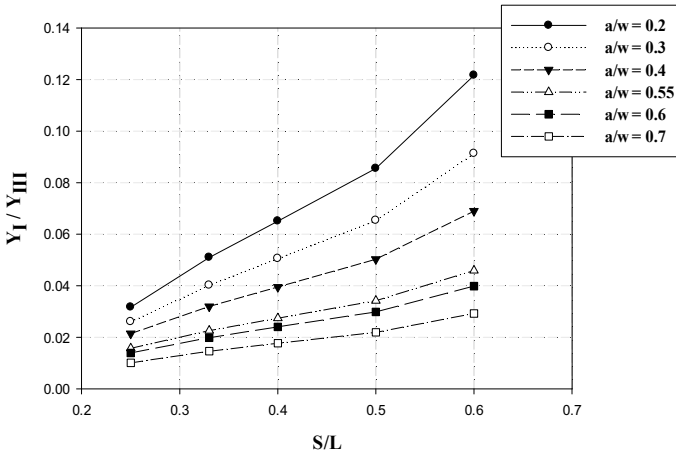
Fig. 9 Variations of Y_I / Y_{III} for different crack length and S/L ratios in the mid-section of specimen

suggests that the anti-plane punch-through shear specimen cannot exclusively induce pure mode III deformations at the crack tip.

References

1. Wei, M.D., Dai, F., Zhou, J.W., Liu, Y., Luo, J.: A further improved maximum tangential stress criterion for assessing mode I fracture of rocks considering non-singular stress terms of the Williams expansion. Rock Mech. Rock Eng. **51**, 3471–3488 (2018). https://doi.org/10.1007/S00603-018-1524-Z/METRICS
2. Ayatollahi, M.R., Torabi, A.R.: Brittle fracture in rounded-tip V-shaped notches. Mater. Des. **31**, 60–67 (2010). https://doi.org/10.1016/J.MATDES.2009.07.017
3. Yue, Z., Peng, L., Qiao, Y., Liu, W., Xu, S., Yuan, Y.: Dynamic brittle fracture in sharp V-notched rock specimens using digital image correlation method. Theor. Appl. Fract. Mech. **119**, 103323 (2022). https://doi.org/10.1016/J.TAFMEC.2022.103323
4. Torabi, A.R., Fakoor, M., Pirhadi, E.: Tensile fracture in coarse-grained polycrystalline graphite weakened by a U-shaped notch. Eng. Fract. Mech. (2013). https://doi.org/10.1016/j.engfracmech.2013.08.015
5. Akhavan-Safar, A., Ayatollahi, M.R., Safaei, S., da Silva, L.F.M.: Mixed mode I/III fracture behavior of adhesive joints. Int. J. Solids Struct. **199**, 109–119 (2020). https://doi.org/10.1016/J.IJSOLSTR.2020.05.007
6. Ayatollahi, M.R., Aliha, M.R.M., Saghafi, H.: An improved semi-circular bend specimen for investigating mixed mode brittle fracture. Eng. Fract. Mech. **78**, 110–123 (2011). https://doi.org/10.1016/J.ENGFRACMECH.2010.10.001
7. Bidadi, J., Saeidi Googarchin, H., Akhavan-Safar, A., da Silva, L.F.M.: Loading rate effects on mixed-mode I/II fracture envelope of epoxy resins with nonlinear behavior. Theor. Appl. Fract. Mech. **125**, 103858 (2023). https://doi.org/10.1016/J.TAFMEC.2023.103858
8. Aliha, M.R.M., Ayatollahi, M.R.: Geometry effects on fracture behaviour of polymethyl methacrylate. Mater. Sci. Eng. A **527**, 526–530 (2010). https://doi.org/10.1016/J.MSEA.2009.08.055

9. Mousavi, S.S., Aliha, M.R.M., Imani, D.M.: On the use of edge cracked short bend beam specimen for PMMA fracture toughness testing under mixed-mode I/II. Polym. Test. **81**, 106199 (2020). https://doi.org/10.1016/J.POLYMERTESTING.2019.106199

10. Aliha, M.R.M., Samareh-Mousavi, S.S., Mirsayar, M.M.: Loading rate effect on mixed mode I/II brittle fracture behavior of PMMA using inclined cracked SBB specimen. Int. J. Solids Struct. **232** (2021). https://doi.org/10.1016/j.ijsolstr.2021.111177

11. Aliha, M.R.M., Ayatollahi, M.R.: Geometry effects on fracture behavior of polymethyl methaacrelate. Mater. Sci. Eng. A **527**, 526–530 (2010). https://doi.org/10.1016/j.msea.2009.08.055

12. Aliha, M.R.M., Hosseinpour, G.R., Ayatollahi, M.R.: Application of cracked triangular specimen subjected to three-point bending for investigating fracture behavior of rock materials. Rock Mech. Rock Eng. **46**, 1023–1034 (2013). https://doi.org/10.1007/S00603-012-0325-Z/METRICS

13. Aliha, M.R.M., Bahmani, A., Akhondi, S.: Determination of mode III fracture toughness for different materials using a new designed test configuration. Mater. Des. **86**, 863–871 (2015). https://doi.org/10.1016/J.MATDES.2015.08.033

14. Safaei, S., Ayatollahi, M.R., Saboori, B.: Fracture behavior of GPPS brittle polymer under mixed mode I/III loading. Theor. Appl. Fract. Mech. **91**, 103–115 (2017). https://doi.org/10.1016/j.tafmec.2017.04.017

15. Saboori, B., Ayatollahi, M.R.: Experimental fracture study of MWCNT/epoxy nanocomposites under the combined out-of-plane shear and tensile loading. Polym. Test. **59**, 193–202 (2017). https://doi.org/10.1016/J.POLYMERTESTING.2017.01.028

16. Bidadi, J., Aliha, M.R.M., Akbardoost, J.: Development of maximum tangential strain (MTSN) criterion for prediction of mixed-mode I/III brittle fracture. Int. J. Solids Struct. **256**, 111979 (2022). https://doi.org/10.1016/j.ijsolstr.2022.111979

17. Bidadi, J., Akbardoost, J., Aliha, M.R.M.: Thickness effect on the mode III fracture resistance and fracture path of rock using ENDB specimens. Fatigue Fract. Eng. Mater. Struct. **43**, 277–291 (2020)

18. Karami, J., Ayatollahi, M.R., Saboori, B.: Fracture study of MWCNT/epoxy nanocomposite under pure mode III loading using anti-symmetric four-point bend specimen. Mater. Des. Process. Commun. **1**, e77 (2019). https://doi.org/10.1002/MDP2.77

19. Backers, T., Stephansson, O., Rybacki, E.: Rock fracture toughness testing in mode II—punch-through shear test. Int. J. Rock Mech. Min. Sci. **39**, 755–769 (2002). https://doi.org/10.1016/S1365-1609(02)00066-7

20. Davies, J.: Numerical study of punch-through shear specimen in mode II testing for cementitious materials. Int. J. Cem. Compos. Light. Concr. **10**, 3–14 (1988). https://doi.org/10.1016/0262-5075(88)90017-6

21. Davies, J., Yim, C.W.A., Morgan, T.G.: Determination of fracture parameters of a punch-through shear specimen. Int. J. Cem. Compos. Light. Concr. **9**, 33–41 (1987). https://doi.org/10.1016/0262-5075(87)90035-2

22. Rao, Q., Liao, Z.: Rock fracture under anti-plane shear (mode III) loading. J. Cent. South Univ. Technol. **121**(12), 125–128 (2005). https://doi.org/10.1007/S11771-005-0385-2

Durability of Structural Adhesive Joints

Silicone Pressure-Sensitive Adhesives Modified with Halloysite of Increased Thermal Resistance

Adrian Krzysztof Antosik, Karolina Mozelweska, Marlena Musik, and Piotr Miądlicki

Abstract The objective of this study was to produce single-sided tapes with varying ccentrations of halloisyte and assess their impact on the self-adhesive properties of commercial adhesives. Key self-adhesive properties, including tack, peel adhesion, shear strength, shrinkage, and thermal resistance, were thoroughly examined. The silicone-based PSA tapes with halloysite additives hold potential applications in heavy industries for joining components operating under high temperatures, as well as in aerospace for bonding solar cells on satellites and space stations. Although there are limited reports on one-sided adhesive tapes incorporating silicones and halloysite, considering their wide range of potential uses, we conducted self-adhesive tests to elucidate the influence of halloysite on these properties. Additionally, we investigated the reactivity between the crosslinking compound and silicone adhesive during the crosslinking process, along with the thermal effects associated with this process. Given the diverse applications of the resulting tapes, we also conducted flammability and heat of combustion tests in accordance with relevant standards. As a result of these tests, we successfully developed one-sided self-adhesive tapes with enhanced properties, such as improved temperature resistance, reduced shrinkage, and increased resistance to flammability.

Keywords Halloysite · Cohesion · Pressure-sensitive adhesives · Adhesion

A. K. Antosik (✉) · K. Mozelweska · M. Musik
Faculty of Chemical Technology and Engineering, Department of Chemical Organic Technology and Polymeric Materials, West Pomeranian University of Technology in Szczecin, Pulaskiego 10, 70-322 Szczecin, Poland
e-mail: adriankrzysztofantosik@gmail.com

P. Miądlicki
Engineering of Catalytic and Sorbent Materials Department, Faculty of Chemical Technology and Engineering, West Pomeranian University of Technology in Szczecin, Pulaskiego 10, 70-322 Szczecin, Poland

1   Introduction

Adhesives, i.e. substances used to connect different materials, have been used by people for centuries. The first adhesives were based on natural substances such as resin, wax, or flour. In ancient times, it was used as an adhesive. milk, eggs, flour, jewels, but also tar, tree resins or natural Arabic gum. In ancient Egypt, glue was used to join ceramics together, as well as to create terrazzo, used to decorate walls and floors. In the Middle Ages, adhesives based on animal skins and bones, such as gelatin, began to be used. These adhesives were used, among others, in for gluing books and as a binder for wood. In the eighteenth and nineteenth centuries, new types of adhesive appeared, including starch adhesives, casein adhesives, as well as synthetic adhesives, such as rubber and formaldehyde resin adhesives. The twentieth century saw further development of synthetic adhesives, including epoxy, cyanoacrylate, and polyurethane adhesives. Today, adhesives are widely used in various industries, from furniture to automotive and aerospace industries [1–3].

Pressure-sensitive adhesives are a type of adhesives that contain a self-adhesive layer on one or both sides, so they can stick to a variety of surfaces without the need for additional adhesive application tools. Pressure-sensitive adhesives are very popular due to their convenience and ease of use. They can be used to glue paper, plastic, wood, fabrics, metals, and other materials. There are many different types of pressure-sensitive adhesives, which differ in strength, thickness, flexibility and durability, among other things. When choosing the right adhesive, consider the type of surface the adhesive will be used on and the conditions in which the product will be used [4–6].

Silicone-based pressure-sensitive adhesives are commonly used to bond a variety of materials, including glass, metal, plastic, and wood. Silicones are a type of elastomers obtained using condensation or addition polymerization, in which one of the main components is silicon [7].

Silicone-based adhesives have many advantages, including:

- Durability: Silicone pressure-sensitive adhesives have very good mechanical strength, so they can be used in harsh conditions, including high temperatures and humidity.
- Resistance to external factors: Silicone adhesives are resistant to weather conditions such as UV radiation, humidity, acidity and alkalinity, which makes them used in many applications, including automotive, construction and electronics industries.
- Flexibility: Silicone-based adhesives are highly flexible, allowing stress to be evenly distributed in the joint and reducing the risk of cracking and damage.
- Ease of application: Silicone adhesives are easy to apply and can be used on a variety of surfaces, including uneven and porous surfaces [8].

Silicone pressure-sensitive adhesives are very versatile and widely used in many areas, such as:

– Electronic industry—silicone adhesives are used to seal and isolate electronic components and circuits from moisture, dust and vibration.
– Automotive industry—silicone adhesives are used in the automotive industry to seal engines, gearboxes and other vehicle components.
– Construction industry—silicone adhesives are used to seal windows, doors, bathrooms and other building elements against moisture, dust and wind.
– Food industry—silicone adhesives are used in the food industry to produce molds for making sweets and other food products.
– Medical industry—silicone adhesives are used in medicine for the production of surgical instruments and medical implants.
– Cosmetic industry—silicone adhesives are used in the production of cosmetics for sealing and gluing packaging elements.
– Textile industry—silicone adhesives are used in the textile industry to glue fabrics and leather.
– Chemical industry—silicone adhesives are used in the chemical industry to produce adhesives, sealants and other chemical products [9].

Overall, silicone pressure-sensitive adhesives are a very versatile product that finds applications in many industries and other areas of everyday life [10].

Halloysite (or halloysite) is a rare mineral from the group of silicates, which contains, among others, boron, aluminum, iron, magnesium and lithium. The name comes from the Greek word "halos", meaning salt, and refers to the mineral's distinctive appearance, which often has white or light gray crystals with clear outlines [10].

Halloysite is mainly found in metamorphic rocks such as shales, marbles and gneisses, and in pegmatites and granites. It is a relatively rare mineral and does not have much economic importance, however, due to its unusual chemical composition, it is a valuable object of scientific research [11].

Halloysite belongs to the group of cyclosilicate minerals and has characteristic physical properties, such as pleochroism (i.e. color change of the crystal depending on the direction of observation) and anisotropy (i.e. changeability of physical properties in different directions). Due to its unique properties and chemical composition, halloysite is often studied by scientists involved in geology, mineralogy and chemistry. Halloysite is a natural mineral from the kaolin group, composed of tubular nanotube-shaped structures that form cylindrical channels with a diameter of 30–70 nm. Due to its microstructure, halloysite is used as a filler for adhesives to improve their mechanical and rheological properties [12].

Adding halloysite to the adhesive increases its viscosity and stability, which leads to better adhesion to the substrate. In addition, halloysite can increase the mechanical strength of the adhesive, which is particularly important in industrial applications. Thanks to its microscopic structure, halloysite has the ability to fill spaces in adhesives and resins, which increases their strength and impact resistance. It is also used in the production of insulating materials and composites where its mechanical properties are also used. Halloysite is used not only in the adhesive industry but also in the production of paints, cosmetics, insulating materials and in the field of biomedicine.

It is worth noting that halloysite is a rare and expensive mineral, which means that its use is usually limited to more advanced technological and industrial applications [13, 14].

Research on the influence of halloysites on the self-adhesive properties of silicone adhesives is important for the development of adhesive materials with diverse parameters. In the context of the presented discussion, it is worth noting several key points:

– Types of Halloysites: Research focusing on different types of halloysites helps understand how different crystal structures and mineral properties affect the self-adhesion of silicone adhesives. Differences in crystal structure, chemical composition, and surface morphology can lead to varied effects in terms of adhesion.
– Halloysite Particle Thickness: Studies on the influence of halloysite particle thickness are significant because they can reveal whether particle size matters for self-adhesion. Thicker or thinner layers of halloysites can impact surface texture and chemical properties, which, in turn, affect adhesion.
– Halloysite Manufacturer: Various manufacturers may offer halloysites with different parameters, such as purity, particle size, or degree of impregnation. Comparing different sources of halloysites can help determine which ones are more suitable for specific applications.
– Self-Adhesive Properties: Self-adhesive properties of silicone adhesives include parameters like tack, adhesion, cohesion, and flexibility. Research on the influence of halloysites on these parameters helps understand how mineral additives affect a adhesive's ability to adhere to surfaces and its overall durability.
– Practical Applications: These studies are essential for tailoring silicone adhesives to various applications. For example, if specific halloysites are found to improve adhesion at low temperatures, they may be more suitable for cold applications. Understanding the influence of halloysites can lead to more optimized adhesive products.

In summary, research on the impact of halloysites on silicone adhesives is a crucial step in the development of new adhesive materials with enhanced properties. The results obtained can significantly influence the design of adhesive materials to better meet specific requirements in various applications.

2   Materials

In work commercial silicone adhesive was used (acronym: Q2-7358), which was the product of Dow Corning (USA). Dichlorobenzoyl peroxide (DClBPO) was used as a crosslinking agent. The halloysites were from different companies (Table 1).

Table 1 Based properties of used halloysite fillers

Acronym	Producent	Size	Colour	Other information
H1	Certech	0.4–1.0 mm	*Fawn*	Dried
H2	Certech	0–1.0 mm	*Brass*	Dried
H3	Certech	0–0.056 mm	*Nutty*	Dried, ground
H4	Certech	0–0.2 mm	*Khaki*	Dried, ground
H5	Dunnino	N/A	*Venetian roses*	Dried, ground, manufacturer's designation ICO-30
H6	Dunnino	N/A	*Fleshy*	dried, ground, Manufacturer's designation PJF
H7	Sigma Aldrich	N/A	*White*	Dried, ground

2.1 Preparation of One-Side Self-Adhesives Tape

The Q2-7356 silicone pressure-sensitive adhesive (manufactured by Dow Corning) and a crosslinking agent (2,4-dichlorobenzoyl peroxide at 1.5 wt.% based on polymer content) were blended together to create a homogeneous organic composition with 50 wt.% polymer [27]. To form a uniform mixture, the selected silicone pressure-sensitive adhesive composition with the crosslinking agent was combined with halloysite. The filler content was varied at 0.1, 0.5. 1.0 and 3.0 wt.% based on polymer content, ensuring that the viscosity limit for effective mixing was not exceeded. Subsequently, the pressure-sensitive adhesive (PSA) was coated onto a 50 μm polyester film at a speed of 5 cm/s, with an approximate coating weight of 45 g/m^2. The coated films were then dried for 10 min at 110 °C in a drying canal. To secure the adhesive films, a 36 μm polyester film was applied on top. The resulting self-adhesive tapes were subjected to testing following international standards. The samples for the adhesive tape containing halloysite strips were prepared in the same manner.

3 Methods

The FTIR spectra were made using a Nicolet 380 spectrometer from Thermo Electron Corporation (Waltham, MA, USA). The study used the ATR attachment with a diamond crystal. The measurement range was from 4000–400 cm^{-1} at a resolution of 4 cm^{-1}.

The XRD of the halloysites were obtained by an Empyrean PANalytical X-ray diffractometer (Malvern, UK) with a Cu lamp used as the radiation source in the 2θ 6–80° range with a step size of 0.026.

Peel Adhesion Testing refers to a method used to assess the bonding strength of a pressure-sensitive adhesive. This test is crucial in evaluating the effectiveness of adhesive materials. It examines how well the surfaces of different layers or physical

bodies adhere to each other, enabling the transfer of loads between them. The results of this test are influenced by the attractive forces acting on the contact surface of the bonded materials [14].

Tack, or stickiness or stickiness, is an important property of pressure-sensitive adhesives. It means the ability of the adhesive to create a permanent bond on the surface when it is briefly exposed to contact. Tack determines the ease with which the adhesive can adhere to a variety of materials and form an initial hold. The higher the tack level, the faster and stronger the bond formation. In practice, high tack adhesives will have a greater ability to grip surfaces and hold them in place, which can be important in applications such as labeling, assembly, and sticking tapes [15].

Cohesion plays a vital role in determining the strength of adhesive bonds. Alongside adhesion, it is regarded as one of the key properties for both self-adhesive tapes and adhesives. Several factors impact the cohesion value, including test temperature, concentration, type of cross-linking compounds, and the thickness of the adhesive film. The FINAT FTM 8 method is employed to determine the cohesion property. The measurement is conducted at both room temperature and elevated temperature (70 °C) to assess the adhesive's performance under different thermal conditions [16].

The SAFT (Shear Adhesion Failure Temperature) test was conducted in a similar manner to the cohesion test, with one key difference: the temperature was not kept constant. Instead, it was gradually raised from 20 to 225 °C, with an increment of 1.5 °C per minute. Throughout the test, the temperature at which the tape sample detached from the plate was recorded [17].

The measurement of shrinkage in pressure-sensitive adhesives involves observing the reduction in the size of the adhesive film compared to its original dimensions. Shrinkage is influenced by the crosslinking process, including the specific method and compound used for crosslinking. This property is significant as shrinkage can impact the adhesive surface and lead to deformations. In the context of pressure-sensitive adhesives, shrinkage refers to the change in the size of the adhesive film and is typically reported as a percentage or in millimeters. The adhesive film is typically transferred onto a PVC (polyvinyl chloride) or PET (poly(ethyl terephthalate)) film, which is then adhered to a metal plate. Two cuts are made in the film and exposed to a temperature of 70 °C. After a specified duration, the size of the cuts is examined, and the test result is determined as the average of eight measurements. In PSA technology, a shrinkage value exceeding 0.5 mm or 0.5% is considered beyond the acceptable limit [18].

4   Results and Discussion

The FT-IR spectras of halloysite samples are presented in Fig. 1 and Table 2.

Figure 2 shows the XRD patterns of the halloysite samples. The characteristic peaks of halloysite, according to JCPDS card 29–1487 are shown in the plot. The diffraction peaks at $2\theta = 12.0, 20.1, 24.6, 35.0, 37.9, 54.5$ and 62.6 corresponded
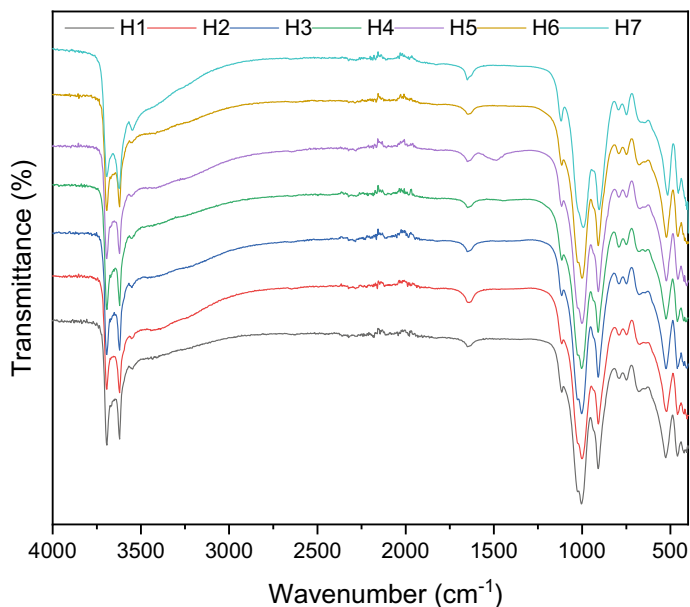
Fig. 1 The FT-IR spectra of halloysite samples

Table 2 Characteristic peaks of halloysite

Wavelength (cm^{-1})	Assignment
3694, 3621	–OH stretching vibrations
1630	H_2O bending vibrations
1115	Si–O stretching vibrations
1040–950	Si–O–Si stretching vibrations
900	Al–O–H bending vibrations
789, 754	–OH translation vibrations
530	Si–O–Al bending vibrations
453	Si–O–Si bending vibrations

to (001), (100), (002), (110), (003), (210) and (300) planes, respectively [https://doi.org/10.3390/nano10091834]. All tested samples are of high purity, they differ slightly in a small amount of impurities consists of quartz, illite and kaolin.

The silicone pressure-sensitive adhesive composition without filler exhibit a relative good values of useful properties such as adhesion and tack (Table 2). On the other hand the values of cohesion at room and elevent temperature was on high level. At the same time, tapes based on an unmodified composition show relatively low thermal resistance (in the SAFT test), which limits the number of possible applications in industry (Table 3).
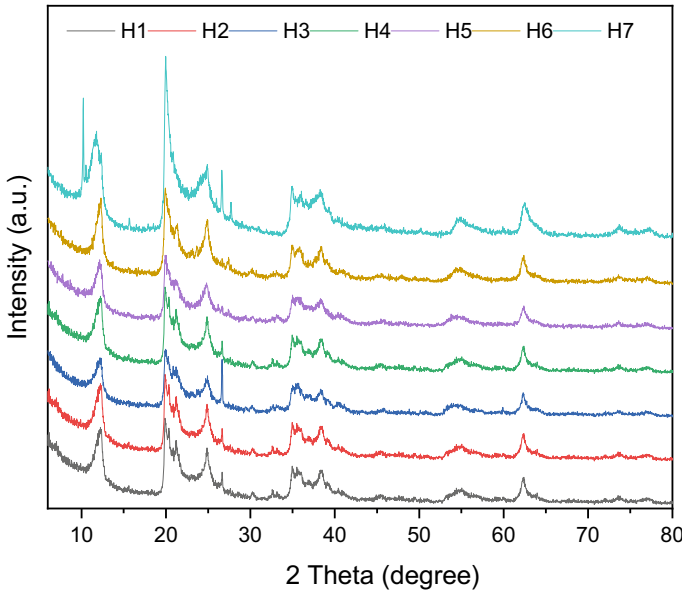
Fig. 2 The XRD patterns of the halloysite samples

Table 3 Based properties of the base silicon pressure-sensitive adhesives without fillers

Resin acronym			Q2-7358		
Cohesion (h)		Tack (N)	Adhesion (N/25 mm)	SAFT (°C)	Viscosity (Pa·s)
20 °C	70 °C				
>72	>72	6.9	10.2	147	16.7

Table 4 presents the viscosity outcomes for the adhesive formulations following the incorporation of halloysite. In all cases, there is a notable rise in viscosity when compared to the base adhesive. The halloysite-modified adhesives, particularly those labeled as H1 and H3, exhibited the longest processing times for adhesive tape production. Conversely, the remaining adhesive compositions are conducive to coating within a relatively short timeframe, typically up to 3 days. Beyond this duration, these adhesive formulations become impractical for use.

The variations in viscosity are an essential consideration in adhesive production. While increased viscosity can offer benefits such as improved adhesion and reduced dripping during application, excessively high viscosity can pose challenges in terms of ease of processing and application. Therefore, the choice of adhesive formulation should be made based on the specific requirements of the intended application, balancing factors like viscosity, drying time, and adhesive performance.

Table 4 Influence on halloysite high content on Si-PSA composition viscosity

Filler acronym	Viscosity (Pas)				
	1 day	2 days	3 days	5 days	7 days
H1	41.8	44.2	46.0	55.8	64.7
H2	42.7	47.2	54.0	72.4	Gel
H3	35.5	37.6	38.6	47.1	60.3
H4	45.4	50.1	50.6	Gel	Gel
H5	46.5	49.2	48.0	Gel	Gel
H6	44.6	47.8	50.0	Gel	Gel
H7	45.3	48.7	49.0	Gel	Gel

Figure 3 illustrates the adhesion characteristics of pressure-sensitive adhesives that have been subject to modification with halloysite. Overall, the adhesives exhibit satisfactory properties. Interestingly, the adhesion results reveal a noteworthy trend: the adhesive samples with the lowest filler content consistently demonstrate the highest adhesion values. Conversely, as the quantity of filler increases, there is generally a decrease in adhesion performance.

Specifically, the adhesive formulations modified with H4, H2, and H1 halloysite variants exhibit the lowest adhesion values, with the most significant reduction in adhesion being observed within the filler content range of 0.1 to 0.5 wt%. In contrast,
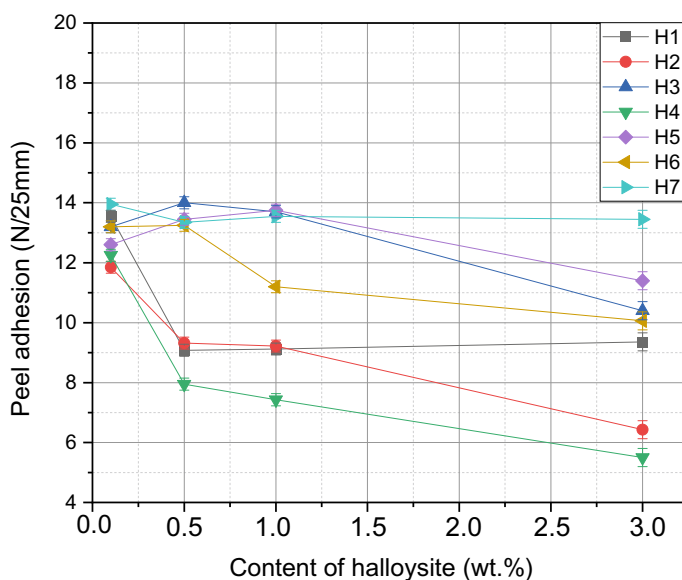
Fig. 3 Influence on halloysite addition on Si-PSA tape peel adhesion

the composition containing halloysite H6 displays intermediate adhesion properties, falling between the ranges observed for the various types of halloysites.

The most promising results are evident in adhesive samples incorporating H5, H3, and H7. Notably, the tack values for adhesive compositions modified with H5 and H3 consistently fall within the range of 1.0 to 3.0 wt.%. Intriguingly, samples incorporating halloysite H7 exhibit relatively consistent adhesion values regardless of the filler content.

These findings underscore the complex interplay between filler type, quantity, and adhesive performance. The choice of halloysite variant and its optimal loading concentration can significantly impact the adhesive's adhesion characteristics. It is essential to consider these factors when tailoring adhesive formulations for specific applications, aiming to strike the right balance between adhesion strength and other desirable properties.

The trend observed in adhesion results is mirrored in the tack measurements as well. Generally, the tack value tends to decrease as the quantity of filler in the adhesive increases. However, it's important to note an interesting exception—the sample modified with halloysite H7 demonstrates an increase in tack value as the filler content rises.

Conversely, the compositions modified with halloysite variants H4, H2, and H1 consistently yield the lowest tack results. In fact, the values obtained for the H4 samples are deemed unacceptable due to their exceptionally low levels. If these compositions were to be utilized, it would be imperative to enhance their short-term tack by incorporating specific agents aimed at improving tack properties.

On the positive side, the most favorable tack results are achieved with samples containing halloysite H3, H5, and H7. These findings reinforce the intricate relationship between filler concentration and tack performance. It's evident that the choice of halloysite type plays a pivotal role in determining tack behavior, which further underscores the importance of meticulous formulation design to ensure the desired adhesive properties, especially in applications where tack is a critical factor (Fig. 4).

The cohesion results presented in Table 4 shed light on the adhesive performance of the self-adhesive tapes under different conditions, both at room temperature and elevated temperatures. These results provide valuable insights into the tape's ability to maintain its integrity and structural stability over time.

One notable observation is that the sample modified with halloysite H1 consistently exhibited the highest cohesion values across the entire concentration range, regardless of temperature conditions. This suggests that halloysite H1 has a positive impact on the internal strength of the adhesive matrix, making it resilient and capable of maintaining its cohesiveness even under elevated temperatures.

At room temperature (20 °C), other halloysite variants, namely H2, H4, and H5, also demonstrated noteworthy cohesion properties, indicating their potential suitability for applications where maintaining structural integrity at lower temperatures is crucial.

However, the scenario changes when the temperature is elevated. In this case, apart from the composition containing halloysite H2, the sample incorporating halloysite H4 displayed the highest cohesion properties. This shift in performance could be
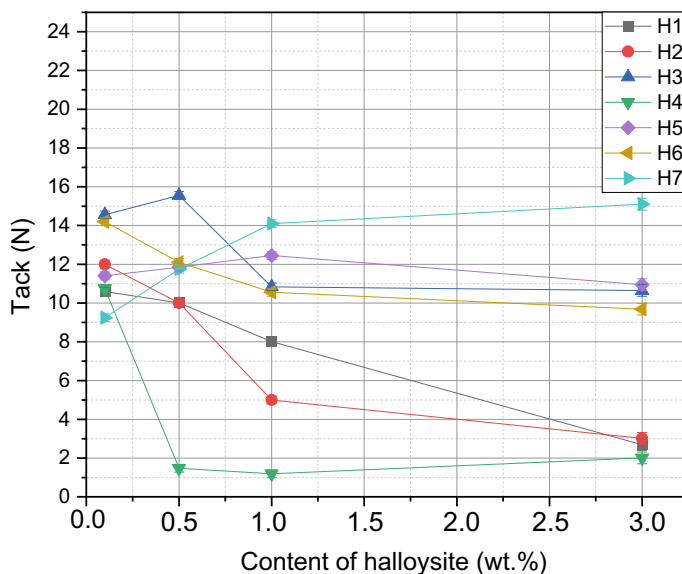
Fig. 4 Influence on halloysite addition on Si-PSA tape tack

attributed to the unique thermal characteristics of halloysite H4, which seem to enhance cohesion under elevated temperature conditions.

Conversely, the compositions modified with halloysite H7, known for their superior adhesion and tack properties, exhibited the poorest cohesion performance. This intriguing inverse relationship between cohesion and adhesion/tack could be attributed to excessive filler loading, potentially hindering the adhesive's ability to maintain its internal structural integrity.

It's worth noting that, in general, as the filler concentration increased, the cohesion tended to decrease. This trend suggests that there might be an optimal filler-to-adhesive ratio that maximizes cohesion while maintaining other critical adhesive properties. The exception here is the H4 sample, which exhibited low cohesion even at the lowest concentration. This could be linked to its low tack and adhesion values, which might lead to insufficient bonding to the adhered surface, thereby compromising its cohesive strength.

In practical terms, these cohesion findings underscore the importance of a balanced formulation approach. While enhancing adhesion and tack properties can be advantageous, it's equally crucial to consider cohesion to ensure the overall performance and reliability of self-adhesive tapes in various real-world applications.

Figure 5 provides insights into the maximum temperature values recorded during the SAFT (Shear Adhesion Failure Temperature) test for various adhesive compositions containing different concentrations of halloysite fillers. These results are crucial in assessing the thermal resistance of the adhesive tapes and their potential applications in environments with varying temperature conditions.
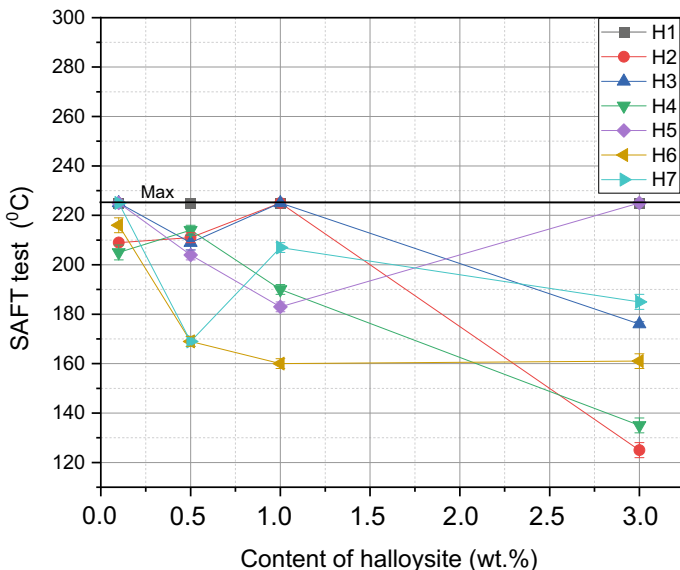
Fig. 5 SAFT test determining thermal resistance of silicone pressure-sensitive adhesives modificated by hallotsite with different filler content

For compositions modified with halloysite H2 and H3, the maximum temperature values were found to be at their highest for concentrations of 0.1 and 1.0 wt.%. This suggests that the addition of these specific halloysite variants at these concentrations enhances the adhesive's ability to withstand elevated temperatures. However, as the filler content increases to 3 wt.%, there is a noticeable decline in thermal resistance. This phenomenon may be attributed to the increasing concentration of filler particles, which might affect the overall heat dissipation within the adhesive matrix.

Interestingly, the compositions incorporating halloysite H5 and H6 exhibit a different trend. Here, the maximum temperature values tend to decrease as the filler content rises to 1 wt.%, indicating a potential negative impact on thermal resistance. However, for the 3 wt.% concentration, these values rebound and increase, with the H5-modified sample reaching the highest maximum temperature in the test. This behavior suggests that these specific halloysite variants may have a more complex interaction with the adhesive matrix, potentially involving changes in heat transfer mechanisms.

Conversely, the composition containing halloysite H4 consistently displays a decrease in maximum temperature values as the filler content increases. This phenomenon aligns with common industry practices, where the addition of excessive filler content can hinder thermal resistance. It's essential to strike a balance between filler content and other adhesive properties to optimize thermal performance.

These findings highlight the nuanced relationship between halloysite fillers and thermal resistance in adhesive compositions. The impact of different halloysite variants and their concentrations on thermal properties can vary significantly, necessitating careful consideration during formulation. Ultimately, understanding how halloysite additives influence thermal resistance is crucial for tailoring adhesive tape formulations to meet the specific temperature requirements of diverse applications.

Table 5 provides valuable insights into the shrinkage characteristics of pressure-sensitive adhesives, which is a critical parameter for various applications, particularly in the adhesive tape industry. The discussion below delves into the implications of the findings presented in the table:

The adhesive labeled "0" in Table 5 represents the base adhesive formulation without any silicone additives. This baseline adhesive exhibits significant shrinkage within a remarkably short time frame, surpassing the recommended limits for adhesives and self-adhesive tapes. For practical applications, it is essential that adhesive tapes maintain a shrinkage level below certain thresholds, typically defined as less than 0.5 mm or 0.5%.

The rapid and excessive shrinkage observed in the unmodified adhesive (labeled "0") highlights a critical challenge that must be addressed. Adhesive tapes with high levels of shrinkage are unsuitable for many applications, especially those where dimensional stability and consistent performance are paramount. These findings underscore the importance of seeking solutions to reduce shrinkage in adhesive formulations.

Fortunately, the introduction of silicone fillers, even in varying quantities, leads to a notable reduction in shrinkage when compared to the unmodified base adhesive. This is a significant and positive outcome of the study, as it suggests that the incorporation of silicone additives can effectively mitigate the undesirable shrinkage behavior observed in the base adhesive.

Reducing shrinkage is of utmost importance for adhesive tapes used in applications where precise fit, alignment, and dimensional stability are critical. Excessive

Table 5 Cohesion prepared silicon pressure-sensitive adhesives composition with different filler content

Filler acronym	Cohesion (h)							
	20 °C				70 °C			
Filler content (wt.%)	0.1	0.5	1.0	3.0	0.1	0.5	1.0	3.0
H1	>72	>72	>72	>72	>72	>72	>72	>72
H2	>72	>72	>72	>72	>72	>72	0.4	0.1
H3	>72	>72	>72	12.5	>72	>72	>72	0.5
H4	>72	>72	>72	>72	8.7	>72	>72	>72
H5	>72	>72	>72	>72	>72	>72	>72	1.5
H6	>72	>72	>72	10.3	>72	>72	10.5	0.5
H7	>72	53.4	24.1	23.6	>72	8.0	7.8	6.3

shrinkage can lead to problems such as warping, misalignment, and reduced bond strength, all of which can compromise the overall effectiveness of the adhesive tape.

In practical terms, the reduction in shrinkage achieved through the addition of silicone fillers broadens the potential applications of these adhesive tapes. Industries and applications that demand dimensional stability, such as electronics, construction, and automotive manufacturing, can benefit significantly from adhesive tapes with improved shrinkage characteristics.

In summary, the data presented in Table 6 underscores the importance of addressing shrinkage in adhesive tape formulations. The introduction of silicone additives has proven to be an effective strategy for reducing shrinkage, making these modified adhesive tapes more versatile and suitable for a broader range of applications where dimensional stability is a critical requirement.

5   Conclusion

The comprehensive tests conducted to investigate the influence of different halloysite types on self-adhesive adhesive performance have yielded valuable insights and practical outcomes. This research has implications for various industries where adhesive tapes play a pivotal role. In summary, the key findings and their significance are highlighted below:

Enhanced Thermal Resistance: One of the notable achievements of this research is the substantial improvement in the thermal resistance of the adhesive, with temperatures reaching as high as 225 °C. This outcome has far-reaching implications, particularly in applications where exposure to high temperatures is a common occurrence. The ability to withstand such elevated temperatures expands the potential applications of these adhesive tapes into industries where heat resistance is critical, such as automotive, aerospace, and electronics.

Mitigation of Shrinkage: Shrinkage is a common challenge in adhesive formulations, and it can have detrimental effects on applications that require dimensional stability. The study demonstrated that the addition of halloysite fillers effectively reduces shrinkage values, bringing them well below the industry-accepted threshold of 0.5%. This result is of paramount importance, as it ensures that adhesive tapes maintain their integrity, alignment, and bonding strength over time. Industries demanding precision and consistency in their adhesive applications, such as construction and electronics, stand to benefit significantly from this development.

High-Quality Adhesive Tapes: The research has culminated in the production of high-quality adhesive tapes. Among the various compositions tested, those containing H1 halloysite emerged as the most promising. These formulations strike an optimal balance between cohesion and adhesion, two essential properties for adhesive performance. Even at low concentrations, H1 substantially improves the thermal resistance of the adhesive, making it a valuable addition to adhesive formulations.

In conclusion, the findings of this research hold substantial promise for the adhesive industry. The ability to enhance thermal resistance and reduce shrinkage,

Table 6 Shrinkage of silicone pressure-sensitive adhesives modificated by hallotsite with different filler content

Filler content (% wt)	Shrinkage (%)											
	10 min	30 min	1 h	3 h	8 h	24 h	2 dni	3 dni	4 dni	5 dni	6 dni	7 dni
Pure												
0.0	0.41	0.42	0.64	0.90	1.14	1.33	1.33	1.33	1.33	1.33	1.33	1.33
H1												
0.1	0.12	0.20	0.22	0.31	0.40	0.50	0.52	0.54	0.56	0.56	0.56	0.56
0.5	0.11	0.13	0.14	0.16	0.18	0.21	0.23	0.24	0.27	0.30	0.30	0.30
1.0	0.08	0.11	0.12	0.13	0.14	0.16	0.17	0.17	0.19	0.20	0.25	0.25
3.0	0.09	0.10	0.11	0.12	0.13	0.15	0.16	0.18	0.20	0.21	0.24	0.24
H2												
0.1	0.03	0.03	0.04	0.10	0.13	0.13	0.13	0.13	0.13	0.13	0.13	0.13
0.5	0.12	0.17	0.2	0.25	0.27	0.30	0.33	0.37	0.42	0.47	0.50	0.50
1.0	0.06	0.10	0.19	0.24	0.36	0.41	0.44	0.46	0.47	0.49	0.49	0.51
3.0	0.10	0.11	0.12	0.14	0.15	0.17	0.18	0.20	0.22	0.24	0.25	0.25
H3												
0.1	0.14	0.19	0.21	0.30	0.32	0.39	0.40	0.42	0.44	0.46	0.50	0.50
0.5	0.10	0.18	0.21	0.25	0.28	0.31	0.35	0.36	0.39	0.40	0.43	0.43
1.0	0.14	0.16	0.18	0.20	0.22	0.25	0.27	0.30	0.34	0.35	0.36	0.36
3.0	0.10	0.11	0.12	0.13	0.14	0.16	0.17	0.18	0.20	0.23	0.25	0.25
H4												
0.1	0.10	0.14	0.17	0.25	0.36	0.41	0.41	0.43	0.45	0.48	0.50	0.450
0.5	0.10	0.12	0.16	0.17	0.24	0.27	0.32	0.37	0.40	0.42	0.42	0.42
1.0	0.09	0.12	0.17	0.22	0.25	0.27	0.30	0.33	0.35	0.38	0.40	0.40
3.0	0.11	0.15	0.17	0.20	0.22	0.25	0.27	0.30	0.32	0.35	0.37	0.37
H5												
0.1	0.18	0.24	0.28	0.31	0.35	0.42	0.47	0.51	0.56	0.6	0.64	0.64
0.5	0.17	0.20	0.27	0.32	0.40	0.48	0.52	0.61	0.71	0.74	0.80	0.80
1.0	0.10	0.19	0.24	0.35	0.37	0.43	0.45	0.49	0.51	0.53	0.55	0.55
3.0	0.07	0.09	0.10	0.11	0.15	0.16	0.17	0.19	0.21	0.21	0.21	0.21
H6												
0.1	0.10	0.16	0.36	0.42	0.47	0.59	0.60	0.61	0.63	0.63	0.66	0.70
0.5	0.06	0.09	0.14	0.25	0.29	0.37	0.39	0.44	0.49	0.54	0.59	0.64
1.0	0.09	0.15	0.21	0.35	0.37	0.44	0.45	0.47	0.50	0.50	0.50	0.50
3.0	0.12	0.17	0.24	0.27	0.30	0.34	0.37	0.40	0.44	0.46	0.46	0.46
H7												
0.1	0.15	0.22	0.27	0.32	0.37	0.42	0.48	0.51	0.57	0.61	0.65	0.69
0.5	0.10	0.11	0.20	0.29	0.35	0.43	0.55	0.57	0.59	0.64	0.65	0.68

(continued)

Table 6 (continued)

Filler content (% wt)	Shrinkage (%)											
	10 min	30 min	1 h	3 h	8 h	24 h	2 dni	3 dni	4 dni	5 dni	6 dni	7 dni
1.0	0.09	0.14	0.21	0.25	0.26	0.36	0.37	0.39	0.42	0.44	0.46	0.48
3.0	0.14	0.17	0.20	0.24	0.25	0.30	0.32	0.34	0.36	0.37	0.40	0.40

combined with the development of high-quality adhesive tapes, signifies a significant advancement in adhesive technology. These outcomes open doors to a wide range of applications, offering improved performance and reliability in sectors where adhesives are critical components. This research serves as a testament to the ongoing pursuit of innovation in adhesive materials, ultimately benefiting numerous industries and applications worldwide.

Supplementary Materials: not applicable.

6 Data Availability Statement

Not applicable.

7 Conflicts of Interest

The authors declare no conflict of interest.

References

1. Dunky, M.: Wood adhesives based on natural resources: a critical review Part I. Protein-based adhesives. Progress Adhes Adhes **6**(3), 199–332 (2020). https://doi.org/10.1002/978111984 6703.ch8

2. Cruz, B.A.S., Martinez, A.M.M. et al.: Evaluation of crosslinking reaction in adhesive based styrene-butadiene elastomers using infrared spectroscopy. In: Theophanides Theophile (ed.) Infrared Spectroscopy-Anharmonicity of Biomolecules, Crosslinking of Biopolymers, Food Quality and Medical Applications, pp. 117–137 (2015)
3. Mapari, S., Mestry, S., Mhaske, S.T.: Developments in pressure-sensitive adhesives: a review. Polym. Bull. **78**, 4075–4108 (2021). https://doi.org/10.1007/s00289-020-03305-1
4. Keimel, F.A.: Historical development of adhesives and adhesive bonding. In: Pizzi, A., Mittal, K.L. (ed.) Handbook of Adhesive Technology, pp. 10–21. Taylor & Francis Group, LLC, New York (2003)
5. Messler, R.W., Jr.: Joining composite materials and structures: some thought-provoking possibilities. J. Thermoplast. Compos. Mater. **17**(1), 51–75 (2004). https://doi.org/10.1177/0892705704033336
6. Yim, M.J., Li, Y., et al.: Review of recent advances in electrically conductive adhesive materials and technologies in electronic packaging. J. Adhes. Sci. Technol. **22**(14), 1593–1630 (2008). https://doi.org/10.1163/156856108X320519
7. Antosik, A.K., Mozelewska, K., Piątek-Hnat, M., et al.: Silicone pressure-sensitive adhesives with increased thermal resistance. J. Therm. Anal. Calorim. (2021). https://doi.org/10.1007/s10973-021-11048-y
8. Antosik, A.K., Mozelewska, K., Czech, Z., et al.: Influence of montmorillonite on the properties of silicone pressure-sensitive adhesives: preparation of a double-sided tape based on the best composition. SILICON **12**, 1887–1893 (2020). https://doi.org/10.1007/s12633-019-00295-2
9. Mecham, S., Sentman, A., Sambasivam, M.: Amphiphilic silicone copolymers for pressure sensitive adhesive applications. J. Appl. Polym. Sci. **116**(6), 3265–3270 (2010)
10. Tan, H.S., Pfister, W.R.: Pressure-sensitive adhesives for transdermal drug delivery systems. Pharm. Sci. Technol. Today **2**(2), 60–69 (1999)
11. Joussein, E., Petit, S., Churchman, J., Theng, B., Righi, D., Delvaux, B.J.C.M.: Halloysite clay minerals—a review. Clay Miner. **40**(4), 383–426 (2005)
12. Du, M., Guo, B., Jia, D.: Newly emerging applications of halloysite nanotubes: a review. Polym. Int. **59**(5), 574–582 (2010)
13. Yuan, P., Tan, D., Annabi-Bergaya, F.: Properties and applications of halloysite nanotubes: recent research advances and future prospects. Appl. Clay Sci. **112**, 75–93 (2015)
14. Rawtani, D., Agrawal, Y.K.: Multifarious applications of halloysite nanotubes: a review. Rev. Adv. Mater. Sci. **30**(3), 282–295 (2012)
15. Si, J., Li, Y., Yu, X.: Curing behavior and mechanical properties of an eco-friendly cold-mixed epoxy asphalt. Mater. Struct. **52**, 81 (2019). https://doi.org/10.1617/s11527-019-1382-5
16. O'Connor, A.E., Willenbacher, N.: The effect of molecular weight and temperature on tack properties of model polyisobutylenes. Int. J. Adhes. Adhes. **24**(4), 335–346 (2004). https://doi.org/10.1016/j.ijadhadh.2003.11.005
17. Baldan, A.: Adhesion phenomena in bonded joints. Int. J. Adhes. Adhes. **38**, 95–116 (2012). https://doi.org/10.1016/j.ijadhadh.2012.04.007
18. Feldstein, M.M., Kireeva, P.E., Kiseleva, T.I., et al.: A new class of pressure-sensitive adhesives based on interpolymer and polymer-oligomer complexes. Polym. Sci. Ser. A **51**(7), 799–814 (2009). https://doi.org/10.1134/S0965545X09070074

SPECSIL – Silicone Pressure-Sensitive Adhesives Exhibit Increased Thermal–Mechanical Properties

Adrian Krzysztof Antosik, Edyta Kucharska, and Karolina Mozelewska

Abstract New self-adhesive tapes based on AGLEV®SI 200 (AG) modified silicone resins has been studied. This study was aimed to find effective methods for AG modification using a coupling agents, and 3-aminopropyltriethoxysilane (APTES). Results revealed that the amine groups from the APTES were effectively loaded and evenly spread on the surface of the AGLEV®SI 200 fibers. The described technique of modifying AG enables an increase in the chemical compatibility of this mineral with certain resins for use in pressure-sensitive heat-resistant silicone adhesives. By loading modified AG, it was possible to considerably increase the temperature resistance of novel self-adhesive materials while retaining their excellent self-adhesive characteristics. The composition comprising 0.5 wt% of modified AG (AG-0.5APTES), which exhibits a thermal resistance above 225 ℃, demonstrated the best characteristics. Additionally, this composition-maintained cohesiveness at both room and increased temperatures for more than 72 h, stable shrinkage for 0.46%, adhesion for 11 N/25 mm, and tack for 39 N, respectively.

Keywords AGLEV®SI 200 · Modifying · Surface characteristics · Silicone pressure-sensitive adhesives

1 Introduction

Silicone pressure-sensitive adhesives (Si-PSA) are recognized to be materials for specialized applications. It has to do with the particular chemical structure of Si-PSAs, which tend to have very flexible Si–O–Si linkages but lack functional groups. They mostly comprise of silicone resins like MQ resins and silicone polymers with silane functionality. As a consequence, these adhesives display strong chemical

A. K. Antosik (✉) · E. Kucharska · K. Mozelewska
Department of Chemical Organic Technology and Polymeric Materials, Faculty of Chemical Technology and Engineering, West Pomeranian University of Technology, 70322 Szczecin, Poland
e-mail: adrian.antosik@zut.edu.pl; adriankrzysztofantosik@gmail.com

resistance and environmental conditions like sun radiation or humidity. They also exhibit extremely good performance attributes (adhesion, cohesion, and tack), particularly for materials with low surface energy. Commercially available adhesive tapes based on Si-PSA compensate for variances in the thermal expansion of the attached materials and are resistant to dynamic stress, ensuring a long-lasting and affordable connection of materials. They also have a good initial adherence to most surfaces. They have been used in a variety of industries, including the medical field (they are found in self-adhesive patches as well as patches that deliver medications topically), the heavy and automotive sector (as a connector for components that must operate at high temperatures), and the electrical sector (as non-conductive tapes and masking tapes). Si-PSA is unusual, which has piqued scientists' curiosity in this category of adhesives during the last ten years. There are ever more efforts in the literature to acquire new items and change silicone pressure-sensitive adhesives [1–3].

Currently, in order to obtain the desired properties of Si-PSA-based self-adhesive materials, they are designed already at the stage of resin synthesis. Due to the aforementioned characteristics, cross-linking and other straightforward chemical changes are often utilized to improve silicone pressure-sensitive adhesives. It seems that one reasonably easy technique to improve the characteristics of Si-PSA based tapes is to change silicone materials by adding improved fillers to them. There are reports in the literature on the modification of silicone resins with silicon and carbon fillers in order to improve their thermal resistance and conductivity, respectively [4–6]. Moreover, the research shows that it is easier to carry out the chemical modification of the fillers than the modification of the resin itself; and the introduction of a suitable compatible filler additive (physical modification) into the resin allows for the production of modified materials.

AGLEV®SI 200 (AG) is a species of hydrated magnesium aluminum silicate non-metallic mineral, which is characterized by a porous crystalline structure containing tetrahedral layers alloyed together along longitudinal sideline chains. AG is an inexpensive and readily available minerals, due to its large specific surface area and high thermal stability, it finds many applications [7–11]. AG is classified as a member of the sepiolite family of minerals because of its comparable microscopic structure and appearance. As a result of its similar microscopic structure and external appearance, AG is categorized as a mineral belonging to the sepiolite family. The fibrous morphology, tiny particle size, and tunnels of AGLEV®SI 200 provide an abundance of specific surface area, with surface characteristics varied greatly across various AG deposits as a result of textural and microtextural aspects. The physical–chemical characteristics and, therefore, the applications of many materials of natural origin (including AG) are greatly influenced by their size, shape, and fiber arrangement. The properties of these materials depend on the following: the length of the fiber (as the specific surface area is small for the longest fibers due to the limited accessibility to the interior of the crystal), and the arrangements or textures of the fibers (as a very closed porosity produces a textural microporosity, whereas an open porosity produces meso- and microporosities that do not contribute to the specific surface area). Numerous industrial uses for AGLEV®SI 200 are directly connected to its

surface characteristics, which are a result of its textural and microtextural characteristics. Because of its physical and chemical characteristics, it is used in several industrial and commercial items, most often in adsorption applications. Its composition and texture result in a sizable adsorption capability. The tiny particle size, the channels in the structure, and the fibrous shape of AG give it an extremely high specific surface area. The material makes up a highly reactive component of soils and sediments [12–21]. Minerals such as palygorskite, attapulgite ABSO-PRO L-16, and attapulgite AGLEV®SI 200 are particularly attractive fillers because of their distinctive structure and significant textual qualities. These naturally porous materials that have been functionalized with coupling agents are widely used in environmental engineering. As a result of the functionalization, natural silicates develop surface functional groups that react easily with resin, enhancing the interfacial connections between the resin and these materials and raising the silicone adhesives' temperature resistance as a result. By functionalizing the surface of the materials with a thiol silane coupling agent (3-mercaptopropyltrimethoxysilane), it is possible to develop modified materials with active thiol groups (–SH), which increase their adhesion. Additionally, one of the conditions that permits the use of MPTMS functionalized materials as fillers for silicone adhesives is the presence of active centers (–SH). 3-Mercaptopropyltrimethoxysilane (MPTMS) may attach to the surface of modified palygorskite, thus obtaining a chemically active material. As a result, silica materials are now being used more often as fillers in silicone pressure-sensitive adhesives. Modified palygorskite fillers increase the adhesive's maximum operating temperature, making them suitable for specialized applications at high temperatures [22–34].

In this work, we have used AGLEV®SI 200 as the support for the 3-aminopropyltriethoxysilane (APTES). The resultant modified AG showed interesting properties, suggesting that this AG–APTES system could be used as an ingredient in heat-resistant silicone pressure-sensitive adhesives.

2 Experimental Section

2.1 Materials

Silicone resin—Dowsil 2013 adhesives, was supplied by Dow Corning (USA), the AGLEV®SI 200 was supplied by the TERRA ENEO (Luszowice, Poland).

2.2 Chemicals

Chemat (Gdańsk, Poland) supplied the 3-aminopropyltriethoxysilane (98%) and 3-mercaptopropyl-trimethoxysilane (95%) for this experiment. Carl Roth (Germany)

provided the toluene, while Chempur (Piekary Śląskie, Poland) provided the methanol. Organo-platinum complexes containing platinum were used as catalysts; one example of this kind was the Dow Corning (USA) SYL-OFF 4000 Catalyst. Analytical grade reagents were used throughout.

2.3 Methods of AG Modification

First, 200 cm^3 of methanol–water solvent solutions (80:20 v/v) containing a modification compound (3-aminopropyltriethoxysilane) in the range of 0.5 to 1.5 wt% in proportion to the quantity of AG were added to up to 20 g of AGLEV®SI 200. Modification of AG was carried out using an ultrasonic method (using an ultrasonic bath with a 40 kHz frequency) for 2 h at 80 °C. The reaction mixtures were then subjected to drying for 24 h at 80 °C (in an oven), filtering on a pressure funnel through a Whatman paper filter (codified EEA03), and calcination for 3 h at 480 °C (in a muffle furnace). After being ground the modified AGLEV®SI 200 was sieved through a mesh.

After modification of AG, the samples: AG and AG-APTES were characterized by FTIR/ATR, the thermal stability TGA, the elemental analysis CHNS and the mastersizer analysis.

2.4 Preparation of Si-PSA Modification Tape

The commercial folvent-free resin (DOWSIL 2013) was added to the platinium catalyst Syl-OFF 4000 in the quantity of 1.5 parts, and the mixture was then blended well to get the desired modification adhesies composition. Then, depending on the weight of the resin filler, 0.1, 0.5, 1 or 3 wt.% were added and blended until a homogenous composition was achieved. Utilizing a Byk slit applicator (ALTANA AG, Germany), the resultant compositions were coated onto a polyester film that was 50 m thick to create an XY thick sticky film. According to the catalyst safety data sheet, the composition coated in this manner was put into a Binder dryer (Binder GmbH, Germany) at 150 °C for 15 min to crosslink. A second layer of polyester film was used to fix the adhesive film that had thus been created.

2.5 Characterizations

2.5.1 Fourier Transform Infrared (FTIR/ATR)

ATR diamond plate-equipped THERMO NICOLED 380 apparatus (Waltham, MA, USA) was used to record FTIR spectra. A total of 32 scans with a resolution of 4 cm^{-1} were obtained in the 4000–400 cm^{-1} range.

2.5.2 Thermogravimetric Analysis (TGA)

TGA was carried out using thermomicrobalance TG from NETZSCH (Selb, Germany) with scan range from 25 to 800 °C at a constant heating rate of 10 °C/min, in an air atmosphere with nitrogen flow as the purge gas. Samples of 9–10 mg, loaded in Al_2O_3 crucible.

2.5.3 The Elemental Analysis CHNS

Thermo Scientific's FLASH 2000 CHNS/O Analyzer (Waltham, MA, USA) was used to conduct the elemental analysis CHNS of AG and AG-APTES. L-cysteine, L-methionine, 2,5-(Bis(5-tert-butyl-2-benzo-oxazol-2-yl) thiophene, and sulphanilamide were used as standards to calibrate the apparatus in CHNS mode. Samples were weighed to an accuracy of 0.000001 g in tin crucibles.

2.5.4 The Mastersizer Analysis

A Mastersizer 2000 apparatus was used to measure the particle size distribution using the laser diffraction technique. We measured the equivalent diameters of AG particles (D0.1, D0.5, and D0.9), the surface weighted mean (D3.2), and the volume weighted mean (D4.3) to determine the characteristic diameters for the particle size distribution. In order to characterize the spreading of the distribution, the Span value, which is defined in Eq. (1), was obtained [35]:

$$Span = (D0.9 - D0.1)/D0.5 \tag{1}$$

2.5.5 Pot-Life

The pot life of an adhesive compound after being modified for usage (for coating) is indicated by a value called pot-life. He defines it as the amount of time required to raise the original mixture's viscosity by twofold (for greater viscosities) or fourfold

(for lower viscosities). The test is conducted at room temperature (23 °C), and the measurement is started right away after the mixture has been mixed [36].

2.5.6 Adhesion

The peel adhesion of pressure-sensitive silicone adhesives was tested using a Zwick-Roell Z1 machine in accordance with the procedures of the international standard Association des Fabricants Europeens de Rubans Auto-Adhesifs (AFERA) 4001. A 2.5 cm wide adhesive tape was sticked to a steel plate under pressure 2 kg of hard rubber roller. The plate was placed in the jaws of a testing machine and the free end into the other jaw. The test measures the force with which the tape peels off the plate at a constant speed of 300 mm/min. The result is the average of the three measurements [36, 37].

2.5.7 Cohesion

Three methods were used to explore the qualities of cohesion and the balance between the adhesive and the cohesive. According to the European Association des Fabricants Europeens de Rubans Auto-Adhesifs—AFERA 4012 standard, the first and second tests were conducted at ambient temperature and a higher temperature (70 °C), respectively. A metal plate and a 2.5×2.5 cm sample of the tape are adhered together in this procedure, and a 1 kg weight is then placed on top of them. The test measures the amount of time it takes for the tape sample to separate from the metal plate [38, 39].

In last way the shear adhesion failure test (SAFT) was carried out in order to determine the Si-PSA resistance to elevated temperature. For this purpose, the samples prepared as for the cohesion test were placed in the shear tester designed at ILSAM (West Pomeranian University of Technology in Szczecin). This apparatus has been developed to determine the temperature and time in which the weld will break. The test was carried out in the range of 20–250 °C with a temperature increase of 0.5 °C min^{-1} [4].

2.5.8 Tack

According to the guidelines of the International Standard Association des Fabricants Europeens de Rubans Auto-Adhesifs (AFERA) 4015, the Tack was also assessed using a Zwik-Roell Z1 testing device. With this technique, the force needed to remove a piece of tape from a metal plate is measured. During the test, the adhesive layer's contact area with the substrate was 5 cm^2 (2.5×2 cm) [5, 40].

2.5.9 Shrinkage

The cross-cut technique was used to look at the shrinkage of pressure-sensitive adhesives that had been cross-linked. The test is conducted using PVC or PET foil that has been coated with adhesive and is adhered to a metal. Then, the prepared plate is heated to 70 °C, and after a certain amount of time (ten and thirty minutes; one, three, eight, and twenty-four hours; two, three, four, five, and seven days), the change in film size (the width of the slits created by the cuts) is assessed. The arithmetic mean of eight points represents the exam outcome [4, 5].

3 Results and Discussion

3.1 Fourier Transform Infrared (FTIR/ATR)

Figure 1 shows FTIR spectra of pure AG and modified of 3-aminopropyltriethoxysilane.

The amine (–NH) groups present in the modified AG (1700–1550 cm^{-1}) presented confirmation in the form of FTIR data that the modification of the AG was effective in changing the chemistry of AGLEV®SI 200. The spectrum from surface functionalized silica with 0.5 wt.% APTES can be noted the –CH stretching vibration bands (3100–2800 cm^{-1}) due to the presence of propyl chain added with APTES. A band at 3600–3200 cm^{-1}, connected to OH stretching of water coordinated to Mg and Al, is clearly seen in the spectra of AG. Additionally, an asymmetric band with at
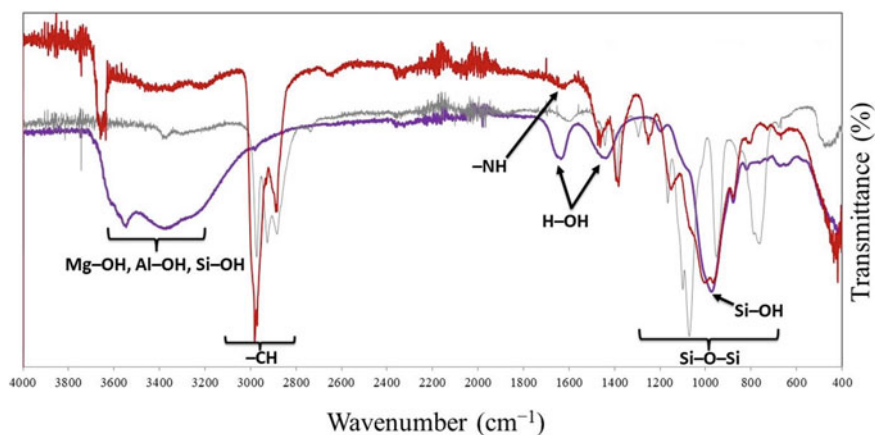
Fig. 1 Fourier transform infrared (FTIR) spectra of pure AG, AG modified APTES (AG-0.5APTES), and 3-aminopropyltriethoxysilane (as a reference sample) are shown in purple, red, and grey, respectively

Table 1 Nitrogen, carbon, hydrogen, and sulfur levels in the studied materials as well as the reaction effectiveness of the AG and AG-APTES

	N (%)	C (%)	H (%)	S (%)	Reaction efficiency (%)
AG	0.00 ± 0.00	1.08 ± 0.02	1.45 ± 0.01	0.00 ± 0.00	–
AG-0.5APTES	0.43 ± 0.01	1.10 ± 0.02	0.68 ± 0.01	0.00 ± 0.00	86.00 ± 0.00
AG-1.0APTES	0.41 ± 0.02	1.20 ± 0.04	0.69 ± 0.01	0.00 ± 0.00	41.00 ± 1.20
AG-1.5APTES	0.41 ± 0.01	1.30 ± 0.04	0.73 ± 0.07	0.00 ± 0.00	27.00 ± 0.24

1630 and 1430 cm^{-1} that corresponds to the water molecules' bending vibration is shown to exist. The spectrum also reveals the peaks due to Si–OH bonds (3600–3200 and 970 cm^{-1}). The existence of an aminopropyl functional group is shown by the new bands, which exhibit the symmetric and asymmetric stretching vibrations of the free amine –NH. A reaction between APTES and surface –OH groups, which are produced from AG and correspond to the hydroxyl bending of structural OH$_2$ and zeolitic H$_2$O, occurs. At the same time, the peak of modified AG disappeared at 1430 cm^{-1}, which indicated that the –OH group of modified AGLEV®SI 200 was significantly reduced, which further confirmed the successful reaction of 3-aminopropyltriethoxysilane with AG.

The Si–O-Si bands (1300–650 cm^{-1}) are also seen in Fig. 1's spectra, which supports the idea that 3-aminopropyltriethoxysilane-containing AG underwent silanization. In addition, peaks at 1000–1100 cm^{-1} indicated the existence of Si–O–Si groups. The high peak at 2960 cm^{-1} and weak peak at 2900 cm^{-1} were caused by the symmetric and asymmetric –CH hydrocarbon component of the spectra. The peak at 1170 cm^{-1} belonged to the –Si–OEt of APTES. The spectrums from surface functionalized silica with 1.0 and 1.5 wt.% 3-aminopropyltriethoxysilane were similar. No significant effect was observed between increasing APTES concentration and N, C or H content (Table 1). The 0.5 APTES modification proved to be the most effective—Fig. 1. [4, 28, 36, 37, 39–43].

3.2 Thermogravimetric Analysis (TGA)

Figure 2 displays the thermograms of both pure AG and AG treated with 3-aminopropyltriethoxysilane (APTES).

The thermal stability of the samples ATT-0.5–1.5APTES (modified with 0.5–1.5 wt.% APTES) was investigated in order to determine their thermal characteristics. The pure AG had a larger weight loss than all other modified samples and revealed four phases of breakdown. The temperature range for thermal breakdown is 75–125 °C for type I, 200–250 °C for type II, 300–400 °C for type III, and 550–700 °C for type IV. The first mass loss happens relatively quickly and is caused by the elimination of bound water, as may be illustrated. Due to the event's immaculate
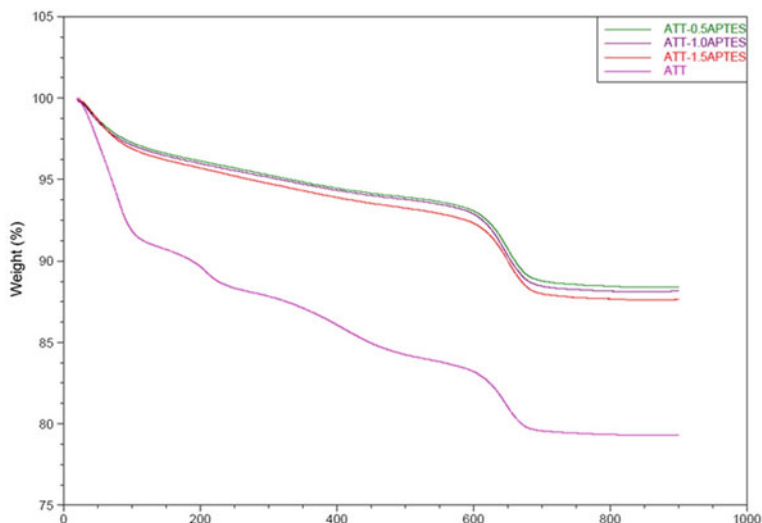
Fig. 2 TGA curves of AG and AG modified with 0.5–1.5 wt.% APTES

reversibility and the clay's exceptional water-absorbing qualities, the second water loss is equivalent to the water's whole eradication. The third weight loss is related to the development of a rafter structure and the slow evaporation of crystallized water (coordinated to cations along octahedral sheets). It should be noted that an AG may still absorb water by capillarity in this situation. The fourth water mass loss in AG is caused by the dehydroxylation of Mg–OH groups. It is also required to include the release of carbon hydroxide in the fourth mass loss since the carbonates in the AG are thermally unstable at 500 °C and their breakdown releases CO_2—Fig. 2 [3, 4, 26, 35, 44–46].

The 5% weight loss for AGLEV®SI 200 after modification of 3-aminopropyltriethoxysilane at higher temperatures. Thermal stability of the AG modified with APTES measured by TGA was improved relative to the pure AG—Fig. 2 [4, 19].

3.3 The Elemental Analysis CHNS

Elemental analysis proved the modified AG included amino groups (Table 1).

According to the elemental analyser data in Table 1, the pure AG has no nitrogen or sulfur (N 0.00%, S 0.00%). The surface functionalized silica with 0.5–1.5 wt% 3-aminopropyltriethoxysilane contained nitrogen. The obtained findings support the amine (–NH) group presence in the modified AG (AG-0.5APTES, AG-1.0APTES, and AG-1.5APTES) molecules. The elemental analysis revealed that the samples

AG-0.5APTES, AG-1.0APTES, and AG-1.5APTES had nitrogen contents of 0.43, 0.41, and 0.41%, respectively—Table 1.

3.4 Mastersizer Analysis

Table 2 shows the characteristic diameters of AG particle size before and after modification such as the equivalent diameters of AG particles D0.1, D0.5, D0.9, surface weighted mean D3.2, as well as the volume weighted mean D4.3.

A Mastersizer 2000 equipment was used to measure the particle size distribution. The size distributions demonstrate that additives may achieve a range of finer particles even when used in relatively small amounts (0.5–1.5 wt%). Comparing higher span values obtained with coupling agents to lower span values obtained without this compound, which showed a tighter distribution, span values in Table 2 show that the size distribution is widening in the presence of coupling agents. As stated in Eq. (1)—Table 2, several diameter characteristics for the particle size distribution were obtained, including the D0.1, D0.5, and D0.9, as well as the mean volume diameter D4.3, the mean surface weighted D3.2, and the Span value. Numerous applications, including as adsorption, catalysis, electrochemistry, chromatography, and nanocomposite materials, depend on the amine moiety. Functionalization of attapulgite surfaces with amine groups (with an aminoterminated organosilicon 3-aminopropyltriethoxysilane), makes it possible to obtain modified materials that are effective adsorbents for aqueous reactive dye removal by modifying. When 3-aminopropyltriethoxysilane (APTES) is newly deposited, a combination of neutral and protonated amine groups coexist on the materials. In contrast to free amines and carbon, which are further from the silicon dioxide surface, protonated and hydrogen-bonded APTES amines are present near to the surface and interact with it through electrostatic and hydrogen bonds. Longer reaction times result in multilayers followed by the formation of macroscopic aggregates of APTES. Easy to produce, stable monolayers, and a homogenous immobilization surface are just a few of the benefits that 3-aminopropyltriethoxysilane provides in applications. Various surface coatings, such as Au NPs, polymers (poly(vinyl alcohol), PEG, polyacrylamide, etc.), and biopolymers (dextran, CS, and protein aggregates), may be modified with the use of this substance to assist decrease nonspecific adsorption. APTES can also be

Table 2 Means characteristic diameters of the AG and AG-APTES

	D0.1 (μm)	D0.5 (μm)	D0.9 (μm)	Span	D3.2 (μm)	D4.3 (μm)
AG	40.04 ± 5.00	425.89 ± 5.50	603.20 ± 2.13	1.32	68.38 ± 2.13	367.44 ± 3.04
AG-0.5APTES	22.60 ± 2.04	134.56 ± 4.00	261.91 ± 1.28	1.78	37.32 ± 3.57	140.58 ± 3.00
AG-1.0APTES	14.22 ± 0.26	102.88 ± 2.01	231.09 ± 4.00	2.11	24.04 ± 4.01	110.11 ± 5.02
AG-1.5APTES	9.16 ± 4.02	81.20 ± 3.00	195.72 ± 1.04	2.30	18.44 ± 2.04	92.32 ± 5.00

subjected to prior modification in order to apply this coupling agent in analytical, bioanalytical, and clinical chemistry [2, 15, 17, 19, 21, 28, 30, 32, 34, 36].

Figures 3, 4, 5, 6 illustrated the effect of filler and modified filler on the time-varying viscosity of the Si-PSA mixture. Non-modified AG demonstrate increased viscosity for a brief period (1 wt.%), followed by a reduction for 0.5 wt.%, below the formulation value for non-filler, and then a further rise. This could be as a result of the filler's excellent dispersion in the resin at 0.5 wt.% filling levels and agglomeration at higher filling levels (both for 1 and 3 wt.% the viscosity values were fairly comparable). Changes in the brightness were seen for both AG adjustments. With each adjustment, the adhesive composition's filler content increased and greater viscosity values were obtained. On the other hand, the curves of the composition's consecutive filling are closer together and their values do not deviate as much from one another the larger the quantity of the filler-modifying component.

Figure 7 shows data on how adding modified AG via APTES affected silicone pressure-sensitive adhesive adherence. According to previous instances of modification with fillers, such as montmorillonite, mentioned in the literature, increasing the filler addition always caused a drop in the adhesion value [3–5]. Compositions modified with APTES modified fillers achieved higher or equal adhesion values compared to the modification with unmodified AG. AG modified 1.0% wt. APTES achieved the highest increase in value for the various fillings by approx. 10–15%. This proves the better compatibility of the filler modification with the Si-PSA polymer matrix and most likely to a lower tendency towards agglomeration.
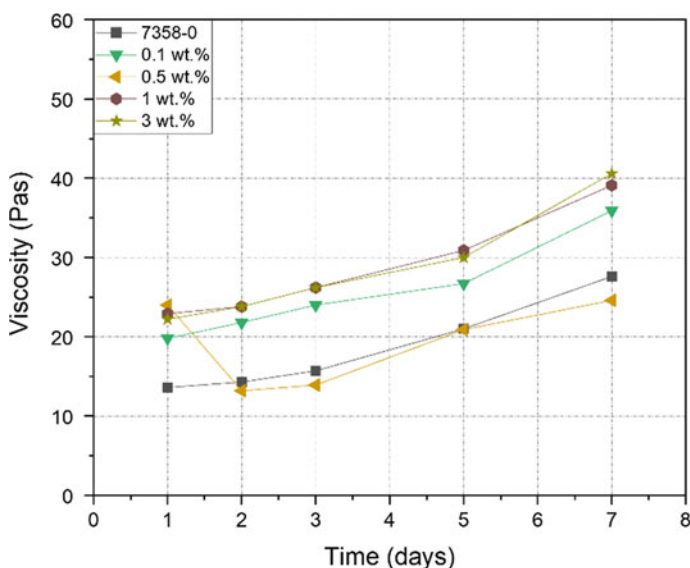
Fig. 3 Influence on AG addition on Si-PSA composition viscosity
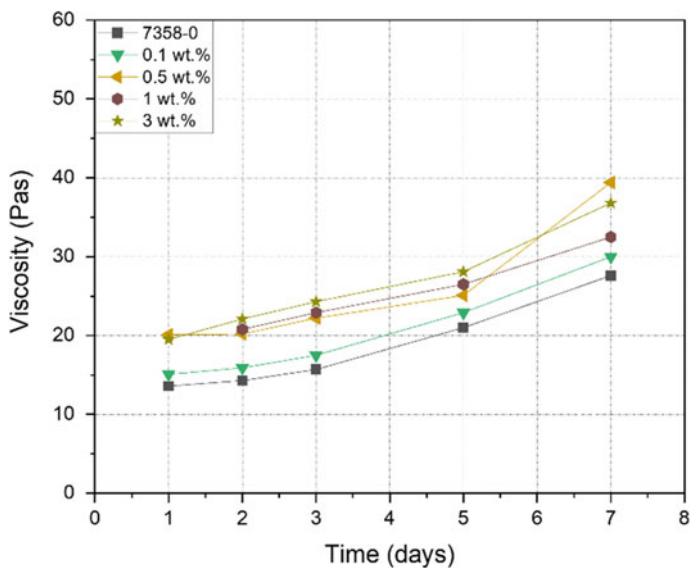
Fig. 4 Influence on AG-0,5APTES addition on Si-PSA composition viscosity
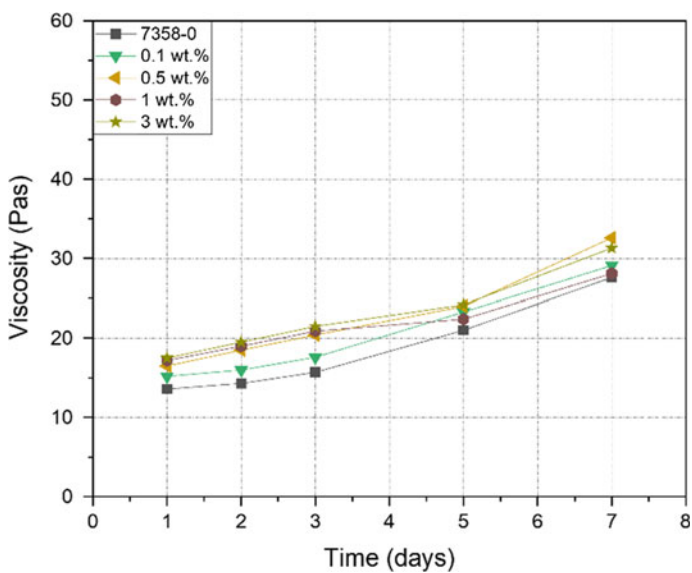
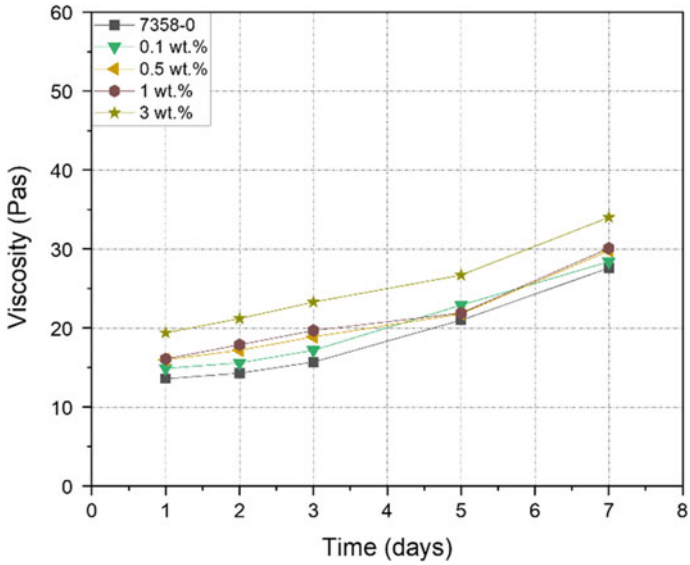**Fig. 5** Influence on AG-1,0APTIES addition on Si-PSA composition viscosity

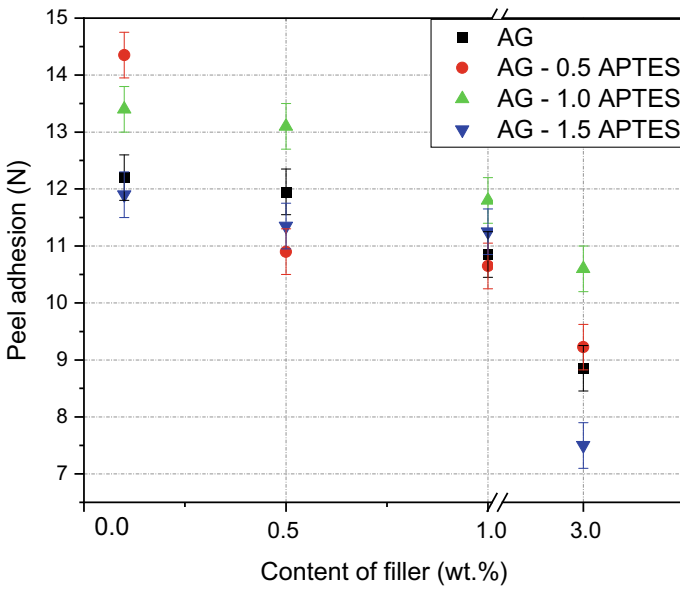**Fig. 6** Influence on AG-1,5APTIES addition on Si-PSA composition viscosity

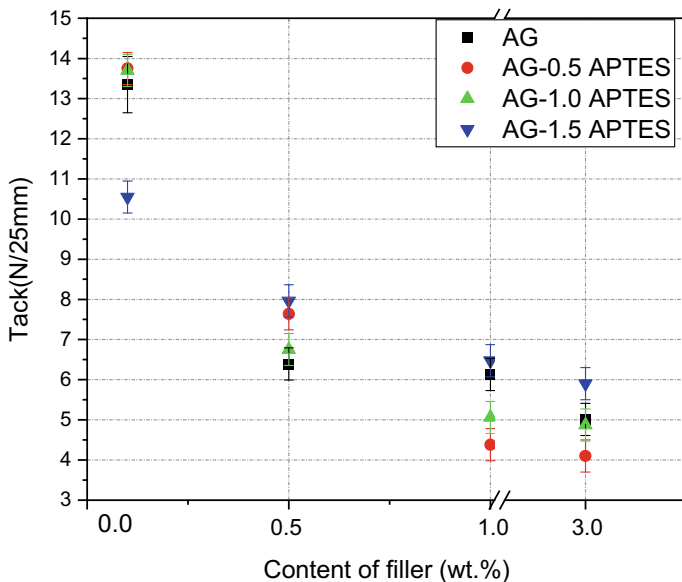**Fig. 7** Influence on AG modified by APTES addition on Si-PSA tape adhesion

Fig. 8 Influence on AG modified by APTES addition on Si-PSA tape tack

The tack values were reduced by both the original AG and its changes, with the filler content having the greatest impact (see Fig. 8). The degree of filler alteration had no impact on how these values changed [40, 49]. The samples with the lowest filler levels (0.1 wt.%) treated with 1.5 APTES revealed a gradual decline in tack value. The absence of the same effect as for adhesion may be due to the filler's impact on the balance of the adhesive and cohesive properties and its improved stability.

Figure 9 shows the results of the cohesion at the temperature of 20 °C depending on the amount of the filler. In the case of AG modified APTES a drop below 72 h was recorded only for the highest degree of filler filling.

Only modest fills (0.1 wt.%) were tested for cohesion at a high temperature (70 °C), but the samples exhibited satisfactory cohesion for both AG modifications. This is because the filler and resin work well together and because the adhesive-cohesive balance has been stabilized. The samples did not hold up for 72 h in the case of greater adhesive-cohesive fillings because there was likely a change in the balance in favor of cohesion (Fig. 10). This effect is also confirmed by the adhesion and tack results presented in the figures above.

The results are directly translated into the Maximum work temperature measured in the SHAFT test (Fig. 11); where the maximum measurement temperature was reached for the lower filling, it was lower in other cases. This, along with the findings from other tests, indicates that such a large addition has an adverse impact on the characteristics of self-adhesive tapes. The literature supports the fact that just a little quantity of filler is required to produce excellent heat resistance and keep the adhesive
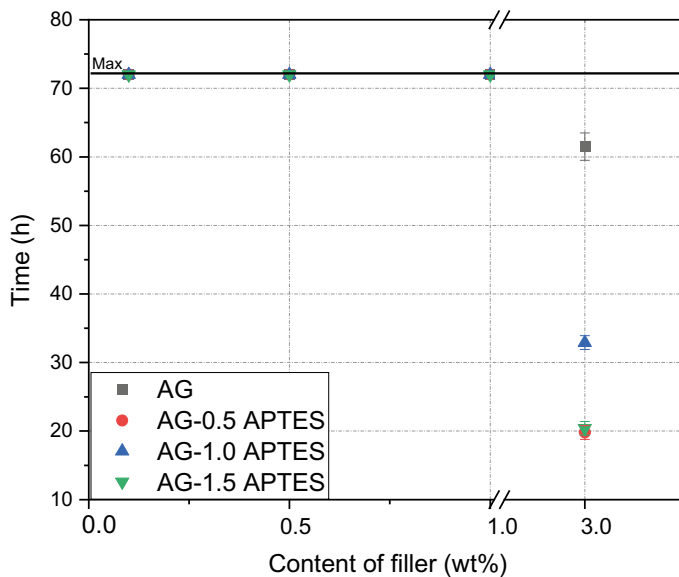
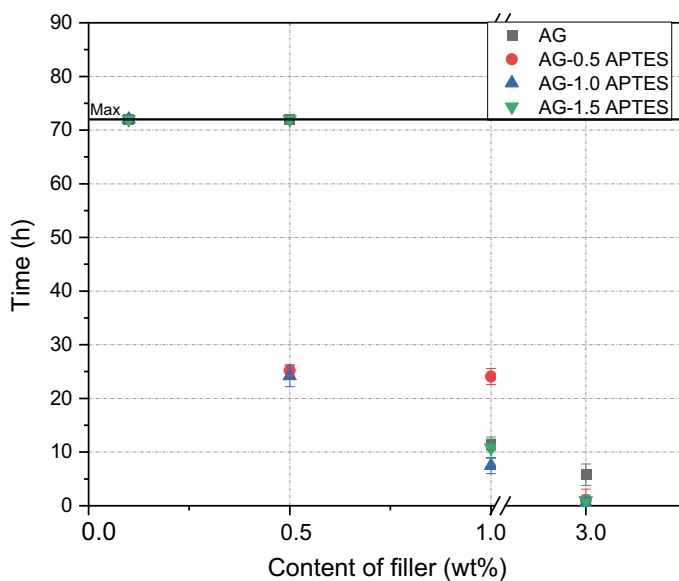**Fig. 9** Influence on AG modified by APTES addition on Si-PSA tape cohesion in 20 °C

Fig. 10 Influence on AG modified by APTES addition on Si-PSA tape cohesion in 70 °C
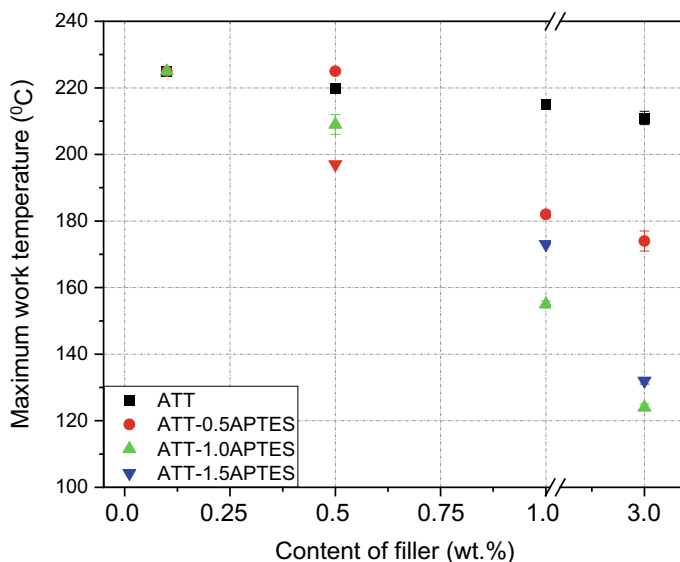
Fig. 11 Influence on AG modified by APTES addition on Si-PSA tape SAFT

tape's utility [36, 41]. The presented results greatly limit the amount of filler used, which would not significantly affect the properties.

Shrinkage increase with adhesive films, both with and without fillers, was seen in Figs. 11, 12, 13, 14, 15. The reference in each instance of filling was the adhesive film without filler, which had a skin resistance greater than the permitted 0.5%. The greatest results were shown by cassettes with a 0.1 wt.% filler content. They succeeded in stabilizing the skin between 0.1 and 0.3% filler. Although there was no persistent shrinkage over the 0.5% limit, higher fills did not maintain the crusts low, which may have been due to partial agglomeration of the filler in the adhesive formulation. Although it is a predictable consequence, the stabilizing effect of the cross-linked adhesive film achieved by adding fillers to the adhesive composition is often connected to larger fill concentrations [39]. In the case of the tested use, the bulk density and lightness could have had an influence (for the lowest values tested). As a result, a more compact adhesive film was obtained than in the case of higher fillings, where an agglomeration effect could occur.

4 Conclusions

Experiments on the modification of the starting AGLEV®SI 200 were carried out by ultrasound and by using coupling agent 3-aminopropyltriethoxysilane (APTES) and in amounts ranging from 0.5 to 1.5 wt.% relative to the amount of AG, to improve the chemical compatibility of this mineral with specific resins for application in
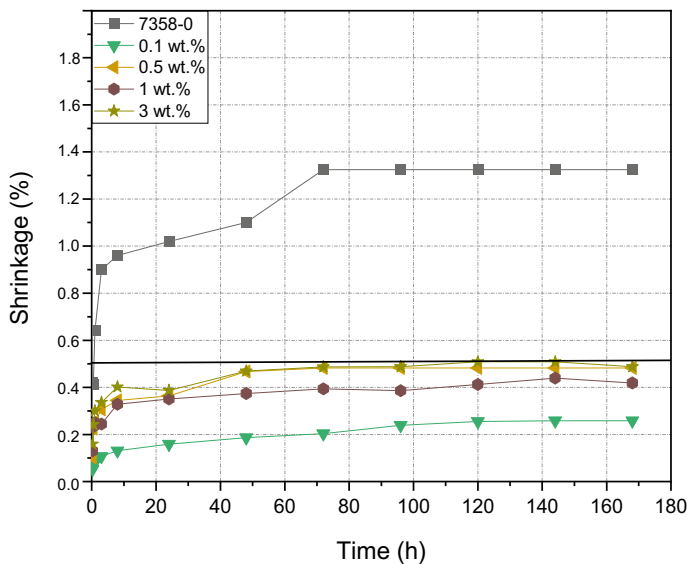
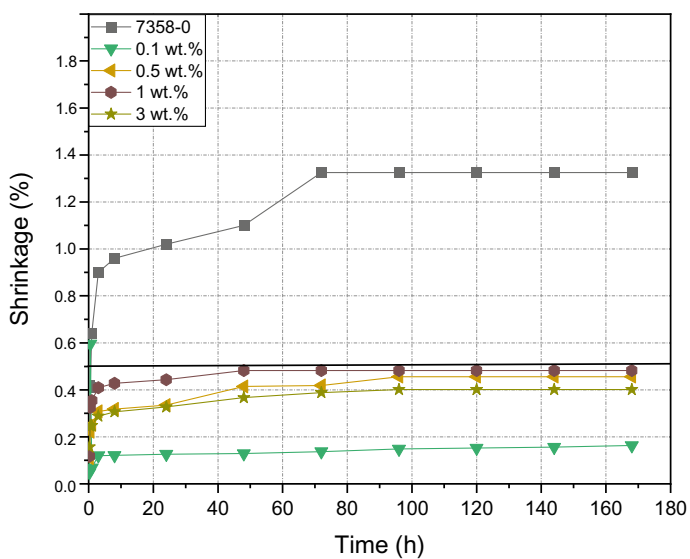**Fig. 12** Influence on AG addition on shrinkage Si-PSA

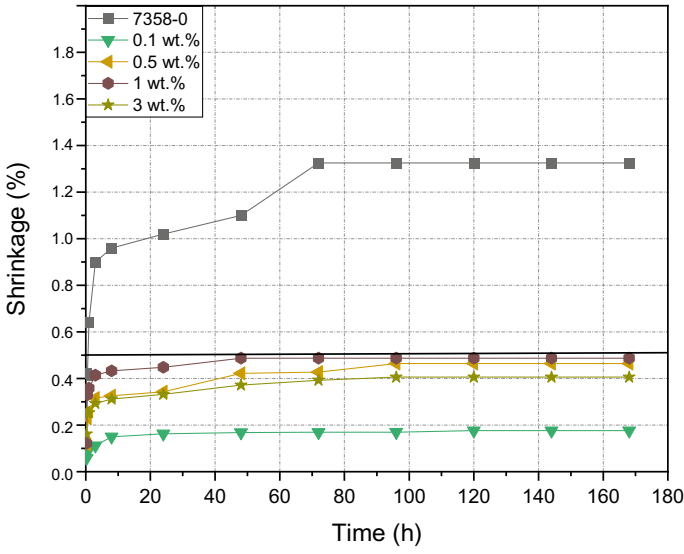**Fig. 13** Influence on AG-0.5APTES addition on shrinkage Si-PSA

Fig. 14 Influence on AG-1.0APTES addition on shrinkage Si-PSA
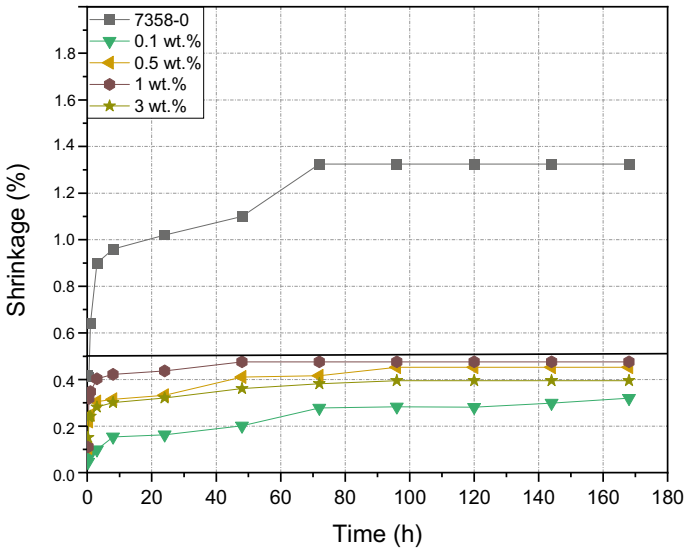

Fig. 15 Influence on AG-1.5APTES addition on shrinkage Si-PSA

heat-resistant silicone pressure-sensitive adhesives. The effectiveness of the stated modification method of AG utilizing APTES was validated by study findings from infrared spectroscopy and CHNS elemental analysis. As revealed by the existence of -NH and Si–O–Si groups in the modified AG and the increase in thermal stability compared to the pure AG, the testing findings showed that the APTES modified AG was effective in changing the chemistry of AGLEV®SI 200. This research shows the possibility of AG, a plentiful and readily-accessible fibrous clay mineral, to be used as fillers in self-adhesive tapes.

AG and its modified versions was used to modifying the selected silicone pressure-sensitive adhesives composition to obtained new self-adhesive tapes, which exhibit increased thermal resistance. At the same time, new tape is keeping the fundamental functional characteristics above those permitted for self-adhesive tapes, such as adhesion of 10 N25 mm^{-1}, 8 N tack, cohesiveness of more than 72 h, and shrinking of less than 0.5%. The greatest results were obtained with tapes containing 0.1 wt.% filler, which also exhibited steady shrinkage at a level of 0.4% and cohesiveness at room and increased temperature levels of >72 h. The value adhesion and tack at levels of around 11–15 N25 mm^{-1} and 10–14 N were the significant differences amongst the tapes obtained. This demonstrates that a variety of self-adhesive tapes may be created using the materials available.

The developed tapes, which have a higher thermal resistance, can be applied as insulating materials in heating and construction projects (when installing fireplaces); masking in powder coating (baking in furnaces); glass varnishing; thermoprinting; or electrical engineering in the insulation of motor windings.

References

1. Samal, S.: Effect of shape and size of filler particle on the aggregation and sedimentation behavior of the polymer composite. Powder Technol. **366**, 43–51 (2020). https://doi.org/10.1016/j.powtec.2020.02.054

2. Antosik, A.K., Mozelewska, K., Piątek-Hnat, M., Czech, Z., Bartkowiak, M.: Silicone pressure-sensitive adhesives with increased thermal resistance. J. Therm. Anal. Calorim. (2021). https://doi.org/10.1007/s10973-021-11048-y

3. Tolia, G., Li, S.K.: Silicone adhesive matrix of verapamil hydrochloride to provide PH-independent sustained release. AAPS Pharm. Sci. Tech. **15**, 1–10 (2014). https://doi.org/10.1208/s12249-013-0004-8

4. Antosik, A.K., Makuch, E., Gziut, K.: Influence of modified attapulgite on silicone pressure-sensitive adhesives properties. J. Polym. Res. **29** (2022). https://doi.org/10.1007/s10965-022-02981-z

5. Antosik, A.K., Mozelewska, K., Czech, Z., Piątek-Hnat, M.: Influence of montmorillonite on the properties of silicone pressure-sensitive adhesives: preparation of a double-sided tape based on the best composition. SILICON **12**, 1887–1893 (2020). https://doi.org/10.1007/s12633-019-00295-2

6. Antosik, A.K., Bednarczyk, P., Czech, Z.: Aging of silicone pressure-sensitive adhesives. Polym. Bull. **75**, 1141–1147 (2018). https://doi.org/10.1007/s00289-017-2083-2

7. Du, M., Guo, B., Jia, D.: Newly emerging applications of halloysite nanotubes: a review: applications of halloysite nanotubes. Polym. Int. **59**, 574–582 (2010). https://doi.org/10.1002/pi.2754

8. Chen, D., Du, Y., Zhu, H., Deng, Y.: Applied clay science synthesis and characterization of a micro Fi Brous TiO_2-CdS/palygorskite nanostructured material with enhanced visible-light photocatalytic activity. Appl. Clay Sci. **87**, 285–291 (2014). https://doi.org/10.1016/j.clay.2013.11.031

9. An, L., Pan, Y., Shen, X., Lu, H., Yang, Y.: Rod-like attapulgite/polyimide nanocomposites with simultaneously improved strength, toughness. Therm. Stab. Related Mech. 4928–4941 (2008). https://doi.org/10.1039/b805849k

10. Du, M., Jia, D.: Newly emerging applications of halloysite nanotubes: a review. 574–582 (2010). https://doi.org/10.1002/pi.2754

11. Peng, J., Sun, H., Wang, J., Qiu, F., Zhang, P., Ning, W., Zhang, D., Li, W., Wei, C., Miao, S.: Highly stable and recyclable sequestration of CO_2 using supported melamine on layered-chain clay mineral (2021)

12. Zhang, L., Lv, F., Zhang, W., Li, R., Zhong, H., Zhao, Y.: Photo degradation of methyl orange by attapulgite—SnO_2–TiO_2 nanocomposites. **171**, 294–300 (2009). https://doi.org/10.1016/j.jhazmat.2009.05.140

13. Zhang, L., Zhang, J., Zhang, W., Liu, J., Zhong, H., Zhao, Y.: Photocatalytic activity of attapulgite—BiOCl—TiO_2 toward degradation of methyl orange under UV and visible light irradiation. Mater. Res. Bull. **66**, 109–114 (2015). https://doi.org/10.1016/j.materresbull.2015.02.029

14. Cao, J., Shao, G., Wang, Y., Liu, Y., Yuan, Z.: CuO catalysts supported on attapulgite clay for low-temperature CO oxidation. **9**, 2555–2559 (2008). https://doi.org/10.1016/j.catcom.2008.07.016

15. Chen, L., Zhai, Y., Ding, H., Zhou, G., Zhu, Y., Hui, D.: Preparation, characterization and thermoelectricity of ATT/TiO_2/PANI nano-composites doped with different acids. Compos. B Eng. **45**, 111–116 (2013). https://doi.org/10.1016/j.compositesb.2012.02.028

16. Liu, J., Zhong, J., Chen, Z., Mao, J., Liu, J., Zhang, Z., Li, X., Ren, S.: Preparation, characterization, application and structure evolution of attapulgite: from nanorods to nanosheets. Appl. Surf. Sci. **565** (2021). https://doi.org/10.1016/j.apsusc.2021.150398

17. Park, S.: Types and health hazards of fibrous materials used as asbestos substitutes. **9**, 360–364 (2018). https://doi.org/10.1016/j.shaw.2018.05.001

18. García-Sánchez, A., Miranda-Díaz, A.G., Cardona-Muñoz, E.G.: The role of oxidative stress in physiopathology and pharmacological treatment with pro- and antioxidant properties in chronic diseases. Oxidative Med. Cell. Longevity **2020** (2020). https://doi.org/10.1155/2020/2082145

19. Bertuoli, P.T., Piazza, D., Scienza, L.C., Zattera, A.J.: Applied clay science preparation and characterization of montmorillonite Modi Fi Ed with 3-aminopropyltriethoxysilane. **87**, 46–51 (2014). https://doi.org/10.1016/j.clay.2013.11.020

20. Shuali, U., Nir, S., Rytwo, G.: Adsorption of Surfactants, Dyes and Cationic Herbicides on Sepiolite and Palygorskite: Modifications, Applications and Modelling, 1st edn, Vol. 3. Elsevier B.V. (2011). ISBN 9780444536075

21. Jose, A., Jose, A.: Sepiolite À palygorskite : a continuous polysomatic series. **61**, 461–472 (2013). https://doi.org/10.1346/CCMN.2013.0610505

22. Feng, J., Yi, X., Huang, W., Wang, Y., He, X.: Novel triterpenoids and glycosides from durian exert pronounced anti-inflammatory activities. Food Chem. **241**, 215–221 (2018). https://doi.org/10.1016/j.foodchem.2017.08.097

23. da Silva, T.F., de Souza, G.P.M., de Melo Morgado, G.F., Albers, A.P.F., Quinteiro, E., Passador, F.R.: Influence of surface modification of attapulgite (ATP) with aminosilane (3-aminopropyl) triethoxysilane for the preparation of LLDPE/ATP nanocomposites. J. Polym. Res. **29**, 95 (2022). https://doi.org/10.1007/s10965-022-02953-3

24. Wang, H., Gurau, G., Shamshina, J., Cojocaru, O.A., Janikowski, J., Macfarlane, D.R., Davis, J.H., Rogers, R.D.: Chemical science simultaneous membrane transport of two active hydrogen bond complex formation. 3449–3456 (2014). https://doi.org/10.1039/c4sc01036a

25. Wang, L., Sheng, J.: Preparation and properties of polypropylene/org-attapulgite nanocomposites. Polymer **46**, 6243–6249 (2005). https://doi.org/10.1016/j.polymer.2005.05.067

26. Peng, L., Zhou, L., Li, Y., Pan, F., Zhang, S.: Synthesis and properties of waterborne polyurethane/attapulgite nanocomposites. **71**, 1280–1285 (2011). https://doi.org/10.1016/j.compscitech.2011.04.012

27. Fan, Z., Zhou, S., Mao, H., Li, M., Xue, A., Zhao, Y., Xing, W.: A novel ceramic microfiltration membrane fabricated by anthurium andraeanum-like attapulgite nanofibers for high-efficiency oil-in-water emulsions separation. J. Membr. Sci. **630** (2021). https://doi.org/10.1016/j.memsci.2021.119291

28. Structures, Z.: Synthesis and photocatalytic activity of hierarchical Zn-ZSM-5 structures (2021)

29. Li, J., Lei, Y., Xu, D., Liu, F., Li, J., Sun, A.: Improved mechanical and thermal insulation properties of monolithic attapulgite nano Fi ber/silica aerogel composites dried at ambient pressure. J. Sol-Gel Sci. Technol. 702–711 (2017). https://doi.org/10.1007/s10971-017-4359-2

30. Wang, W., Wang, A.: Applied clay science recent progress in dispersion of palygorskite crystal bundles for nanocomposites. Appl. Clay Sci. **119**, 18–30 (2016). https://doi.org/10.1016/j.clay.2015.06.030

31. Aly, A.A., Zeidan, E.B., Alshennawy, A.A., El-masry, A.A., Wasel, W.A.: Friction and wear of polymer composites filled by nano-particles: a review. **2012**, 32–39 (2012)

32. Bao, Y., Li, X., Tang, P., Liu, C., Zhang, W., Ma, J.: Attapulgite modified cotton fabric and its flame retardancy. Cellulose **26**, 9311–9322 (2019). https://doi.org/10.1007/s10570-019-02709-1

33. Wang, Y., Zhou, R., Wang, C., Zhou, G., Hua, C., Cao, Y.: Novel environmental-friendly nano-composite magnetic attapulgite functionalized by chitosan and EDTA for cadmium(II) removal. 817 (2020). https://doi.org/10.1016/j.jallcom.2019.153286

34. Liu, L., Ying, G., Zhao, Y., Li, Y., Wu, Y., Wen, D., Wu, M., Wang, M., Zhou, Q., Wang, X., et al.: Attapulgite–MXene hybrids with $Ti_3C_2T_x$ lamellae surface modified by attapulgite as a mechanical reinforcement for epoxy composites. Polymers **2021**, 13 (1820). https://doi.org/10.3390/polym13111820

35. Boudriche, L., Chamayou, A., Calvet, R., Hamdi, B., Balard, H.: Corrigendum to "Influence of different dry milling processes on the properties of an attapulgite clay, contribution of inverse gas chromatography". Powder Technol. **254**, 352–363 (2014)]. Powder Technol. **257**, 191 (2014). https://doi.org/10.1016/j.powtec.2014.02.062

36. Bartkowiak, M., Czech, Z., Mozelewska, K., Kabatc, J.: Comparison between thermal crosslinkers based on melamine-formaldehyde and benzoguanamine resin and their influence on main performance of acrylic pressure-sensitive adhesives as tack, peel adhesion, shear strength and pot-life. Polym. Testing **89**, 106596 (2020). https://doi.org/10.1016/j.polymertesting.2020.106596

37. Sowa, D., Czech, Z., Byczyński, Ł: Peel adhesion of acrylic pressure-sensitive adhesives on selected substrates versus their surface energies. Int. J. Adhes. Adhes. **49**, 38–43 (2014). https://doi.org/10.1016/j.ijadhadh.2013.12.013

38. Sasaki, M., Fujita, K., Adachi, M., Fujii, S., Nakamura, Y., Urahama, Y.: The effect of tackifier on phase structure and peel adhesion of a triblock copolymer pressure-sensitive adhesive. Int. J. Adhes. Adhes. **28**, 372–381 (2008). https://doi.org/10.1016/j.ijadhadh.2007.11.002

39. Sun, S., Li, M., Liu, A.: A review on mechanical properties of pressure sensitive adhesives. Int. J. Adhes. Adhes. **41**, 98–106 (2013). https://doi.org/10.1016/j.ijadhadh.2012.10.011

40. Tordjeman, P., Papon, E., Villenave, J.: Tack properties of pressure-sensitive adhesives. J. Polym. Sci. B Polym. Phys. **38**, 1201–1208 (2000). https://doi.org/10.1002/(SICI)1099-0488(20000501)38:9<1201::AID-POLB12>3.0.CO;2-%23

41. Tiu, B.D.B., Delparastan, P., Ney, M.R., Gerst, M., Messersmith, P.B.: Enhanced adhesion and cohesion of bioinspired dry/wet pressure-sensitive adhesives. ACS Appl. Mater. Interfaces **11**, 28296–28306 (2019). https://doi.org/10.1021/acsami.9b08429

42. Falayi, T., Ntuli, F.: Effect of attapulgite calcination on heavy metal adsorption from acid mine drainage. Korean J. Chem. Eng. **32**, 707–716 (2015). https://doi.org/10.1007/s11814-014-0266-1

43. Falayi, T., Ntuli, F.: Removal of heavy metals and neutralisation of acid mine drainage with un-activated attapulgite. J. Ind. Eng. Chem. **20**, 1285–1292 (2014). https://doi.org/10.1016/j.jiec.2013.07.007

44. Ni, Z., Xia, S., Wang, L., Xing, F., Pan, G.: Treatment of methyl orange by calcined layered double hydroxides in aqueous solution: adsorption property and kinetic studies. **316**, 284–291 (2007). https://doi.org/10.1016/j.jcis.2007.07.045

45. Boudriche, L., Chamayou, A., Calvet, R., Hamdi, B., Balard, H.: Influence of different dry milling processes on the properties of an attapulgite clay, contribution of inverse gas chromatography. Powder Technol. **254**, 352–363 (2014). https://doi.org/10.1016/j.powtec.2014.01.041

46. Li, M., Wu, Z., Kao, H.: Study on preparation, structure and thermal energy storage property of capric-palmitic acid/attapulgite composite phase change materials. Appl. Energy **88**, 3125–3132 (2011). https://doi.org/10.1016/j.apenergy.2011.02.030